Oscillations magnétiques et domaines de Condon dans des métaux

Roman B.G. Kramer

Thèse

présentée par

Roman Bernd Günter Kramer

pour obtenir le titre de Docteur
de l'Université Joseph Fourier - Grenoble I
en Physique

Magnetic Oscillations in Metals
Condon Domains

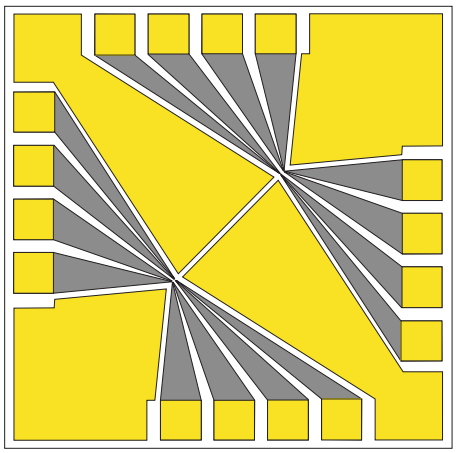

Soutenue publiquement le 2 décembre 2005 devant le jury:
L.P. Lévy, Président
R. Monnier, Rapporteur
J. Wosnitza, Rapporteur
V.S. Egorov, Examinateur
V.P. Mineev, Examinateur
A.G.M. Jansen, Directeur de thèse
W. Joss, Directeur de thèse

Thèse préparée au Grenoble High Magnetic Field Laboratory

Acknowledgements

This thesis has been prepared at the Grenoble High Magnetic Field Laboratory, formerly a cooperation of the Max-Planck-Institute for Solid State Research and the Centre National de la Recherche Scientifique. I would like to thank all people who have contributed to its success. In particular, I am grateful to:

- Louis Jansen, my Ph.D. supervisor, for his continuous interest, ideas, and motivations during this thesis. Even after having moved to the CEA he was always receptive for all kind of problems and offered readily his help.

- Valerij Egorov, one of the pioneers on the field of Condon domains, with whom I had the pleasure to work. Without him this work would certainly not have been as successful as it was. I am very grateful for his advice, help, and discussions as an great experimental physicist. Moreover, I will always remember his famous "lectures" and our trips to the mountains around Grenoble.

- Walter Joss, my Ph.D. co-supervisor, who managed to get the financial support from the Max-Planck-Institute for Solid State Research in Stuttgart for this thesis, even after Max-Planck had already left Grenoble.

- René Monnier and Jochen Wosnitza who kindly accepted to serve as "rapporteurs" for this work.

- Laurent Lévy and Vladimir Mineev for their participation in the jury of the Ph.D. defence as the president and examiner, respectively.

- Vitaly Gasparov for the preparation of single crystal samples of outstanding quality.

- Werner Dietsche for his advice in the choice of the semiconductor material for the Hall probes and for the immediate supply of these layers.

- Michel Schlenker for many useful discussion and for initiating the subject of Condon domain visualization in Grenoble. By the way, he invited Valerij Egorov for the first time to Grenoble.

- Frank Schartner and Birgit Lemke form the Technology group of the Max-Planck-Institute in Stuttgart for preparing the Hall probe structures.

I wish to thank all my other colleagues in the laboratory, Ph.D. and diploma students, scientist, technicians, secretaries for their help and for creating a nice atmosphere.
Last, but certainly not least, I would like to thank my family and my friends for their unfailing support during these years in Grenoble.

Contents

Introduction en français

Dans cette thèse, les domaines magnétiques, connus sous le nom de "domaines de Condon" ou "domaines diamagnétiques" sont étudiés. L'expression "domaines magnétiques" signifie la subdivision d'un échantillon en régions ayant une aimantation uniforme. Les domaines les plus intuitifs sont les domaines ferromagnétiques. Ces domaines ont été étudiés intensivement au siècle dernier et aujourd'hui, on répond facilement à la question "que sont des domaines magnétiques ?" en montrant des images de structure de domaines, obtenues directement par l'effet Faraday ou par la méthode de décoration. D'autres exemples de domaines magnétiques sont les domaines dans l'état intermédiaire des supraconducteurs et les structures de vortex. Pour visualiser ces structures, des nouvelles techniques d'observation (microsonde de Hall, micro-SQUID ...) ont été mises au point.

L'origine des domaines de Condon n'est pas l'interaction entre spins des électrons, comme dans le cas des domaines ferromagnétiques, mais les oscillations quantiques de l'aimantation d'un métal soumis à un champ magnétique extérieur, l'effet de Haas-van Alphen (dHvA). L'effet dHvA, prédit par Landau et, expérimentalement montré par de Haas et van Alphen dans les années 1930, est un outil très important dans la physique du solide parce que l'observation de ces oscillations permet de déterminer expérimentalement les surfaces de Fermi des métaux. Généralement, le comportement de l'aimantation est très bien décrit par la formule de Lifshitz-Kosevich (LK) [1], cependant, Shoenberg a découvert en 1962 [2] que, dans certaines conditions, si l'amplitude des oscillations est comparable à leur période, des déviations considérables existent entre la formule LK et les observations expérimentales. Shoenberg explique ces observations en remplaçant le champ H dans la formule LK par l'induction B. Ce remplacement a le caractère d'une interaction parce que l'aimantation dHvA, $M(B)$, influence le champ quantifiant $B = \mu_0\big(H + M(B)\big)$. Condon a proposé, en 1966, que la solution auto-cohérente de ce problème peut conduire à une instabilité du système vis-à-vis de la formation d'une structure de domaines d'aimantation alternée [3]. L'existence des domaines de Condon a été démontrée jusqu'à présent dans un certain nombre de métaux, à l'aide de la résonance magnétique nucléaire dans l'argent par Condon et Walstedt [4] et à l'aide de la rotation de spin de muon (μSR) sur le béryllium, l'étain, le plomb et l'aluminium par Solt *et al.* [5, 6]. Ces méthodes spectroscopiques ne permettent cependant pas de déterminer la taille, la géométrie et la topologie de ces domaines. Le sujet principal de cette thèse est

la visualisation des domaines de Condon grâce à une sonde locale de l'aimantation, une micro sonde de Hall.

Les calculs théoriques ont montré que la transition entre l'état homogène et l'état avec domaines est de premier ordre [7]. En principe, une telle transition de phase est accompagnée par l'hystérèse de l'aimantation. Le second sujet de cette thèse est l'étude de la réversibilité de l'aimantation d'un échantillon en présence de domaines de Condon. On montre l'existence de l'hystérèse dans l'effet dHvA à l'aide de plusieurs méthodes, sondes de Hall et mesure de la susceptibilité AC. La découverte de l'hystérèse permet de déterminer, avec une grande sensibilité, la ligne de coexistence de l'état homogène et de l'état avec domaines. Ce comportement est utilisé pour déterminer expérimentalement les diagrammes de phase (T, H) des domaines de Condon pour un échantillon d'argent et un échantillon de béryllium. Notons que, jusqu'à présent, seulement très peu de données existent [4, 6], capables de vérifier les calculs théoriques des diagrammes de phase [8, 9].

Au premier chapitre, la théorie des oscillations quantiques et le mécanisme de l'interaction magnétique sont brièvement introduits.

Les dispositifs expérimentaux et l'instrumentation sont présentés dans le second chapitre. Le dispositif cryogénique et les différents types de bobines de champ magnétique utilisées y sont décrits. Les caractéristiques de la méthode de mesure de la susceptibilité AC par mutuelle inductance, quelques aspects concernant l'effet de Hall et le choix du matériau utilisé dans les différentes évolutions des sondes de Hall sont discutés.

Au cours du troisième chapitre, on présente les expériences de visualisation des structures magnétiques des domaines de Condon par des réseaux de microsondes de Hall. Du comportement d'une série de sondes, on va déduire la direction de propagation des parois des domaines et de leur orientation.

Dans le quatrième chapitre, les expériences montrant l'hystérèse dans l'effet dHvA en présence de domaines de Condon sont examinées. On trouve notamment, que la susceptibilité AC devient extrêmement non linéaire en fonction de l'amplitude et que la troisième harmonique de la susceptibilité montre des valeurs exceptionnellement grandes.

Dans le dernier chapitre, les diagrammes de phase des domaines de Condon pour un échantillon d'argent puis pour un échantillon de béryllium sont expérimentalement déterminés et ensuite comparés aux prédictions théoriques.

Introduction

The present thesis investigates dia- and paramagnetic domains in metals at low temperatures called "Condon domains" or sometimes simply "diamagnetic domains". These domains, which were first predicted by Condon [3] in 1966 and two years later evidenced by Condon and Walstedt [4], are a macroscopic quantum effect due to the Landau orbital magnetism. They are one of the rare examples of magnetic domains whose origin is not the interaction of electron spins.

From a global point of view domain formation is a consequence of discontinuities in the equilibrium magnetization curve and of the demagnetization effect [10]. In the case of Condon domains the magnetization is associated with the de Haas van Alphen (dHvA) effect. The physical mechanism responsible for the discontinuity in the dHvA magnetization is the self-consistent way the induction B is built up through the "magnetic interaction" between electrons on cyclotron orbits [11]. This interaction is accounted for by using the induction B instead of the magnetic field H as the field variable in the Lifshitz-Kosevich formula [1]. Discontinuities appear in the magnetization if the amplitude of the dHvA oscillations is of the order of their period. In a finite sample with a demagnetization field this discontinuity leads to domain formation.

The "diamagnetic transition" [12] from the uniform to the domain state is analogous to the transition to the intermediate state of type-I superconductors. However, the periodical occurrence, in phase with the dHvA oscillations, is a unique feature together with the particularity that Condon domains occur up to extremely high magnetic fields, e.g. in silver up to about 45 T.

Indications for the existence of domains can be found in the waveform of various oscillating magnetic, magnetothermal, elastic and transport parameters [11]. But direct evidence has been obtained as yet only in a few cases. Condon domains were first discovered by Condon and Walstedt [4] using nuclear magnetic resonance (NMR). This work remained the only reference work in the next decades. In particular nuclear magnetic resonance was not suitable to study domains in beryllium, the very metal where anomalies in the dHvA susceptibility, magnetoresistivity and magnetothermal oscillations stimulated Condon to formulate his theory. With the development of muon spin rotation spectroscopy (μSR), domains became visible in beryllium [5] and later on in white thin, aluminum,

lead [6, 13]. By now, the appearance of Condon domains is supposed to be a general phenomenon in pure metals, with characteristic features and phase diagrams varying with the different topologies and shapes of the Fermi surface.

However, important questions concerning the size, geometry and topology of Condon domains could not be addressed with the above cited spectroscopic methods which measure only bulk properties. In this thesis we intend to measure with micro Hall probes the local magnetic induction at the surface of beryllium and silver single crystals to gain information about the size and orientation of the domain structure. The challenge in this work is to develop Hall probes that meet the requirements of spatial and magnetic resolution at low temperatures and high offset magnetic fields. In particular, a field contrast of $\Delta B/B \approx 10^{-4}$ on length scales of typically tens of micrometers should be resolved. The Condon domain structure is for the first time resolved with a local magnetic field probe. From the space resolved Hall probe measurements the domain period as well as the domain wall thickness are estimated.

Furthermore, we investigate in this thesis whether a hysteresis effect exists in the dHvA magnetization in the Condon domain state. The domain state consists of two phases of different induction values with a magnetization current in the domain walls. This needs usually extra energy. It was shown that the transition from the homogeneous to the Condon domain state is of first order [7]. At this phase transition one could in principle expect all phenomena like irreversibility, supercooling and hysteresis that exist at first order phase transitions, e.g. the liquid - gas transition. Naturally, Condon discussed these aspects in his first paper on domains [3] concluding that neither supercooling nor hysteresis had been observed in all at that time available data. Since then, these phenomena were discussed in several papers [9, 14]. In this work we will show with various highly sensitive methods that indeed a small hysteresis loop occurs in dHvA magnetization in the Condon domain state.

Phase diagrams of the Condon domain state in the temperature and magnetic field plane have been calculated using the Lifshitz-Kosevich formula for various metals [8, 9]. However, only very few experimental data exists up to now [6] which allows to verify the theoretical predictions. Experimental techniques using NMR, μSR and Hall probes measure two induction values in the domain state and this is considered as evidence for domains. To construct a phase diagram the temperature where the induction difference tends to zero must be determined as function of magnetic field. This procedure is very time consuming, expensive and not precise enough. However, the discovery of hysteresis in the Condon domain state which is easily detectable with field modulation techniques provides a simple tool which enables to find the phase boundary of the Condon domain state. Using this method experimental Condon domain phase diagrams for beryllium and silver are drawn.

Outline

The structure of this thesis is as follows: First, the basics of the Condon domain theory are outlined. Then the experimental methods and setups developed and built-up during this work, like the Hall probes and the ac susceptibility setup, are briefly introduced and characterized. In chapter 3 local magnetization measurements with Hall probe arrays, revealing Condon domains, are presented. In chapter 4 a hysteretic behavior of the dHvA magnetization is found in the Condon domain state. Several methods are used to demonstrate its existence. Finally, in chapter 5 Condon domain phase diagrams for beryllium and silver are measured using the observed hysteresis as a tool.

Chapter 1

Theory

Au cours de ce premier chapitre, on rappelle les fondamentaux de la quantification de Landau et les oscillations de l'aimantation, connues sous le nom de l'effet de Haas-van Alphen (dHvA). On montrera le mécanisme de "l'interaction magnétique" où il s'agit de remplacer le champ H par l'induction B dans la formule de Lifshitz-Kosevich. Cette interaction devient importante quand l'amplitude des oscillations dHvA est comparable à leur période. Dans ces conditions, la formation de domaines magnétiques (domaines de Condon) est énergétiquement favorable, en particulier dans une plaque (fort facteur démagnétisant). On présentera ensuite un aperçu des résultats expérimentaux obtenus jusqu'à présent et les différents enjeux de ce sujet.

In the following a short introduction to the de Haas-van Alphen (dHvA) effect is given. Then the term "magnetic interaction" (MI) is introduced which is important when the amplitude of the dHvA oscillations becomes comparable to their period. Following the argument first invoked by Condon the mechanism of magnetic domain formation is presented. Thereafter the most important experimental evidences of Condon domains are reviewed. Finally, theoretical Condon domain phase diagrams for silver and beryllium are shown.

A basic introduction to the dHvA effect can be found in nearly every textbook on solid state physics, e.g. [15, 16]. A detailed description of "Magnetic Oscillations in Metals" is given by D. Shoenberg [11]. This book is considered as reference work reviewing all important results in this field. Another extensive review is the festschrift "Electrons at the Fermi Surface" of M. Springford [17].

1.1 Landau quantization and the de Haas-van Alphen effect

dHvA and Shubnikov-de Haas oscillations are often called quantum oscillations as they are based on quantum mechanical effects. To determine the motion of an electron in a magnetic field with the induction B in z-direction, the Schrödinger equation must be solved. The energy eigenvalues are

$$E_n = \hbar\omega_c \left(j + \frac{1}{2}\right) + \frac{\hbar^2 k_z^2}{2m_e} \tag{1.1}$$

where $\omega_c = eB/m_e$ is the cyclotron frequency, $j = 0, 1, 2, \ldots$ and $k_z = 2\pi j_z/L$ with $j_z = 0, \pm 1, \pm 2, \ldots$ (L is the length of the sample). The solution of the Schrödinger equation corresponds to a harmonic oscillator with the frequency ω_c and a free motion in the z-direction. With the energy-momentum relation of a free electron gas

$$E = \frac{\hbar^2 k^2}{2m_e} \tag{1.2}$$

and $k^2 = k_\perp^2 + k_z^2$ where $k_\perp$ is the component of the k-vector which is perpendicular to the magnetic field, we obtain

$$\frac{\hbar^2 k_\perp^2}{2m_e} = \hbar\omega_c \left(j + \frac{1}{2}\right). \tag{1.3}$$

All possible states for $k_\perp$ and k_z lie on concentric cylinders with the radius $k_\perp$ which are parallel to the applied magnetic field. These are the so called Landau cylinders presented in figure 1.1. Each eigenstate for fixed j and k_z is degenerate

$$D_{jk_z} = \frac{e}{2\pi\hbar} BL^2 \tag{1.4}$$

because the number of states on a Landau cylinder is given by the number of states that would lie in the space between two Landau cylinders without an applied magnetic field.

1.1.1 Onsager relation

$A_{k_\perp} = \pi k_\perp^2$ is the enclosed area by the electrons in the k_x-k_y-plane. With equation (1.3) the cross section of the j^{th} Landau cylinder is

$$A_{kj} = \left(j + \frac{1}{2}\right) \frac{2\pi eB}{\hbar}. \tag{1.5}$$

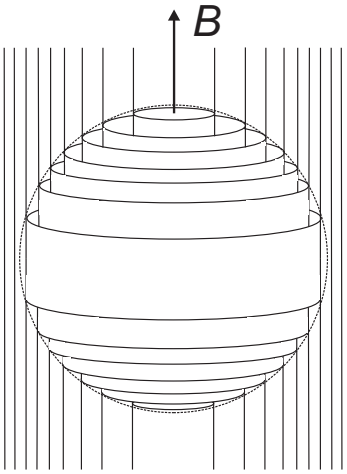

Figure 1.1: Landau cylinders in a 3D Fermi surface. The Fermi surface is indicated by the doted sphere.

As A_{kj} is proportional to the magnetic induction B, the cross section of the Landau cylinders increases with rising fields. This leads to a successive sweep of the cylinders with the allowed states out of the Fermi surface. The states outside the Fermi surface are redistributed to inner Landau levels whose degeneracy is increased. This causes oscillations in the density of states and hence in nearly all macroscopic physical properties like magnetization, electrical resistivity, and specific heat. When A_{kj} equals an extremal cross section of the Fermi surface A_{extr} a particularly great number of electrons must be reorganized. From equation (1.5) the increment of the inverse field between two passages of Landau cylinders through the Fermi surface can be derived

$$\Delta(\frac{1}{B}) = \frac{1}{B_j} - \frac{1}{B_{j+1}} = \frac{2\pi e}{\hbar A_{extr}} \tag{1.6}$$

This means that the oscillations are periodic in the inverse magnetic field. Their frequency

$$F = \frac{1}{\Delta(\frac{1}{B})}, \tag{1.7}$$

whose unity is tesla, is proportional to the extremal cross section of the Fermi surface

$$F = \frac{\hbar}{2\pi e} A_{extr}. \tag{1.8}$$

This is the Onsager relation [18] which is valid for arbitrary Fermi surfaces. If the Fermi surface has several extremal cross sections perpendicular to the applied magnetic field there are simply several frequencies in the dHvA spectra each corresponding to an extremal cross section.

1.2 Lifshitz-Kosevich formula

In 1956 I. M. Lifshitz and A. M. Kosevich [1] developed a theory describing quantitatively the oscillations of the magnetization. This theory applies up to now successfully to dHvA oscillations in three-dimensional metals. The basics of this theory are presented in this section.

1.2.1 Ideal case: zero temperature and infinite relaxation time

In most derivations of thermodynamic quantities it will be the chemical potential μ (equal to the Fermi energy at temperature $T = 0$ K), rather than the number of electrons N, which appears in the calculations. Therefore it is convenient to calculate the thermodynamic potential defined by

$$\Omega = F - \mu N. \tag{1.9}$$

The vector magnetic moment is then given by

$$\vec{M} = -\left(\mathrm{grad}_{\vec{B}}\Omega\right)_{T,\mu} \tag{1.10}$$

or in more practical terms, the components of M parallel and perpendicular to B are

$$\begin{aligned} M_{\parallel} &= -\left(\frac{\partial\Omega}{\partial B}\right)_{T,\mu} \\ M_{\perp} &= -\frac{1}{B}\left(\frac{\partial\Omega}{\partial\theta}\right)_{T,\mu,B}. \end{aligned} \tag{1.11}$$

Strictly speaking, all quantities are for arbitrary volume V; therefore M denotes magnetic moment rather than magnetization, but we shall often ignore this distinction when it is obvious what is meant.

The grand thermodynamic potential of a fermionic system is

$$\Omega = -k_B T \sum_j \ln\left(1 + \exp(\mu - E_j)/k_B T\right) \tag{1.12}$$

where the summation is over all possible states. With equation (1.4) and (1.3) the oscillating part of the thermodynamic potential is obtained after a technical calculation [1]

$$\tilde{\Omega} = -\sqrt{\frac{e^5}{8\pi^7\hbar}}\frac{B^{\frac{5}{2}}}{m_c\sqrt{A''}}\sum_{p=1}^{\infty}\frac{1}{p^{\frac{5}{2}}}\cos\left[2\pi p\left(\frac{F}{B} - \frac{1}{2}\right) \pm \frac{\pi}{4}\right] \tag{1.13}$$

where

$$A'' = \left(\frac{\partial^2 A_k}{\partial k_z^2}\right) \tag{1.14}$$

is the curvature of the Fermi surface at the extremal cross sectional area. The frequency F is given by the Onsager relation (1.8). Finally, with (1.11) the oscillating part of the magnetization can be calculated

$$\begin{aligned} \tilde{M}_{\parallel} &= -\sqrt{\frac{e^5}{2\pi^5\hbar m_e^2}}\frac{F\sqrt{B}}{m^*\sqrt{A''}}\sum_{p=1}^{\infty}\frac{1}{p^{\frac{3}{2}}}\sin\left[2\pi p\left(\frac{F}{B}-\frac{1}{2}\right)\pm\frac{\pi}{4}\right] \\ \tilde{M}_{\perp} &= -\frac{1}{F}\frac{\partial F}{\partial\theta}\tilde{M}_{\parallel}. \end{aligned} \tag{1.15}$$

The summation is over all harmonics of the dHvA oscillation and $m^* = \frac{m_c}{m_e}$ is the quotient of the cyclotron mass

$$m_c = \frac{\hbar^2}{2\pi}\frac{\mathrm{d}A}{\mathrm{d}E} \tag{1.16}$$

and the free electron mass m_e. To derive an expression for the realistic case with finite relaxation time and at finite temperatures, some damping factors must be introduced to (1.15). These factors will be presented in the next section.

1.2.2 Real case: Damping factors

Effect of finite temperature

At finite temperatures the Fermi distribution of the electronic states is smoothed by the factor k_BT. This leads to an attenuation of the amplitude as the redistribution of the electrons is also smoothed. The reduction factor

$$R_T^p = \frac{\alpha p m^*(T/B)}{\sinh\left(\alpha p m^*(T/B)\right)} \tag{1.17}$$

where

$$\alpha = \frac{2\pi^2 m_e k_B}{\hbar e} \approx 14.69\frac{\mathrm{T}}{\mathrm{K}} \tag{1.18}$$

is obtained by calculating basically the Fourier transform of the Fermi distribution [11]. Figure 1.2a shows that increasing temperature causes a strong damping of the oscillation amplitude. The oscillation amplitude increases on the other hand for high magnetic fields. From the temperature damping factor the effective mass can be calculated when the amplitude of the oscillations is plotted as a function of temperature for a fixed magnetic field.

Effect of finite relaxation time

Due to defects in the crystal the electron stay only a finite time τ on their orbits. Then they are scattered. This results in an energy uncertainty of $\hbar/\tau$ leading to a smearing of

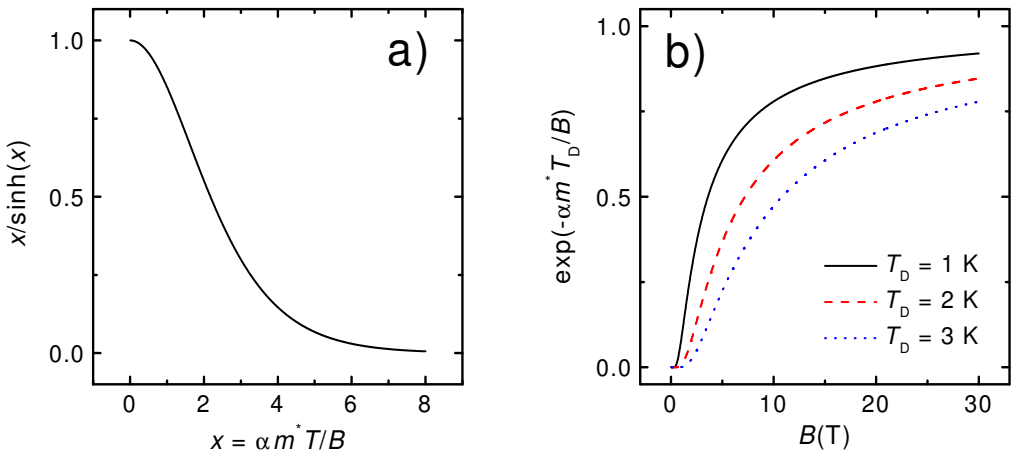

Figure 1.2: Amplitude reduction factors due to (a) finite temperature and (b) finite relaxation time (calculated for beryllium $\alpha = 14.69$ T/K and $m^* = 0.17$).

the Landau cylinders. The effect of finite relaxation time is equivalent to a temperature increase of T_D (Dingle temperature [19]). A similar calculation as for the temperature damping factor yields the so called Dingle factor

$$R_D^p = \exp\left(-\alpha p m^* (T_D/B)\right) \tag{1.19}$$

where

$$T_D = \frac{\hbar}{2\pi k_B \tau}. \tag{1.20}$$

The Dingle temperature is a measure for the crystalline quality of the sample. Figure 1.2b shows its influence on the oscillation amplitude. When the effective mass is known, T_D can be determined from the field dependence of the amplitude at a fixed temperature.

Effect of electron spin

The magnetic field lifts the spin degeneracy. Each Landau level with the energy ϵ is split into two levels with

$$\epsilon \pm \frac{1}{2} g \mu_B B \tag{1.21}$$

where $\mu_B = e\hbar/m_e$ is the Bohr magneton and g the spin-splitting factor ($g = 2.0023$ for free electrons). The two sets of shifted Landau cylinders create oscillations with a different phase. This leads to the damping factor

$$R_S^p = \cos \frac{p\pi g m^*}{2}. \tag{1.22}$$

Lifshitz-Kosevich formula

The final formula for the oscillating part of the magnetization is obtained after insertion of the reduction factors (1.17), (1.19), and (1.22) into the 'ideal' formula (1.15)

$$\begin{aligned}\tilde{M}_{\parallel} &= -\sqrt{\frac{e^5}{2\pi^5\hbar m_e^2}}\frac{F\sqrt{B}}{m^*\sqrt{A''}}\sum_{p=1}^{\infty}R_T^pR_D^pR_S^p\frac{1}{p^{\frac{3}{2}}}\sin\left[2\pi p\left(\frac{F}{B}-\frac{1}{2}\right)\pm\frac{\pi}{4}\right]\\ \tilde{M}_{\perp} &= -\frac{1}{F}\frac{\partial F}{\partial\theta}\tilde{M}_{\parallel}.\end{aligned} \tag{1.23}$$

This is the Lifshitz-Kosevich (LK) formula. In general, Fermi surfaces can be complicated and usually there might be more than one cross section of extremal area for a given field direction. Thus, the total oscillatory quantity is the sum of a number of contributions, each of which has the LK form but with different sets of parameters.

1.3 Magnetic interaction (MI)

So far the basic formulas of the dHvA effect have been introduced as function of the induction B assuming that the electrons experience B and thus the Landau quantization occurs. Historically all formulas were derived as function of the magnetic field H [1]. This difference might seem to be negligible as the oscillating magnetization $\tilde{M}$ is always small compared to the applied magnetic field and hence $B \simeq \mu_0 H$. In the following it will be shown that $\tilde{M}$ can create under certain conditions a kind of 'feedback' effect which will modify the line shape of the dHvA oscillations. Then the influence of the sample shape and thus the demagnetization field $-\mu_0 N\tilde{M}$, where N is the demagnetization factor, will be studied.

1.3.1 Shoenberg effect for an infinite sample

Shoenberg [2] noticed a appreciable deformation of the sinusoidal line shape of the dHvA oscillations in gold. The magnetization showed a left-right anisotropy and the susceptibility $\mathrm{d}\tilde{M}/\mathrm{d}H$ an up-down asymmetry. He proposed to replace the magnetic field in the original LK-formula by the induction B as the electrons experience the induction rather than the magnetic field. This apparently unimportant replacement could explain his observation on gold. It was Pippard [20] who confirmed with an thermodynamical argument that indeed H must be replaced by B in the LK-formula. As this effect was first discovered by Shoenberg in gold it is often called 'Shoenberg effect'.

To determine the conditions where the difference between B and H, i.e. the oscillating magnetization $\tilde{M}$, might modify the dHvA line shape, we take the fundamental contribution ($p = 1$) of the LK-formula (1.23) in its original version as function of the applied

magnetic field H. As we are usually concerned with only a few periods of oscillations, it is convenient to write

$$H = H_0 + h \quad \text{and} \quad B = \mu_0 H_0 + b \tag{1.24}$$

where h and b are small increments to H_0. The LK-formula then writes

$$\tilde{M} = \widehat{A} \sin\left(2\pi \frac{F}{\mu_0 H}\right) = A \sin\left(2\pi \frac{F}{\mu_0 H_0^2} h\right). \tag{1.25}$$

Since for the present we ignore complications of shape and suppose the sample is a long rod oriented along the field, we may put

$$B = \mu_0(H + \tilde{M}) \quad \text{or} \quad b = \mu_0(h + \tilde{M}) \tag{1.26}$$

and we need not distinguish between H and the field H_a of the magnet. Replacing H by the induction B leads to a sort of self-consistency or implicit equation

$$\tilde{M} = \tilde{M}(\mu_0(H + \tilde{M})) = A \sin k \left(\mu_0(h + \tilde{M})\right) \tag{1.27}$$

where

$$k = 2\pi \frac{F}{(\mu_0 H_0)^2}. \tag{1.28}$$

The criterion for the 'feedback' to change the line shape of the dHvA oscillations is that the extra term in the argument of the sin-term becomes appreciable

$$k\mu_0 \tilde{M} \simeq 1. \tag{1.29}$$

This means that the amplitude of the oscillating magnetization $\mu_0 \tilde{M}$ should become comparable to the dHvA period $(\mu_0 H)^2/F$. Even though $\tilde{M}$ is never of the order of H it can indeed become in practical situation, i.e. in high magnetic field and low temperatures, comparable to the dHvA oscillation period. This criterion can be more conveniently expressed in terms of the differential susceptibility

$$\mu_0 \left| \frac{\partial \tilde{M}}{\partial B} \right| \geq 1 \tag{1.30}$$

Shoenberg [11] introduced for this critical parameter a 'reduced' notation which is widely used

$$a \equiv \mu_0 \left| \frac{\partial \tilde{M}}{\partial B} \right| = kA. \tag{1.31}$$

The implicit equation (1.27) can be solved by a graphical construction in which each point of the graph

$$\tilde{M} = A \sin(k\mu_0 h) \tag{1.32}$$

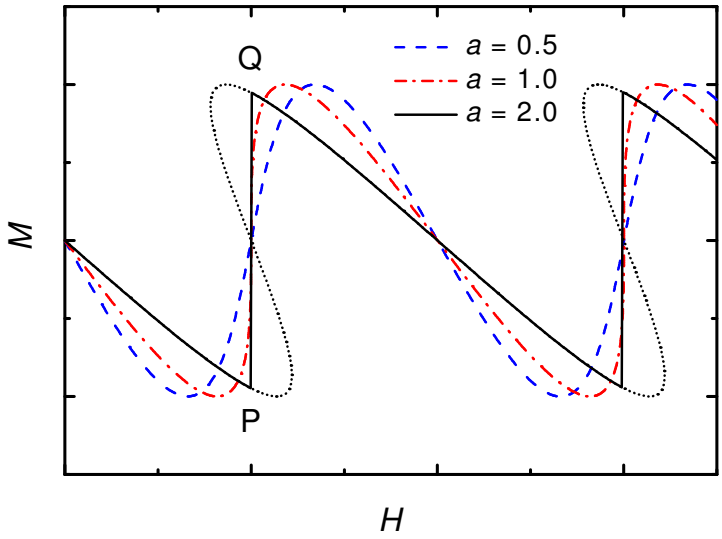

Figure 1.3: Line shape of $M(H)$. The sinusoidal wave form is more and more distorted as a increases. When $a > 1$ the oscillation becomes multivalued and a sudden jump of the magnetization occurs.

is shifted in the negative h direction by a distance equal to $k\mu_0\tilde{M}$. Figure 1.3 shows that the originally sinusoidal line shape becomes more and more distorted as a increases. For $a > 1$ $\tilde{M}(H)$ becomes multivalued in some part of each dHvA period. Naturally, the wavy line shape of $a = 2$ is not realized. The points on the curve between P and Q are thermodynamically instable. In fact, M jumps discontinuously at a critical applied field from P to Q. This jump occurs periodically in each dHvA oscillation.

Figure 1.4 shows for comparison $B(H)$ for low (a) and high (b) magnetic interaction. The situation is basically the same. For $a > 1$ $B(H)$ becomes multivalued in some part of the dHvA oscillation. In this region

$$\mu_0 \partial H/\partial B = 1 - a < 0 \quad \text{for} \quad a > 1. \tag{1.33}$$

This implies that these section are thermodynamically instable. The instability is avoided by a discontinuous jump at a given critical field H of $\delta B = B_2 - B_1$ leaving out all induction values between B_1 and B_2. The $H - B$ diagram is similar to the $p - V$ diagram of a van der Waals gas for the gas-liquid phase transition.

For $a \gg 1$ the $B(H)$ curve assumes the form of a staircase. The triangular magnetization curve in this limit is very similar to magnetization curve of a superconductor, even though of course the magnetization of a superconductor disappears at the critical field, so that there is no periodic continuation outside the range indicated. This similarity will be helpful when we will consider sample shape effects.

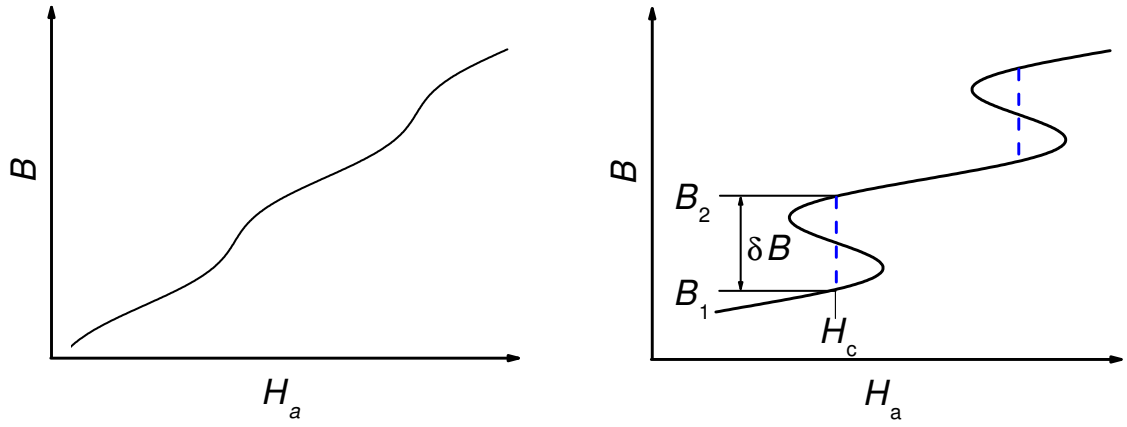

Figure 1.4: $B-H$ diagram for small (a) and high (b) magnetic interaction. For high MI ($a > 1$) B becomes a multivalued function of H. These regions are thermodynamical instable. The systems undergoes a discontinuous jump at a critical magnetic field H_c leaving out all inductions between B_1 and B_2.

1.3.2 Energy argument

It was *ad hoc* claimed above that the multivalued parts of the dHvA oscillation were thermodynamical instable and that $M(H)$ and $B(H)$ jump at a critical magnetic field. To understand this behavior figure 1.5 shows a graphical presentation of the energies involved in the system. We emphasize that we are still dealing with an infinite sample oriented along the magnetic field.

The parabola E_{mag} is the magnetization energy per unit volume caused by the difference $B - \mu_0 H$ in the sample.

$$E_{mag} = \frac{1}{2\mu_0}(B - \mu_0 H)^2 \tag{1.34}$$

E_{osc} is the oscillating energy described by the LK-formula. Here we take only the simplest approximation necessary to explain the phenomenon

$$E_{osc} = e\cos(2\pi F/B) \tag{1.35}$$

Figure 1.5a shows separately both energies as function of B for a given applied magnetic field H_0. Figure 1.5b shows the sum of both contributions. The sample will always assume the state with the lowest energy. This state is given when the B-derivative of the total energy vanishes

$$\frac{\partial E_{osc}}{\partial B} + \frac{1}{\mu_0}(B - \mu_0 H) = 0. \tag{1.36}$$

This leads to the well known expression for the magnetic moment $M(B) \equiv -\partial E_{osc}/\partial B$. Usually, only one minimum of the total energy exists for a given applied magnetic field.

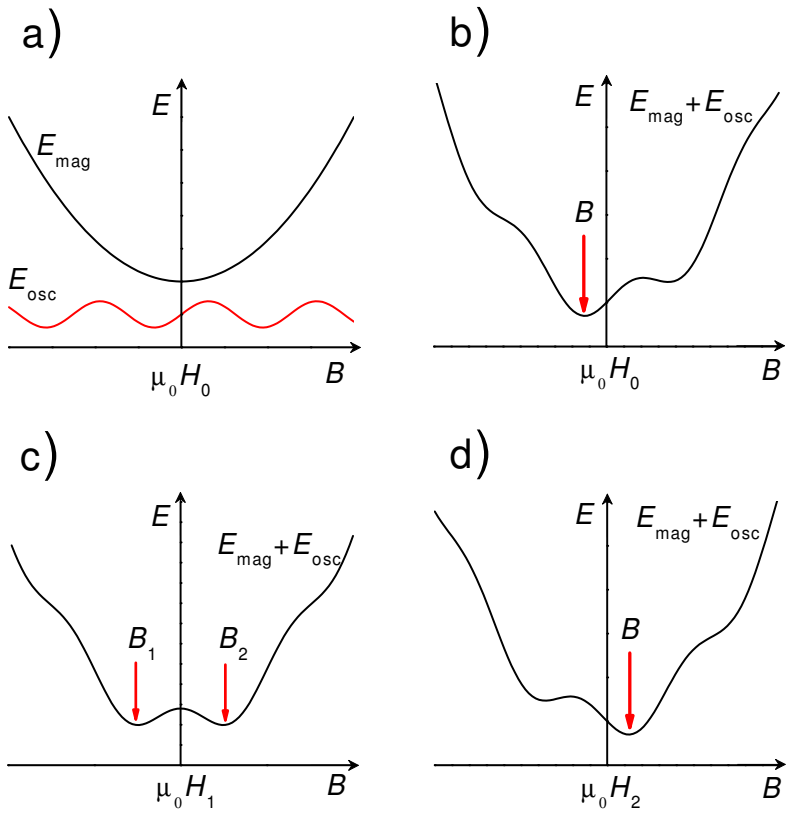

Figure 1.5: Schematic representation of the magnetization energy E_{mag} and the dHvA energy E_{osc} as function of B for several applied magnetic fields. If the curvature of the parabola is smaller than the curvature of the oscillating energy two minima coexist. This leads to discontinuous jump of the induction.

In fact, the curvature of the parabola $E_{mag} = 1/\mu_0$ is normally bigger than the curvature of the oscillating energy E_{osc} so that the second B-derivative is positive

$$\frac{\partial^2 E_{osc}}{\partial B^2} + \frac{1}{\mu_0} > 0. \tag{1.37}$$

This leads finally to the stability condition

$$\mu_0 \frac{\partial M}{\partial B} < 1. \tag{1.38}$$

If on the other hand the curvature of the parabola E_{mag} is smaller than the curvature of E_{osc}, i.e.

$$\mu_0 \frac{\partial M}{\partial B} > 1, \tag{1.39}$$

two values of the induction B_1 and B_2 may coexist (see figure 1.5c. The condition for this instability is the same as already found above in (1.30). When the applied field is then

swept to $\mu_0 H_2$, shown in figure 1.5d, there is once again only one minimum in the total energy for a single induction B. This explains the discontinuous jump in the induction. As soon as the applied magnetic field crosses the point $\mu_0 H_1$, the induction jumps from B_1 to B_2; or in terms of magnetization from M_1 to M_2.

1.3.3 Demagnetization field in finite samples

Up to now only infinite samples were considered so that demagnetization effects could be neglected. For simplicity we will consider in this chapter only ellipsoidal shaped samples, so that if the external field H_a is uniform over all space, M and B will be uniform within the sample. The predicted results will still be qualitatively valid even if the sample is not a perfect ellipsoid but generally the dHvA amplitude will be reduced due to phase smearing.

If the magnetic field $\mathbf{H_a}$ is applied parallel to one of the principal axes of the ellipsoid the demagnetization tensor n_{ij} is purely diagonal and reduces to a simple factor which can be introduced in equation (1.26)

$$B = \mu_0 H_a + \mu_0 (1 - n)\tilde{M}. \tag{1.40}$$

The additional factor $(1 - n)$ seems to weaken the magnetic interaction, and indeed to eliminate it altogether in the limiting case of a disc shaped sample with $\mathbf{H_a}$ normal to its plane, for which $n = 1$. It was found by Condon [3] that this is only true if the homogeneously magnetized state is indeed that of the lowest free energy. It turned out that if MI is strong enough, a state of lower free energy can be achieved over an part of the oscillation cycle by the sample breaking up into domains. In these domains the local value of M alternates in sign from one domain to the next. This can be explained, following Condon, if we think of the sample as made up of many parallel thin rods along the field direction. Each of these rods experiences the field $H_a - \mu_0 n\tilde{M}$ rather than H_a and so, if $a > 1$, can exist at the discontinuity in figure 1.3 in either of two states P or Q of equal free energy. For a finite demagnetization factor, the field

$$H_a - n\tilde{M} = \text{const.} \tag{1.41}$$

can stay constant at this critical value as H_a increases, provided $\tilde{M}$ varies. Along the line PQ in figure 1.6 the sample volume will be broken up into domains, with an increasing proportion of $+$ rather than $-$ domains as we go along PQ until 100% is reached at Q. Over this domain part of the magnetization curve the observed $\tilde{M}$ is an average value. The values in the individual domains, as indicated in figure 1.8 are those at P and Q.

The total energy was sketched above to explain the jump in the induction. Let us consider now domain formation in this model. For simplicity we consider the limiting case of a plate-like sample with an demagnetization factor of $N = 1$. In this case we have

$$\mu_0 H_a = B. \tag{1.42}$$

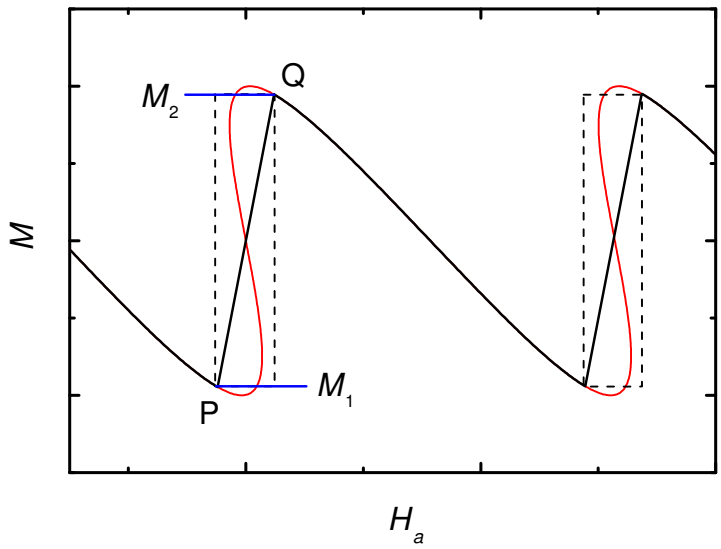

Figure 1.6: Shape effect on magnetic oscillation form for $a > 1$ and $n = 0.7$. The sample breaks up into domains between P and Q, and the average magnetization follows the straight line PQ with the slope $1/n$.

This implies that the induction can not jump as discussed above for infinite samples because the applied magnetic field is usually smoothly swept. As $B - \mu_0 H_a = 0$ we can omit the parabola E_{mag} in figure 1.5a. As a result, only the oscillating energy E_{osc} remains. Figure 1.7 shows that over a large range of magnetic field in the vicinity of H_0 the energy of the metal becomes considerably higher than the minimal value realized in a infinite sample where the metal could always choose the induction of minimal total energy. Condon showed that in a plate-like sample the energy can be lowered by δE by dividing the plate into a set of thin regions - domains. Let their length, which is the sample thickness, be much larger than the domain width. In this case a domain looks like a long cylinder oriented along the field. That is why we can apply the above discussed energy considerations (see figure 1.5) on each domain. The domains can hence exist with two induction values B_1 and B_2. The volume fraction of the respective domains is then arranged that the average induction over the whole sample is equal to the applied magnetic field. Calculations show that the formation of domains with constant induction B_1 and B_2 respectively becomes more favorable than the homogeneous state for applied magnetic fields $B_1 < \mu_0 H_a < B_2$. This gain is shown in figure 1.7 by the dashed line.

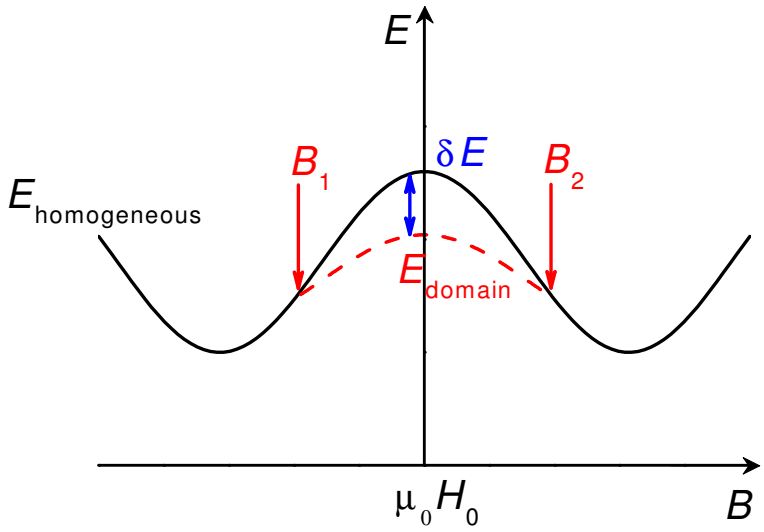

Figure 1.7: In a plate-like sample only the oscillating energy is considered as $\mu_0 H_a = B$. The energy can be lowered by δE by the formation of domains with respective inductions B_1 and B_2 for applied magnetic fields $B_1 < \mu_0 H_a < B_2$.

1.4 Domain structure

The size and shape of Condon domains are governed by considerations very similar to those in other domain structures, e.g. domains in ferromagnets and intermediate state domains in type-I superconductors [21, 22]. The total free energy in thermodynamic equilibrium should be a minimum. Therefore, the sum of the surface energy of the domain walls and on the other hand the energy of emergence of the domains at the surface or magnetostatic energy of the sample must be minimized. These energies depend considerably on the actual shape and size of the sample. In the simplest case of a flat plate-like sample of thickness t, the domains may in principle form parallel layers across the sample from one surface to the other with a domain periodicity p (see figure 1.8). In the following we will consider this case.

There are no detailed calculations of the surface energy of the domain walls but the order of magnitude can be estimated by considering the electron orbits which are in the domain wall and experience a non-uniform field. There is certainly not a sharp reversal of the magnetization because this would create a drift current along the domain wall. This drift current would then be distributed over a thickness of roughly two electron orbits, and hence the change in the induction can not be abrupt. The electrons in the wall have quantized orbits but in average with a higher energy level, corresponding to the maximum of $E_{hom.}$ in figure 1.7, than the electrons in the body of the domains (corresponding to the energy at B_1 and B_2 in figure 1.7). This is the origin of the excess surface energy of

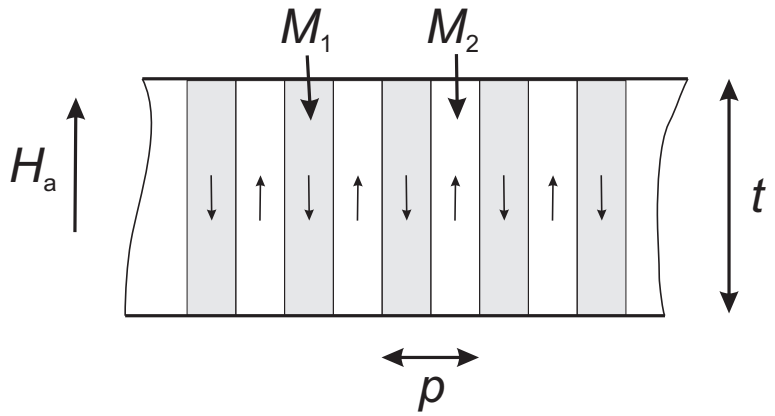

Figure 1.8: Simplest model for a domain structure. Domains with magnetization M_1 and M_2 coexist in a thin sample. t is the thickness of the sample and p the period of the domain structure.

the domain walls. One can estimate its order of magnitude to be roughly $\delta E \approx \alpha H_0 M_2$ times the thickness of the domain wall w. $H_0 M_2$ is the amplitude of the energy variations in figure 1.7 and α is a numerical constant of order unity. The surface energy of the $1/p$ domain walls per unit volume of the sample is then

$$E_{wall} = \alpha w H_0 M_2 \frac{1}{p}. \tag{1.43}$$

The magnetostatic energy of the domain configuration shown in figure 1.8 has been calculated before in connection with the ferromagnetic problem [22]. The magnetostatic energy per unit volume is

$$E_{mag} = \beta H_0 M_2 \frac{p}{t} \tag{1.44}$$

where β is another numerical constant of order unity. The sum of these two energies has, as a function of p, a minimum when p is

$$p = \sqrt{\frac{\alpha}{\beta} wt} \propto \sqrt{wt}. \tag{1.45}$$

The scale of the domain pattern, p, is roughly the geometric mean between the sample thickness and the domain wall thickness. In a brief abstract Condon [23] refers to a more relevant calculation, but gives no details except that the wall thickness is about two cyclotron orbit diameters and the surface energy is positive.

The cyclotron radius is approximately 10 μm for beryllium at 2.3 T and silver at 9.0 T. For a sample with a thickness of about 1 mm, we find a domain pattern size of about 30 μm. The magnetization M_1 and M_2 of the domains in figure 1.8, was measured with μSR on beryllium to be roughly $\pm$20 G at 2 T and 0.5 K [5]. These estimations are important for the design of the domain vizualization experiment.

1.5 Experimental evidence for Condon domains

Condon's first experiments [3] indirectly confirmed the existence of domains in beryllium. Jumps in the magnetization were observed for a rod-shaped sample in an applied field parallel to the long axis. On the other hand the magnetization of a disc in a perpendicular applied field approached the limiting form, discussed above, with two similar slopes on both sides of the oscillation.

In 1968 Condon and Walstedt [4] found direct evidence for the existence of magnetic domains in silver. Nuclear magnetic resonance (NMR) measurements at 1.4 K showed a split in the resonance line corresponding to domains with different magnetic induction (see figure 1.9). A local field difference of about 12 G was observed between the paramagnetic and diamagnetic domains in a magnetic field of 9 T. As the conductivity of silver is very high at these low temperatures, the high frequencies (18 MHz) used for the NMR measurements can not penetrate more than the skin depth into the sample. The skin depth is here of the order of some micrometers so that the induction splitting was essentially observed at the surface of the silver sample. Therefore, this result is encouraging for domain imaging attempts with magnetic probes at the sample surface. In [4] the authors attempted similar experiments on a beryllium sample but the long nuclear thermalization time and the nuclear quadrupole splitting made the measurements and their interpretation difficult. Thus, this pioneering result remained the only reference work in the next decades.

New experimental possibilities appeared with the development of muon spin rotation (μSR) [24]. Muons are unstable elementary particles with a lifetime of about two microseconds. A muon with sufficiently high initial energy, can penetrate into the sample to a fairly large depth. Its spin precesses in exact correspondence with the local value of magnetic induction. The decay of a muon creates a positron which rushes out mostly in the direction of its spin, i.e. the direction of the muon spin when it decayed. The positron is detected by detectors situated around the sample. In the experiment, a great number of muons is used, with all their spins rotating from strictly the same starting position. If all muons are in the same magnetic field, then the number of registered events in each direction will vary with time with the muon precession frequency f, which determines exactly the magnitude of the magnetic induction, i.e. $f = gB$, where the constant g is well known for muons.

As early as in 1979, Yu. Belousov and V. Smilga [26] suggested to use μSR for the observation of Condon domains. In 1996 the idea was finally carried out and G. Solt *et al.* [5] evidenced successfully Condon domains in beryllium by μSR at the Paul Scherrer Institute in Switzerland. A splitting of the μSR peak, similar to that observed by NMR, caused by Condon domain formation, was observed at 2.7 T and 800 mK.

The μSR method, in spite of its direct analogy with NMR, has, of course, a number of distinctions as well. This method needs no ac electromagnetic field since the precession frequency is measured directly, and therefore the first difficulty of NMR measurements

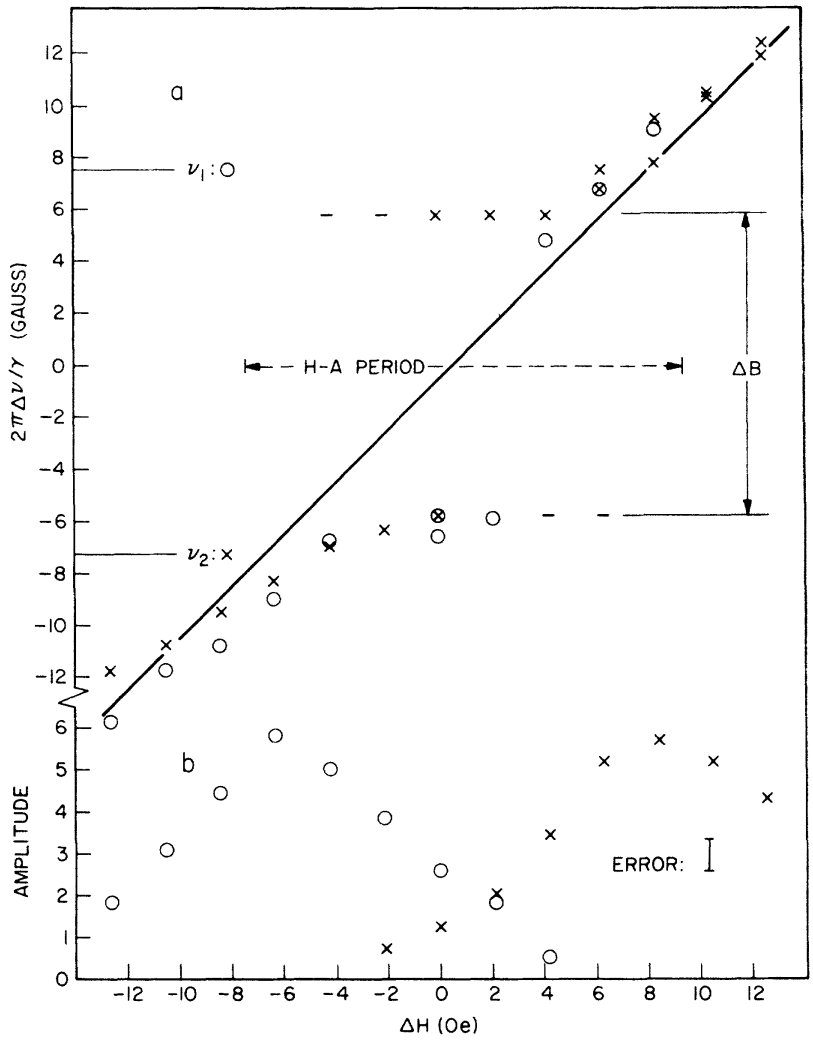

Figure 1.9: NMR results on silver from [4]. (a) Induction values as function of the applied magnetic field of 9 T at 1.4 K. Around $\Delta H = 0$ two inductions separated by $\Delta B = 12$ G are observed. This indicates the presence of domains. (b) Shows the variation of the resonance line amplitude in the domain region which corresponds to the respective domain volumes.

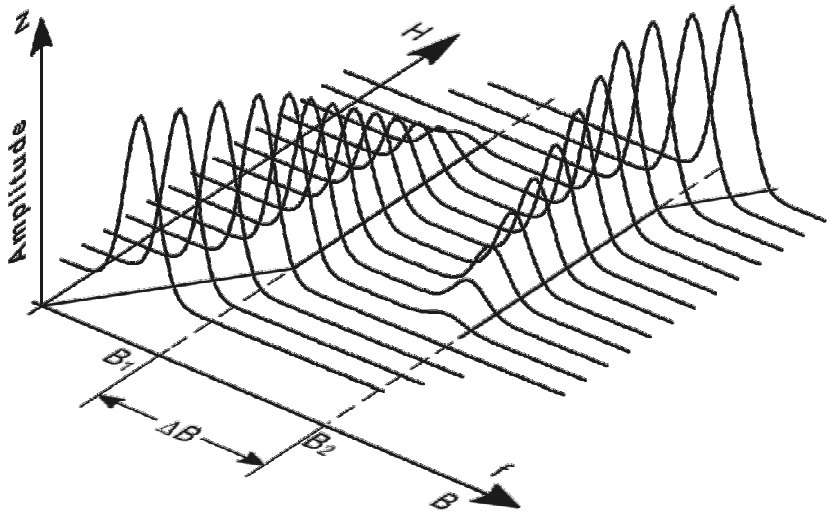

Figure 1.10: Schematic representation of several μSR spectra over a small region of applied magnetic field H near the onset of Condon domains [25]. In the domain region two peaks at B_1 and B_2 coexist.

caused by the small skin layer does not exist. Furthermore, all metals can be investigated, in contrast to NMR, where troublesome quadrupole broadening occurs for nuclear spins $I > 1/2$. The fact that spin precession occurs far enough from the sample surface, represents the third important advantage of this method.

As a result, in analogy with NMR, the width of μSR peak corresponds to the amplitude of magnetic induction inhomogeneity. If now the sample becomes stratified into two phases with the induction values B_1 and B_2, then one part of muons will find themselves in the field B_1 and the other part - in the field B_2, which will result in two precession frequencies and therefore in a splitting of the μSR peak into two peaks. Figure 1.10 demonstrates the results of μSR experiment on a crystalline plate of beryllium. Each time when H goes through the region $B_1 < \mu_0 H < B_2$, the spectrum splits into two peaks with the frequencies corresponding to B_1 and B_2. While the field changes, the amplitude of one peak decreases and the amplitude of the other increases, which corresponds to the change of the relative volumes occupied by these two phases. At any other values of magnetic field beyond the given range, a standard narrow peak is observed.

It was quite natural that Condon domains were evidenced successfully in beryllium as, due to its quasi two dimensional Fermi surface, the dHvA amplitude is the highest of all metals. At the same time the dHvA period is not too big so that equation (1.30) is verified for temperatures up to 3 K (see section 1.7.2). A systematic study of domain parameters in beryllium in function of temperature and magnetic field was possible with μSR [27, 28, 29].

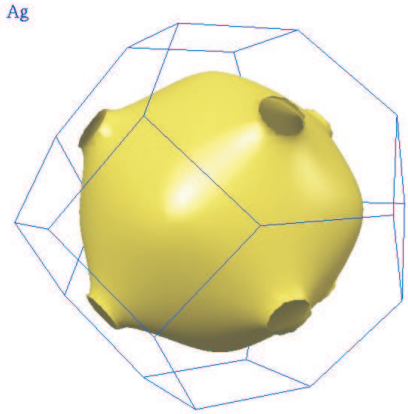

Figure 1.11: Fermi surface of silver within a single zone [33]. The neighboring zones are joined by 'necks' in the $\langle 111 \rangle$ directions. The main 'belly' frequency is about 47500 T. The frequency of a 'neck' orbit is about 900 T. The reduced electron mass is $m^* = 0.94$.

Later on, the Condon domains were observed with μSR in other very pure single crystals of white tin [30, 31], aluminum and lead [13]. The requirements for sample purity, field and temperature allowing domain formation are much more stringent in these metals. The "state of the art" in this field has been recently reviewed [6]. By now, the phenomenon of Condon domain formation is assumed to occur in all metals.

The above discussed spectroscopic techniques give clear evidence for the existence of domains. Nevertheless, the size and topology of Condon domains are still unknown.

1.6 Silver

1.6.1 Fermi surface of silver

Monovalent metals have the simplest Fermi surfaces. Out of the monovalent metals the alkali Fermi surfaces are the simplest, departing only slightly from the ideal spherical surface of the free-electron model. The next simplest Fermi surfaces are those of the monovalent noble metals, Cu, Ag and Au. The new feature is that there are 'necks' in the extended Brillouin zone representation joining the surfaces within each separate zone in the $\langle 111 \rangle$ directions (see figure 1.11). Thus a magnetic field along $\langle 111 \rangle$ will see not only the 'belly' orbit with a high dHvA frequency of about 47500 T but also the 'neck' orbit associated with a low frequency of about 900 T [32].

Other consequences of the multiply connected Fermi surface are that there are [11]:

- a 'dog's' bone orbit normal to $\langle 110 \rangle$ with 0.4 times the belly frequency,

- a 'four-cornered rosette' orbit normal to $\langle 100 \rangle$ again with 0.4 times the belly frequency,
- a 'six-cornered rosette' normal to $\langle 111 \rangle$ with twice the belly frequency.

As the Fermi surface of silver is nearly spherical, the effective electron mass m_c is approximately equal to the free electron mass m_e, i.e. $m^* = 0.94$.

1.6.2 Theoretical phase diagram for silver

As has been shown in the previous chapter, domains can only arise at the paramagnetic part ($\partial M/\partial B > 0$) of the dHvA period. This leads to two phase transitions per dHvA period. Therefore, the Condon domain phase diagram has a comb-like structure in the (B, T) plane, with a domain region or stripe for each dHvA period. The width of the domain stripe within a dHvA period is proportional to the demagnetization factor n as described above. In this section the envelope of the comb structure is considered which separates the region with no domains from the one where uniform and domain phase alternate. A more detailed consideration of the substructure is given in the section on the phase diagram for beryllium. There, the substructure is more interesting due to the dHvA frequency beat.

In the (B, T) plane, where B is the magnetic induction and T the temperature, the boundaries between homogeneous and domain regions are determined by equation (1.30) and (1.31)

$$a(B, T, T_D) = 1 \tag{1.46}$$

where T_D is the Dingle temperature. In other words the differential susceptibility must be equal to unity

$$\chi_B(B, T, T_D) = \mu_0 \frac{\partial \tilde{M}}{\partial B} = 1. \tag{1.47}$$

This condition gives the phase boundary $T_c(B)$.

Although the amplitude of the magnetization increases like $\sqrt{B}$ for $B \to \infty$, the susceptibility has a maximum in function of magnetic field. This can be seen if one considers only the limiting cases. In the high field limit $B \to \infty$

$$\chi \propto \frac{\partial}{\partial B} \sqrt{B} \sin(2\pi \frac{F}{B}) \leq \frac{F}{B^{3/2}} \to 0. \tag{1.48}$$

In other words the period of the oscillations increases faster than their amplitude for high fields leading to vanishing susceptibility. This means that there is for every metal an upper critical field above which no domains exist for all temperatures [12].

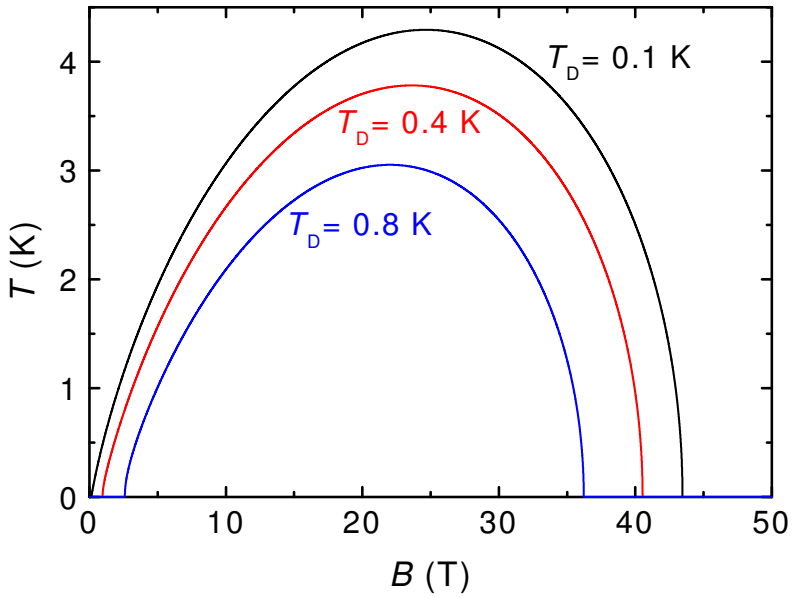

Figure 1.12: Condon domain phase diagram $T_c(B)$ for silver for several Dingle temperatures T_D calculated with the LK-formula (cf. [34]).

In the low field limit $B \to 0$

$$\chi \propto \frac{\partial}{\partial B}\sqrt{B}\exp(-\alpha p m^* \frac{T_D}{B})\sin(2\pi\frac{F}{B}) \to 0. \tag{1.49}$$

In the low field limit the magnetization amplitude decreases exponentially due to the finite sample quality of a real sample with a finite Dingle temperature. Even if the dHvA period shrinks quadratically this leads to a vanishing susceptibility. From the LK-formula it is clear that the susceptibility decreases also as the temperature is increased. In conclusion, there will be for every metal a finite region in the (B,T) plane where Condon domains arise.

The susceptibility can be calculated in absolute units with the LK-formula (1.23) if all parameters like curvature A'', effective electron mass m^* and the Dingle temperature of the sample are known. For noble metals, where the deviations from a spherical Fermi surface are only very small, these parameters have been calculated [35]. Usually only the first harmonic contribution of the LK-formula is considered. Figure 1.12 shows several phase diagrams for silver corresponding to samples with different Dingle temperatures. Up to now, there are only very few experiments that test the theoretical calculations for silver. At least the theoretical phase diagram is compatible with the NMR observations of Condon and Walstedt [4]. They observed no splitting ΔB due to domains above 2.5 K at 9 T on their high quality silver sample.

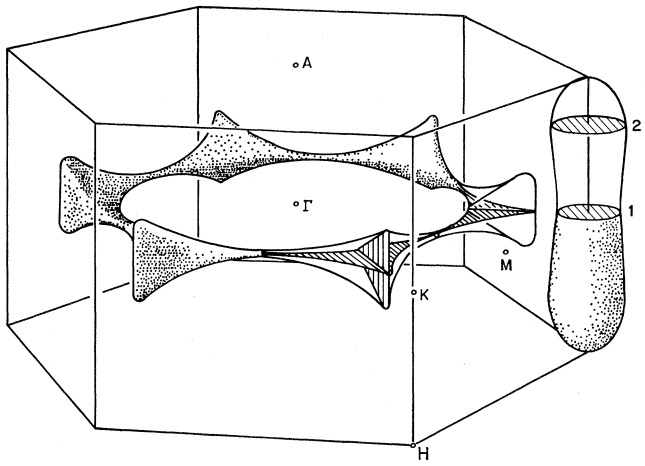

Figure 1.13: Fermi surface of beryllium [36] with the coronet and one of the two electron 'cigars'. The extremal cross sections at the 'waist' (1) and the two 'hips' (2) lead a beat in the dHvA waveform (see figure 1.14).

1.7 Beryllium

1.7.1 Fermi surface of beryllium

The Fermi surface of beryllium [37, 38], presented in figure 1.13, contains a hole region which resembles a coronet and two equivalent pockets of electrons similar in shape to a cigar. The cigar-like ellipsoids are oriented along the $[0001]$ direction and are slightly pinched in the middle forming a 'waist' and two symmetrically placed 'hips'. The cross sections A_{waist} and A_{hip} give rise to two frequencies $F_w = 942.2$ T and $F_h = 970.9$ T causing a beat in the oscillations with the frequency $F_h - F_w = 28.7$ T. Each beat cycle, i.e. between two succeeding nodes or antinodes of the magnetization beat, comprises ≈32 dHvA periods.

While the shape of the cross sections A_{waist} and A_{hip} is known, Fermi surface models have not given values for the curvature A'', which is however an important parameter in the LK formula. From the observed ratio $\approx 3:1$ of the dHvA amplitudes at beat antinodes and nodes [39] one can deduce that the curvatures at the hip and the waist are nearly equal. A simple interpolation, consistent with these features [40], leads to $A'' \approx 0.24$.

Figure 1.14 shows schematically the dHvA oscillations waveform of the magnetization and the susceptibility calculated with the LK-formula for $\mathbf{H} \parallel [0001]$. In all experiments described below the beryllium sample is usually oriented $\mathbf{H} \parallel [0001]$ because the small $m^* = 0.17$ and the small curvature along $[0001]$ result in a relatively high dHvA amplitude even at relatively high temperatures. Therefore, the differential susceptibility, which is the critical parameter for Condon domain formation, can be much higher than

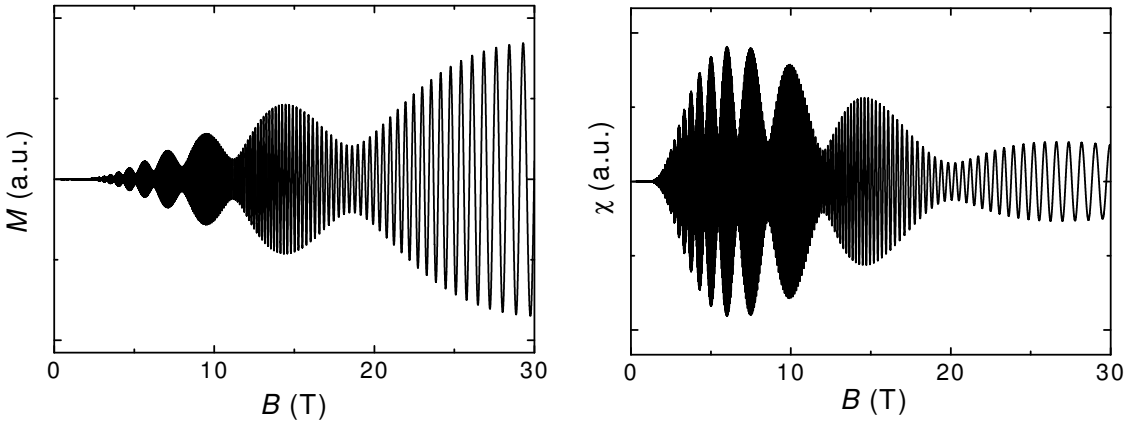

Figure 1.14: Magnetization and susceptibility waveforms of beryllium calculated with the LK-formula for $\mathbf{H} \parallel [0001]$. The frequencies $F_w = 942.2$ T and $F_h = 970.9$ T lead to a beat in the oscillations with ≈32 oscillations in each beat cycle.

unity at easily accessible (2-3 T) fields [39].

Because of the beat in the dHvA waveform in beryllium there is the unique possibility to change the dHvA amplitude and the critical parameter χ by a factor three at constant temperature by varying the magnetic field only very little. This means that one can choose the experimental conditions in a way that in a certain field range the Condon domain state arises periodically in some part of each dHvA period and just for neighboring fields, i.e. the beat minimum, the sample stays homogeneous over the hole dHvA period (see next section). This features make beryllium the best metal to investigate Condon domains.

1.7.2 Theoretical phase diagram for beryllium

The general condition $\chi_B > 1$ under which the Condon domain state arises is naturally the same for beryllium as for silver (see section 1.6.2). The differential susceptibility χ_B is calculated with the LK formula with the above parameters of the Fermi surface. Three extremal cross sections, two hips and one waist, contribute to χ_B for $\mathbf{H} \parallel [0001]$. The above described beat in the susceptibility (see figure 1.14) reappears in the phase diagram. It is convenient to calculate two phase boundary lines $T_c(B)$, one for the beat antinodes and another for the beat nodes. Figure 1.15 shows the theoretical phase diagrams for several Dingle temperatures [29].

Like in section 1.6.2 on the phase diagram for silver, figure 1.15 shows only the phase boundary below which Condon domains may arise in some part of the dHvA period. For beryllium the substructure is more sophisticated due to the dHvA beat. Figure 1.16 shows schematically the substructure. Condon domains exist only in the thin "domain stripes" reaching from $T = 0$ to $T = T_c(B)$. Between the stripes the magnetic state is uniform.

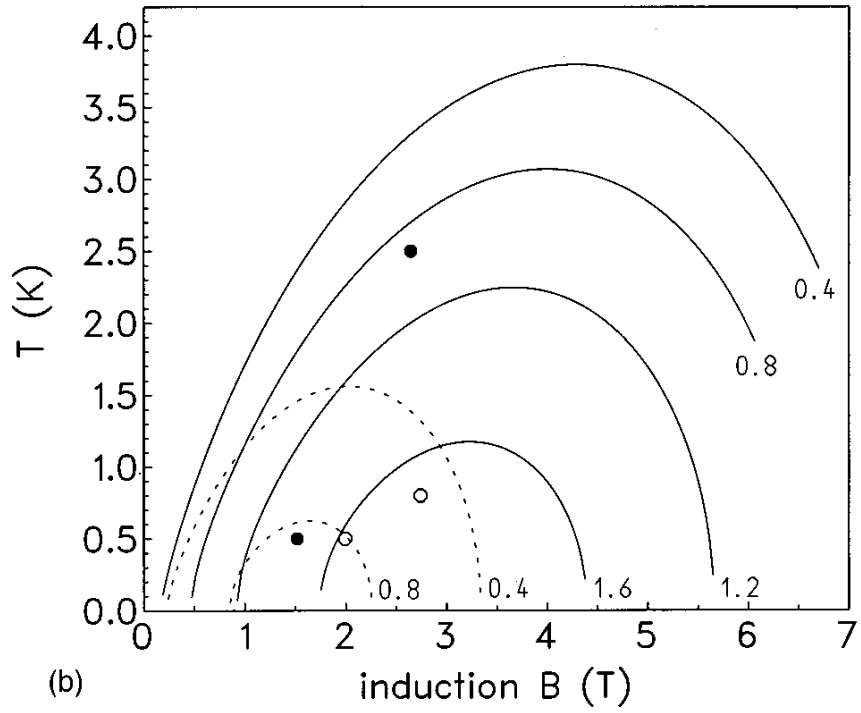

Figure 1.15: Theoretical phase diagram for beryllium for different Dingle temperatures [29]. The solid and dashed curves indicate the Condon domain state at the beat antinodes and nodes, respectively. The experimental points for two beat antinodes (•) and beat nodes (○) show observed domain phases for a sample with $T_D \approx 2.6$ K.

The phase diagram has a comb-like shape in the B-T-plane, modulated with the dHvA beat frequency. This feature enables many experimental possibilities as already discussed above.

The experimental points in figure 1.15 show that Condon domains were observed in samples of less quality ($T_D \approx 2.6$ K) in a much more extended region in the (B, T) plane than the curves, calculated by the LK formula, predict. This indicates that the susceptibility χ is underestimated by the theory. The reason is the very low curvature of the Fermi surface along the $[0001]$ direction at the extremal cross sections. In fact, the curvature factor in the LK formula is only a reminder of a power expansion of $A(k)$ stopped at the quadratic term. For low curvature this approximation is no longer valid. Higher contributions need to be considered.

On the other hand, as the cross section A varies only very little along $[0001]$ the susceptibility can be estimated by taking the Fermi surface as a cylinder, i.e. a 2D electron gas [12, 41]. This approach gives reasonable upper limits for χ and for the phase boundary $T_c(B)$. Nevertheless, there are some obvious shortcomings besides the poor precision like

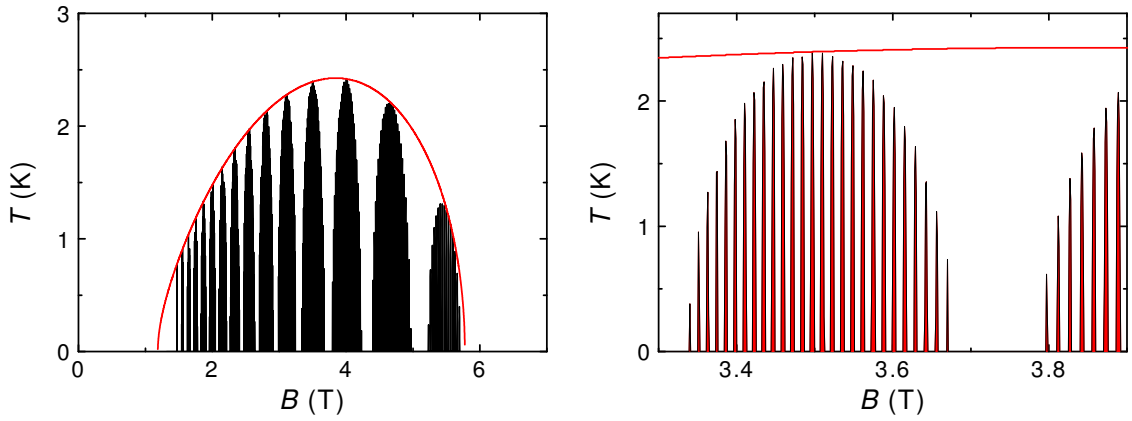

Figure 1.16: Schematic phase diagram for beryllium for $T_D \approx 1.2$ showing in detail the beat substructure under the envelopes of figure 1.15. Domains occur only at the paramagnetic part of the dHvA oscillations. This leads to a comb-like substructure in the (B, T) plane.

e.g. that the beat in χ can not be reproduced.

Recently, $\chi(B, T)$ has been calculated in the frame of a model beyond the LK formula and consistent with the 3D character and available information of the Fermi surface of beryllium [8]. In this model the cross section $A(k)$ is approximated with power laws and polynomial forms up the the eighth order. The obtained phase diagram is in good agreement with at that time available μSR data [6].

Chapter 2

Methods

Les dispositifs expérimentaux et l'instrumentation sont présentés dans ce chapitre. Les conditions expérimentales pour l'observation des domaines de Condon nécessitent basses températures et champs magnétiques intenses (cf. partie 1.7.2 et partie 1.6.2). On expliquera ici le dispositif cryogénique et les différents types de bobines de champ magnétique utilisées. Pour mesurer l'hystérèse dans l'effet dHvA, nous avons utilisé la susceptibilité AC, détectée par la méthode de mutuelle inductance. Pour détecter directement les domaines de Condon, le sujet majeur de cette thèse, nous avons développé des microsondes de Hall, afin d'obtenir les résolutions spatiale et magnétique nécessaires. Dans ce chapitre sont discutés quelques aspects concernant l'effet de Hall et le choix du matériau utilisé dans les différentes évolutions des sondes de Hall.

In this chapter the experimental setups and measurement devices used during this work are presented. From the phase diagrams for the Condon domain state in silver and beryllium (see section 1.7.2 and 1.6.2) one can see that the experiments need to be performed at low temperatures and high magnetic fields; considerably higher fields for silver. Therefore, first the cryogenic equipment and magnet systems are briefly introduced. A standard ac modulation coil method was used for the experiments on hysteresis effects in the Condon domain state and for the determination of the phase diagrams. The basic principles of this method are summarized and its realization is presented. Finally, after a short introduction to the magnetic and spatial resolution of a Hall probe, the Hall probe setups and their evolutions realized during this work are shown. It turned out that the appropriate choice of the Hall probe material and the spatial arrangement was decisive for a successful observation of Condon domains on silver. Therefore the Hall probe setups and a test of their spatial resolution are discussed in detail.

2.1 General

2.1.1 Cryogenic equipment

Most of the experiments were carried out in a ^{4}helium bath cryostat. The cryostat has a tail which fits to the room temperature bore of the magnet. In the tail a diameter of 38 mm is available for the insert with the experiment. The temperature is varied by changing the vapor pressure above the ^{4}helium bath. The vapor pressure of ^{4}helium increases exponentially with temperature. In these cryostats temperatures between 1.3 K and 4.2 K are typically accessible. The lowest temperature is given by the pump rate. On our magnet site (T02) two rotary vane vacuum pumps with each a pump speed of 65 m^3/h and a roots vacuum pump are available. A pressure gauge measures the actual vapor pressure and the temperature is determined via the ITS 90 temperature scale [42]. This way to measure the temperature is particularly convenient when magnetic fields are applied. As commercial resistive thermometers, made e.g. of ruthenium oxide, show more or less pronounced magneto resistance. The vapor pressure however is independent from the applied magnetic field. The temperature of the ^{4}helium bath could be stabilized by keeping a constant pressure by means of a membrane valve.

On our magnet site (T02) the cryostat which houses the superconducting magnet and the cryostat for the sample are completely independent. This has several advantages. First, the sample cryostat, whose tail fits in a 50 mm bore, can be used also on the resistive magnet sites of the laboratory. Secondly, the temperature of the sample cryostat can be varied independently from the huge magnet cryostat volume.

The experiments for the Condon domain phase diagrams where partly carried out in the laboratory of Laurent Levy where an Oxford variable temperature insert (VTI) is available. The VTI is fitted in the ^{4}helium bath cryostat of the superconducting coil. Helium is aspirated from the bath through a thin capillary by pumping on the VTI cryostat. The flow trough the capillary can be adjusted by a needle valve. The insert with the experiment is cooled by the cold helium gas stream. The temperature is kept stable by a temperature controller using a heater in order to control the temperature at the position of the experiment. In the VTI temperatures between 1.5 K and room temperature are available. Another advantage of the VTI is that temperature sweeps can be realized very comfortably at a given magnetic field, which was very useful for the phase diagram measurements.

2.1.2 Magnet systems

Magnetic fields with a high spatial homogeneity are required to measure dHvA oscillations. The magnetic field should be constant over the dimensions of the sample. If this

condition is not fulfilled, the electrons experience different magnetic fields and hence the resulting dHvA oscillations are slightly shifted in phase. A small phase shift or phase smearing leads to a considerable decrease of the overall dHvA amplitude. For the experiments to visualize Condon domains, in addition to the high spatial homogeneity, a high temporal stability of the applied magnetic field is required. At least during the time, necessary to read out all Hall probes or to accomplish a scan of the sample surface, the magnetic field should be stable.

These requirements are very well fulfilled by superconducting magnets. Due to their high inductance only slow fluctuations of the magnetic field are possible. Moreover the coils can be wound in a way that the produced magnetic field has a high homogeneity. Unfortunately superconducting magnets are limited by their maximum fields (about 17 T available in the GHMFL in 2005). Higher fields have to be produced by resistive magnets or hybrid magnets that incorporate a superconducting and a resistive part.

Superconducting magnets

Most of the results of this thesis were measured in an Oxford 10 T superconducting coil. The coil, being actually a NMR coil, had a high spatial homogeneity of better than 10 ppm (parts per million) in a sphere with a diameter of 1 cm. The magnet with an inductance of 11.8 H had a 60 mm warm bore in which a water-cooled modulation coil is fit. A standard 50 mm ^{4}helium cryostat was installed in the remaining space of the room temperature bore. This coil had no switch so that the magnet power supply had to be always connected to the coil and a persistent mode was not possible. Nevertheless, only very small temporal drifts or fluctuations of the magnetic field were observed due to the high stability ($<$ 30 ppm/hour) of the magnet power supply (Oxford PS 126 HS). In principle the magnet could be pushed even to 12 T if the temperature was lowered to 2.2 K by pumping on the lambda plate. This possibility was never used because of the high investment in time and helium.

Some susceptibility measurements on silver were carried out in the laboratory of Laurent Levy. There, the coil is slightly less homogenous (30 ppm in a 1 cm^3 sphere) but the maximum available field is of about 17 T.

Resistive magnets

With resistive magnets, maximum fields of 31 T have been reached in a 50 mm warm bore at the GHMFL. A hybrid magnet that should allow to attain magnetic fields up to 40 T is currently under construction.

Resistive magnets are water-cooled copper coils, that use two design principles. The outer part of the magnet is usually a so called Bitter magnet, realizing a coil by a stack

of copper disks. A particularity of the resistive magnets designed in Grenoble is that the inner part is a polyhelix magnet, that consists of concentric copper tubes that have been cut into helices. The spatial homogeneity of the magnetic field produced by resistive magnets of the GHMFL is of the order of 10^{-3}. Exact values can be found in [43]. The temporal stability of the magnetic field is of about 10^{-4}, basically caused by parasitic ac signals at the main power frequency and its higher harmonics. Another source of noise are mechanical vibrations mainly caused by the flow of cooling water. The typical power consumption of a resistive magnet at 30 T is around 20 MW.

The experimental conditions in resistive magnets were not suitable for Condon domain visualization experiments using Hall probes but for studies of nonlinear response with a pickup coil system and for the construction of the Condon domain phase diagram of silver the experimental requirements are less stringent so that the high field magnets of the GHMFL could be used.

2.1.3 Measurement control

The data acquisition and the operation of the measurement devices were controlled by a computer. The lock-in amplifier (Stanford Research SR830) and the Keithley (2000) multimeters were connected with a GPIB bus to the computer. The magnet power supply was controlled via the serial RS232 bus. Only the temperature between 1.3 K and 4.2 K had to be adjusted manually by a membrane pressure controller. The measurement programs and routines were built with LabView. With the graphical LabView compiler the measurement programs could be easily adapted to the various purposes of this work.

2.2 Ac susceptibility setup

A standard ac modulation method was used to measure the susceptibility and the higher harmonics of the beryllium and silver samples. This method was first introduced by Shoenberg and Stiles [44]. Comprehensive reviews can be found in [45, 46] as well as in [11]. Here, we will only outline the basic principles of the method.

The sample is placed in one of a balanced pair of pickup coils. The magnetization M is made to vary periodically with time with small amplitude at some suitable frequency ω and the induced voltage at the same frequency or at a higher harmonic $k\omega$ is measured. The periodic variation of M is obtained by superimposing a small periodic field $h_0 \cos \omega t$ on the applied field H_0. Figure 2.1 shows a schematic representation of the ac susceptibility setup. The great advantage of such modulation methods is that phase sensitive detection of the pickup voltage can be used which improves considerably the signal to noise ratio and therefore the effective sensitivity of detection.

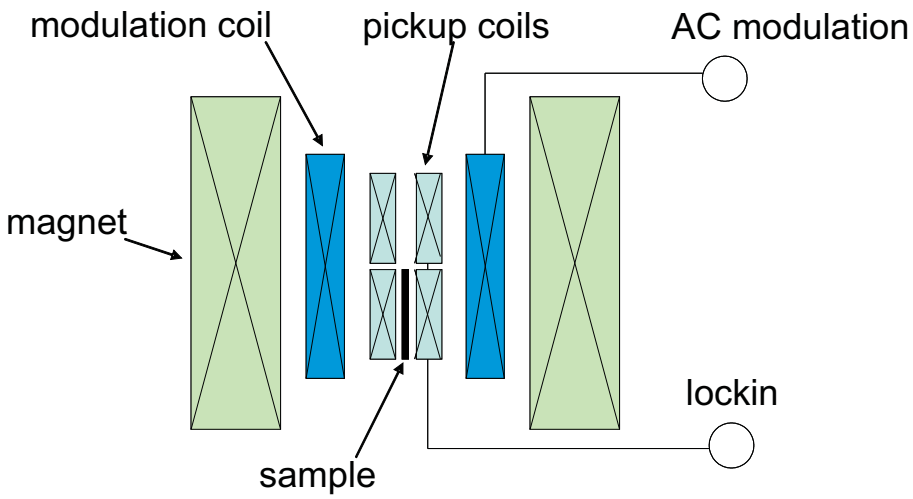

Figure 2.1: Schematic representation of the ac susceptibility setup. A small modulation field is superposed to the applied field from the superconducting coil. The sample is placed in one of a balanced pair of pickup coils. The induced voltage is measured with a lock-in amplifier.

The voltage induced in the pickup coil is given by

$$V_p = \alpha \frac{\mathrm{d}M}{\mathrm{d}H} \frac{\mathrm{d}H}{\mathrm{d}t} \tag{2.1}$$

where α is an appropriate coupling constant. $\mathrm{d}H/\mathrm{d}t$ is simply $-h_0\omega \sin \omega t$ but if h_0 is appreciable the time dependance of $\mathrm{d}M/\mathrm{d}H$ must be taken into account. Thus

$$V_p = -\alpha h_0 \omega \sin \omega t \left(\frac{\mathrm{d}M}{\mathrm{d}H} + \frac{\mathrm{d}^2 M}{\mathrm{d}H^2} h_0 \cos \omega t + \ldots \right) \tag{2.2}$$

where all derivatives are to be taken at $H = H_0$. Consequently if the variation of M with H is non-linear, V_p contains not only the fundamental frequency ω but also higher harmonics, i.e.

$$V_p = -\alpha\omega \left(h_0 \frac{\mathrm{d}M}{\mathrm{d}H} \sin \omega t + \frac{1}{2} h_0^2 \frac{\mathrm{d}^2 M}{\mathrm{d}H^2} \sin 2\omega t + \ldots \right). \tag{2.3}$$

Here only the lowest power of h_0 has been retained in the amplitude of each harmonic. If we now make the specific assumption that the dHvA magnetization M as function of H is given in the first harmonic approximation, i.e.

$$M = A \sin \left(\frac{2\pi F}{H} + \phi \right) \tag{2.4}$$

and we write the field interval of one dHvA oscillation as $\Delta H = H^2/F$ equation (2.3) becomes

$$V_p = -\alpha\omega A\left[\left(\frac{2\pi h_0}{\Delta H}\right)\sin\left(\frac{2\pi F}{H}+\phi-\frac{\pi}{2}\right)\sin\omega t + \frac{1}{2}\left(\frac{2\pi h_0}{\Delta H}\right)^2\sin\left(\frac{2\pi F}{H}+\phi-\pi\right)\sin 2\omega t+\ldots\right]. \tag{2.5}$$

We see that if $h_0 \ll \Delta H$, the harmonic amplitudes are small, each successive harmonic being weaker by a factor of order $(2\pi h_0/\Delta H)$.

Usually a phase-sensitive detector tuned to the fundamental frequency ω is used to detect the pickup voltage V_p. This improves the signal to noise ratio. On the other hand there are some considerable advantages in tuning the lock-in amplifier to a harmonic of ω. For example if the pickup coils are not perfectly balanced V_p contains a considerable component of $\sin\omega t$ not associated with properties of the sample. Furthermore, even at low modulation frequencies, eddy currents induced in the sample upset the balance of the pickup coils so that the measured dHvA oscillations appear on a sloping base line. Another source of noise are vibrations of the pickup coil in the steady field caused by the interaction of the modulating current with the applied field. These effects influence mostly V_p detected at the fundamental ω and can be almost completely eliminated by detection on 2ω or higher harmonics. But in order to get an appreciable amplitude of such a harmonic in equation (2.5), the modulation level must be increased in a way that the condition $(2\pi h_0/\Delta H) \ll 1$ is no longer valid.

For weak modulation h_0 the pickup voltage V_p has exactly the wave form of $\mathrm{d}M/\mathrm{d}H$ and higher harmonics corresponding to $\mathrm{d}^kM/\mathrm{d}H^k$ are too feeble to be useful. The criterion [11] for the modulation to be weak enough for V_p to give faithful reproduction of $\mathrm{d}M/\mathrm{d}H$ is

$$\frac{2\pi F h_0}{H_0^2} \equiv \frac{2\pi h_0}{\Delta H} < 0.28. \tag{2.6}$$

Here one should note that if the susceptibility is measured over a large range of applied magnetic field and if it is desired to keep a constant ratio of h_0 to ΔH it is necessary to vary the modulation current as H^2. By the way, during such measurements also the field ramp rate should be varied as H^2 so that the lock-in amplifier measures for each dHvA period an equal number of values.

We mentioned already that eddy currents induced in the sample by the modulating field may influence the detected pickup voltage. This problem has been discussed in detail in [47]. The modulation frequency is considered to be low enough and eddy currents can be neglected if the skin depth s, given by

$$s = \sqrt{\frac{2\rho}{\omega\mu}} \tag{2.7}$$

where ρ is the resistivity and μ the absolute magnetic permeability of the sample, is large compared with some relevant sample dimension a (e.g. sample radius or thickness) i.e. if

$$\frac{a}{s} \ll 1. \tag{2.8}$$

An estimation of the possible dHvA waveform distortion in percent p for a cylindrical sample due to eddy currents is given in [47] for low modulation frequencies and high values of the differential susceptibility $\chi = \mathrm{d}M/\mathrm{d}H$

$$\frac{a}{s} < (0.19\frac{p}{\chi^2})^{1/4}. \tag{2.9}$$

In practice this means that for $a \approx 0.5$ mm, the modulation frequency $f = \omega/2\pi$ must be below 100 Hz. For very pure metals with little magnetoresistance and for high values of χ, e.g. in the Condon domain phase, f should be even below 10 Hz.

The above considerations for the modulation amplitude h_0 and frequency f are important if the aim is to study the waveform and the absolute amplitude of the dHvA oscillations. For experiments aiming at the dHvA frequency spectrum the requirements are less stringent. By the way, it was proposed in [47] that if the modulation frequency is raised to make eddy currents appreciable, resistance oscillations of the sample, i.e. the Shubnikov-de Haas effect, can be observed with the same field modulation setup, originally designed to measure the dHvA effect. An advantage of this method is that no electrical contacts must be prepared on the sample.

The pickup coil design depends very much on whether sensitivity or reliable calibration is the main aim and also on the kind of sample that is used and on whether the sample orientation needs to be varied. Some typical arrangements are presented in [11]. Figure 2.2 shows our homebuild setup made of Araldite. The pickup coils consist of about 400 turns wound with 50 μm thick copper wire. The inner diameter of the pickup coil is about 2.4 mm. We preferred to wind the wire on a Araldite structure and not directly on the sample, which would have certainly increased the sensitivity, because we intended to use the setup for several samples of slightly different sizes. Moreover, the sensitivity of such a compensated system should be more than sufficient to measure the dHvA effect in beryllium [3]. An advantage of our setup is that the pickup coil system on the right side of figure 2.2 could be used without the modulation coil shown on the left side. For example, the pickup coil were fixed above the Hall probe setup and then *in situ* measurements of the local and overall susceptibility were possible using the built-in water-cooled modulation coil of the superconducting magnet.

In principle the field modulation method can give absolute values of M and χ if the coupling constant α in equation (2.3) is known. For our setup the coupling constant is given by

$$\alpha = -\mu_0 N A (1 - n) \tag{2.10}$$

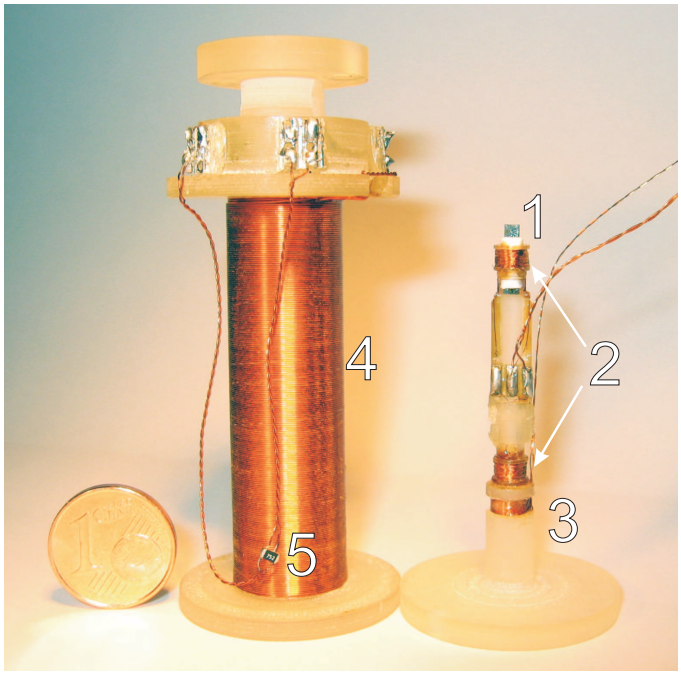

Figure 2.2: Ac susceptibility setup. The sample (1) is placed in one of a compensated pair of pickup coils (2). The amplitude h_0 of the modulation field is measured with a small probe coil (3). The modulation coil (4) consists of four layers wound with 200 μm thick copper wire. Both parts are made of Araldite. A thermometer (5) surveys possible heating of the setup. The right part is inserted to the modulation coil from the bottom.

where N is the number of turns, A the cross-sectional area of the sample and n the demagnetization factor of the sample. Thus in practice, due to e.g. the uncertainty of n because of a not perfectly ellipsoid-shaped sample, it would be difficult to achieve an accuracy of better than a few percent in the absolute determination of M or χ.

We tried to overcome this shortcoming of the calibration by preparing for each sample clones of exactly the same sizes made of lead. Lead has a critical temperature of 7.2 K and a critical field of 803 G [16]. At 4.2 K and zero applied field the lead clone is thus in the superconducting state and the pickup voltage measured with the field modulation method corresponds to $\chi = -1$. Then a small field of the order of 0.5 T is applied so that the lead sample is in entirely in the normal state. The resulting pickup voltage corresponds to $\chi = 0$. The field modulation setup can in principle be calibrated with these two values. In fact the calibration works best if the pickup coils are closely wound on the sample and the sample is much longer than the pickup coil.

The sensitivity of a typical field modulation setup is estimated in [11]. It turns out that the modulation method compares favorably with the widely-used torque method [48].

Moreover, in contrast to the torque method even materials with an isotropic Fermi surface or ferromagnetic materials can be studied with the field modulation method.

2.3 Hall probes

In this section we will first present the basic formulas of the Hall effect in three dimensions. The spatial resolution of a micro Hall probe in the diffusive regime is discussed. Then different sensor materials are compared and their possible application for Condon domain imaging is considered. Finally, the Hall probe setups which were used during this work are presented. They were all manufactured in the Technology Service Group of the Max-Planck-Institut für Festkörperforschung in Stuttgart.

2.3.1 Hall effect and resolution of a Hall probe

We consider a rectangular plate with small thickness d with a current I applied along the long side of the plate and a field B applied perpendicular to the plate. The Lorentz force acting on the charge carrier with charge q is compensated by the force on the carrier due to the Hall field E_y once a dynamic equilibrium has been established

$$qv_dB = qE_y \tag{2.11}$$

where v_d is the carrier drift velocity. Using the relationship for the current density $j = nqv_d$, where n is the charge density, the Hall constant R_H becomes

$$\frac{E_y}{jB} = R_H = \frac{1}{nq} \tag{2.12}$$

R_H is negative for electrons and positive for holes, and is expressed in $\Omega{\cdot}\mathrm{m}{\cdot}\mathrm{T}^{-1}$. By measuring R_H the type of the charge carriers and their density can be determined. Finally, the Hall voltage V_{Hall} is given by

$$V_{Hall} = R_H\frac{BI}{d}. \tag{2.13}$$

Often, especially when dealing with two dimensional electron systems, the Hall resistance R_{xy}

$$R_{xy} = \frac{V_{Hall}}{I} = R_H\frac{B}{d} \tag{2.14}$$

is calculated which should not be confused with the Hall constant R_H. For two dimensional electron gases (2DEG) the derivation of the Hall effect follows by analogy while the 3D charge density n is replaced by the layer or sheet density $n_s = nd$.

The main noise component of such Hall probes for $T < 100$ K up to a critical dc bias current I_{max} is the Johnson noise of the Hall voltage contacts

$$V_J = \sqrt{4k_B T R_v \Delta f} \tag{2.15}$$

where R_v is the two-terminal voltage probe resistance and Δf is the measurement bandwidth. Consequently for $I_{Hall} < I_{max}$ the signal to noise ratio (SNR) of a Hall probe is

$$SNR = \frac{R_H B I_{Hall}/d}{\sqrt{4k_B T R_v \Delta f}}. \tag{2.16}$$

For a Hall sensor with voltage leads of width w and total length l the two-terminal resistance R_v is given by

$$R_v = \rho \frac{l}{wd} = \frac{1}{nq\mu} \frac{l}{wd} \tag{2.17}$$

where ρ is the resistivity and μ the charge carrier mobility. Finally we obtain for the SNR

$$SNR = \left(\frac{\mu}{n}\right)^{1/2} \left(\frac{1}{4k_B T q \Delta f} \cdot \frac{w}{ld}\right)^{1/2} B I_{Hall}. \tag{2.18}$$

This means that if all other factors remain constant, the ratio of carrier mobility to carrier density provides a good figure of merit for the sensor. In practice, however, the maximum current bias imposes an equally severe constraint. If I_{max} is exceeded, the low frequency output becomes dominated by random telegraph-like $1/f$ noise, presumably due to the trapping and emission of "hot" electrons at deep donor impurities [49].

The Hall voltage is always superimposed on an "offset" voltage which arises due to slight misalignments of the opposing contacts. Another reason for the offset voltage are microscopic inhomogeneities in the conduction layer. For two very similar micro Hall probes the offset voltage is never the same. As the offset presents an ohmic longitudinal voltage drop it has the same strong temperature dependence as the carrier mobility. In practice this offset must be subtracted electronically every time that a new temperature is established.

2.3.2 Spatial resolution

If the length scales of inhomogeneities in the magnetic field are of the order of the dimensions of the Hall sensor it is important to provide a quantitative theory which relates the experimental data, in terms of resistance and voltage measurements, to the properties of the magnetic field, and more precisely to the size and strength of the inhomogeneities in this magnetic field. In other words it is necessary to determine the response function of the Hall probe.

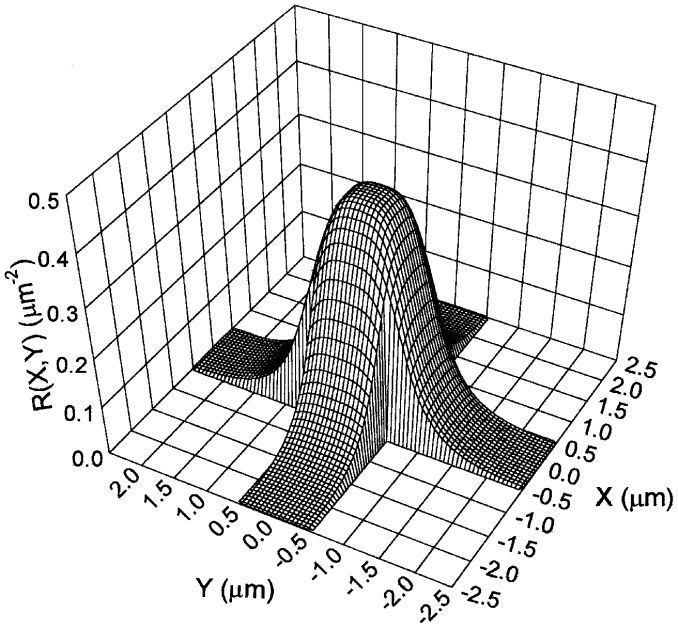

Figure 2.3: Response function for a two dimensional Hall probe with leads 1 μm wide as a function of the position of a highly localized vortex within it. From [49].

This problem can be studied in two limits. In the very high mobility and low temperature (below 4.2 K) limit the Hall probe is in the ballistic regime if the electron mean free path exceeds typical probe dimensions. In this limit the Hall voltage is well described by the average magnetic field in the Hall junction and it is rather insensitive to the exact position of the magnetic field inhomogeneity [50]. This is in contrast to the diffusive regime, where scattering processes strongly determine the electron transport. In this case there is no longer a simple relation between the Hall resistance and the magnetic field inhomogeneity. It turns out that different regions of the Hall probe are more or less sensitive to the presence of a magnetic field.

Figure 2.3 shows a 3D representation of the response function of a 1 μm wide Hall probe [49, 51]. We notice that the response extends well outside the square intersection of voltage and current leads. We note that the response function of a Hall probe can be determined experimentally by scanning a field source, for example a tip of magnetic force microscope, over the Hall probe of interest [52, 53]. The Hall voltage as function of the tip position measures directly the Hall response function. Figure 2.3 shows the response function for a Hall probe with symmetrical current and voltage leads. Recently the effect of the probe geometry on the Hall response function in an inhomogeneous magnetic field has been investigated theoretically [54, 55] and experimentally in [53]. It was found that narrowing the current or voltage leads, respectively, leads to more sensitive areas in the Hall junction. Especially the reduction of one of the voltage leads to submicron size, for

example by a focused ion beam, creates a highly sensitive spot in the junction and the spatial resolution of the Hall probe is appreciably increased. As lithographic fabrication techniques have limited resolution the effect of circular corners in the Hall junction has been studied in [55]. It was observed that circular corners decrease significantly the Hall response so that particular attention should be paid to the resolution with which the Hall probe structure is fabricated.

2.3.3 Hall probe materials

Miniature Hall probes have been used for many years to detect magnetic fields and field gradients on a micron scale. Typically thin evaporated films of the semimetal bismuth [56, 57] and later epitaxial films of InAs [56], InSb [56] and GaAs have been employed in this role. Although most of these studies present results on a much coarser scale, spatial resolution as high as 4 μm with magnetic field sensitivity of 0.01 mT was already attained in [57].

The development of modulation doped semiconductor heterostructures [58] revolutionized the field. These epitaxial structures contain two dimensional layers of electrons (2DEG) with carrier mobilities which are far higher than in any other compound (see also table 2.1). Hall probes made of 2DEG combine high sensitivity and high spatial resolution. Therefore, mostly Hall probes prepared of a 2DEG are nowadays employed as extremely sensitive flux detectors to study, for example, flux motion in type-II superconductors [59] and vortex dynamics in high-temperature superconductors [60, 61, 62].

Nevertheless, each type of Hall probe qualifies for a certain field and temperature range and has its own advantages like high sensitivity, linearity of the Hall signal in field, large signal to noise ratio, small size, reproducibility of the sensitivity after thermal cycling, ease of fabrication, and mechanical robustness. Figure 2.4 compares the Hall resistance R_{xy} as function of applied magnetic field at millikelvin temperatures for 0.1 μm thick polycrystalline bismuth on a sapphire substrate, 0.1 μm thick InAs on a GaAs substrate, and a GaAs 2DEG heterostructure. Bismuth Hall probes are easy to fabricate, but their Hall signal is nonlinear in field, saturating for high fields and their sensitivity is small. Furthermore, the Hall constant depends strongly on temperature and large changes in the sensitivity occur under thermal cycling. Group III-V semiconductors like InAs, InSb and GaAs are more suitable for the application as magnetic field sensors at liquid helium temperatures. The Hall coefficient of these compounds is larger than in bismuth by a factor of 750 for InSb and 75 for InAs for example. The signal to noise ratio is larger than in bismuth as well by a factor of 10 in InSb. Figure 2.4 shows that an enormous sensitivity can be reached with 2DEG GaAs Hall probes by reducing the charge carrier concentration and increasing the charge mobility (see also table 2.1). However, this increases not only the Hall resistance but causes also quantum Hall effect at low temperatures. This is unfavorable for a Hall probe since the sensitivity depends in this case

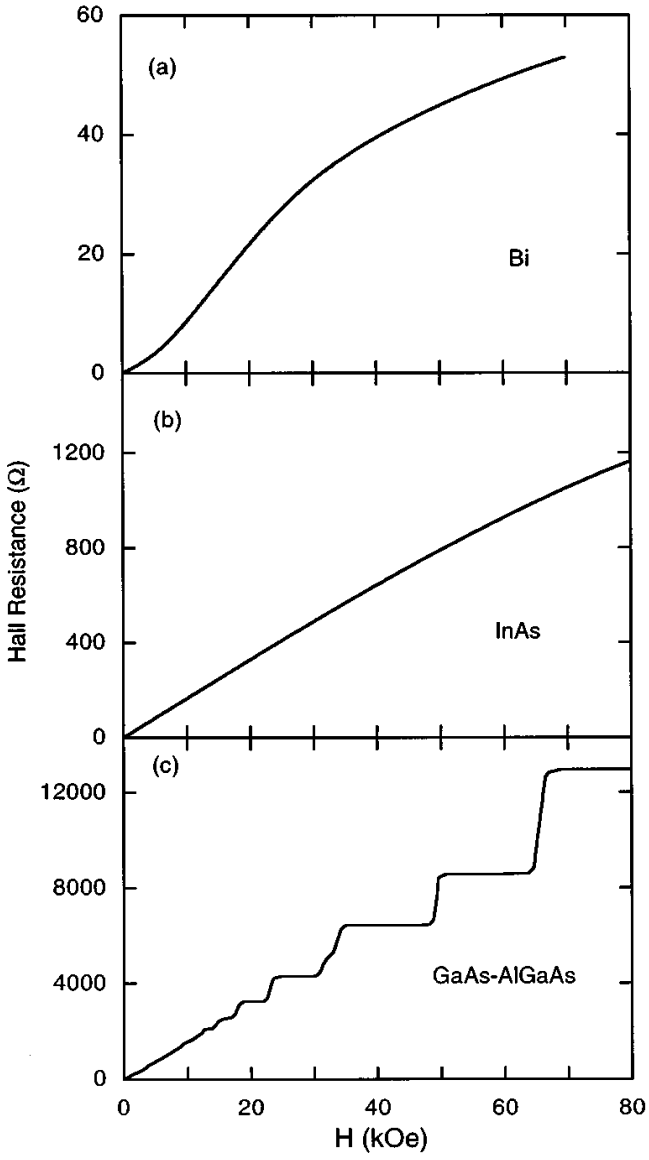

Figure 2.4: Comparison of the Hall resistance as a function of magnetic field H at $T = 0.3$ K for three magnetometer materials. Note the change of vertical scale between panels. From [63].

strongly on the applied magnetic field and is even zero at a quantum Hall plateau.

In conclusion, we see that for the purpose of Condon domain visualization, at low temperatures and high magnetic fields, epitaxial films made of InAs, InSb or GaAs are the most favorable materials for the fabrication of Hall probes.

2.3.4 $10 \times 10\ \mu m^2$ micro-Hall probes

The semiconductor layers for this Hall probe setup were prepared by K. Eberl from the Max-Planck-Institut für Festkörperforschung in Stuttgart. The same material was used for studies on quantum Hall effect in disordered layers with a continuous 3D single-particle spectrum of the charge carriers [64, 65]. The semiconductor structure was prepared with molecular beam epitaxy. On a GaAs(100) substrate were successively grown an undoped GaAs layer (0.1 μm), a periodic structure 30×GaAs/$Al_{1-x}Ga_xAs$(10/10 nm), an undoped GaAs layer (0.5 μm), the heavily Si-doped GaAs layer of 140 nm nominal thickness and a cap layer (0.5 μm). The mobility μ in the heavily doped layer was about 2600 cm^2/Vs at zero magnetic field and the bulk density of electrons n was 1.6×10^{17} cm^{-3} at 4.2 K. The Hall probe structure was made by optical lithography and wet etching at the Max-Planck-Institut für Festkörperforschung in Stuttgart. Contacts to the Hall probes were prepared by diffusion of a AuGe/Ni alloy into the conducting semiconductor layer at 450°C. Finally, a CrAu layer was evaporated to facilitate the attachment of bonding wires.

Figure 2.5 shows the Hall probe setup which was designed in [66]. Four independent Hall probes with an active surface of $10 \times 10\ \mu m^2$ are placed on one chip. The free surface on the chip available for a sample and for scanning is about 6×6 mm^2. The distance between the centers of the Hall probe is 200 μm. The whole structure is covered with a 3 μm thick varnish which remained after optical lithography processing. A particularity of this Hall probe setup is that there are four surface areas covered with CrAu. These surfaces were used for capacitive distance control during scanning experiments as they form a capacitor with the metallic sample.

Figure 2.6 shows the behavior of the two-terminal resistance R_V and the Hall voltage V_{Hall} as function of magnetic field up to 10 T at 4.2 K. R_V and V_{Hall} were measured with a standard ac lock-in technique at low frequencies (≈ 40 Hz). An ac current with about 5 μA amplitude was passed through the sample. This was about a thousand times higher than in [65] where self-heating was carefully avoided. For our purpose there were no disadvantages in applying higher currents but rather the signal to noise ratio improved appreciably. R_V in figure2.6a shows well-pronounced Shubnikov-de Haas oscillations [64]. As a voltage source (oscillator of the lock-in amplifier) was used to apply the current a high resistance (1 MΩ) was connected in series with the Hall probe to keep the current constant as function of magnetic field. Figure 2.6b shows slight deviations from linearity in the Hall voltage. These small deviations at 4.2 K might be due to quantum Hall effect

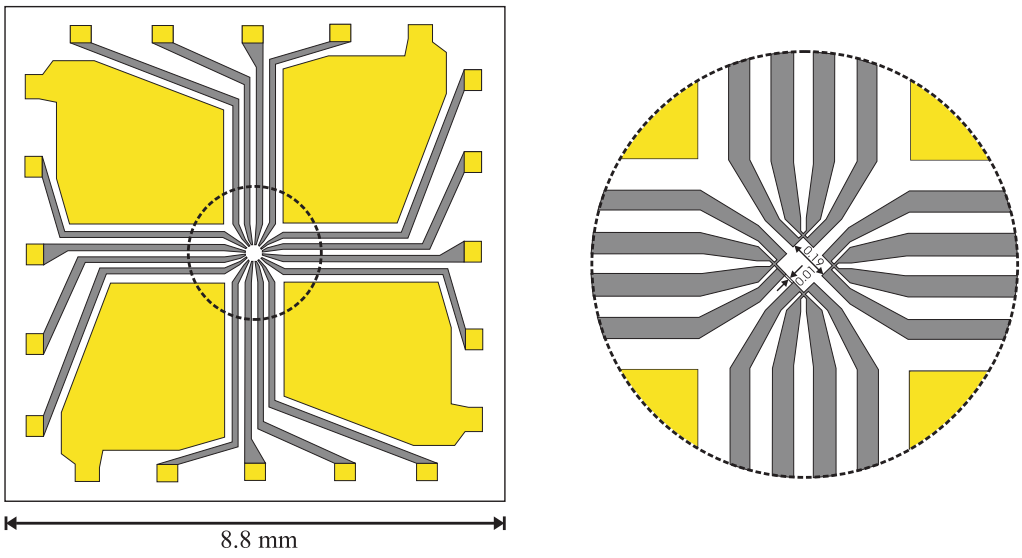

Figure 2.5: Hall probe setup with four Hall probes with an active surface of 10×10 μm^2. The distance between neighboring probes is about 200 μm. Four surface areas are covered with CrAu for capacitive distance control. The right side shows a zoom to the center of the Hall probes with leads for current and voltage being dark shaded.

like in [64] or on the other hand they might result of a slight misalignment of the opposing voltage probes which causes an ohmic longitudinal voltage drop with the strong magnetic field dependence of R_V.

From the slope of V_{Hall} in figure 2.6b we can estimate that for a magnetic resolution of 1 G a voltage difference of 1 μV must be resolved at an applied current of 5 μA. However, the typical resolution of a lock-in amplifier is $10^{-3}..10^{-4}$. In order to reach the magnetic resolution at an applied magnetic field of 10 T the offset Hall voltage must be therefore compensated. Figure 2.7 shows the circuit diagram used for the compensation. An simple ac bridge was built with a General Radio capacitance and resistance bridge and with a high impedance low noise preamplifier. On A the General Radio generated a sinusoidal voltage with variable amplitude and phase. On B the Hall voltage is preamplified with a gain of ten. A lock-in amplifier measured the differential signal $A - B$ between the Hall voltage and the reference signal from the bridge. The Hall voltage could be adjusted to zero for every magnetic field between 0 T and 10 T by changing the capacitance and resistance of the General Radio bridge.

The Hall probe setup had however some shortcomings. In dc measurements of the Hall voltage the noise level was very high so that the magnetic resolution was not sufficient. This might be due to the considerably high two-terminal resistance of about 200 kΩ. On the other hand the more complicated ac method with the above described compensation

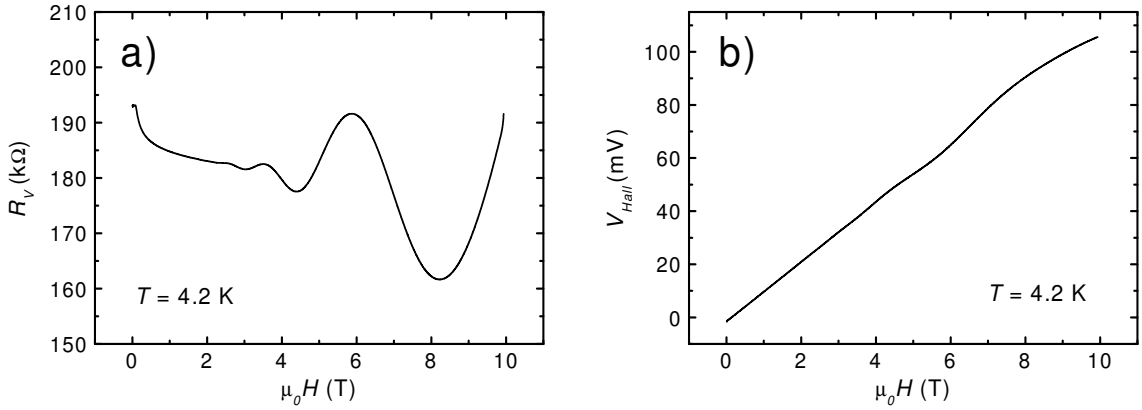

Figure 2.6: (a) R_V and (b) V_{Hall} as a function of magnetic field up to 10 T at 4.2 K. The two-terminal resistance shows well pronounced Shubnikov-de Haas oscillations. The transverse resistance is slightly nonlinear.

was difficult to apply to several Hall probes simultaneously. Furthermore, for scanning Hall probe application the integration time ($\approx$ 1 s) of the lock-in amplifier should be reduced by increasing the frequency of the driving current ($>$ 150 Hz). However, it turned out that for higher frequencies the phase of the lock-in amplifier could not be arranged in a way that a monotonous Hall voltage like in figure 2.6b was obtained.

2.3.5 5×5 μm^2 micro-Hall probes

A second Hall probe generation was developed later [66] presenting some advantages in design. However, the same semiconductor layer as described above was used for their realization. The overall surface of the setup was considerably reduced to 4×4 mm^2 because only small pieces of the GaAs heterostructure were left in Stuttgart.

Figure 2.7 shows the layout of the Hall probe setup. Two pairs of Hall probes, each with an active surface of 5×5 μm^2, are separated by 1.5 mm. The distance between two probes of a pair is about 20 μm. The structure size of 5 μm was actually the minimum size of the optical lithography facility in Stuttgart.

This design offers on the one hand the possibility to measure the applied magnetic field H_a with one Hall probe and the induction B with another one, if the sample is small and covers only one pair of the Hall probes. On the other hand a short range differential measurement can be made between nearby Hall probes, to detect spatial inhomogeneities in the magnetization of the sample. In this respect we note that the distance of about 20 μm between the nearby Hall probes was approximately the theoretically predicted size of the Condon domain structure [4].

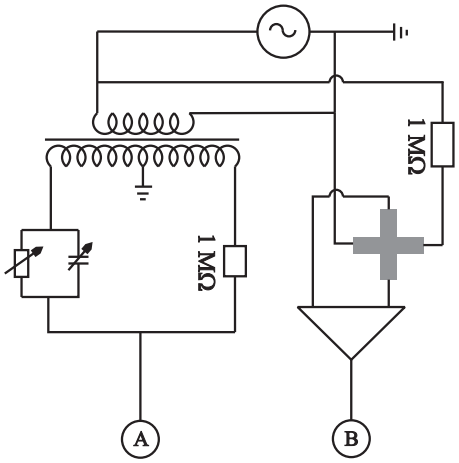

Figure 2.7: Circuit diagram used to balance the Hall voltage offset. A gives a reference voltage generated by a General Radio capacitance bridge. B gives the Hall voltage amplified with a low noise differential preamplifier. A and B are linked to the lock-in amplifier.

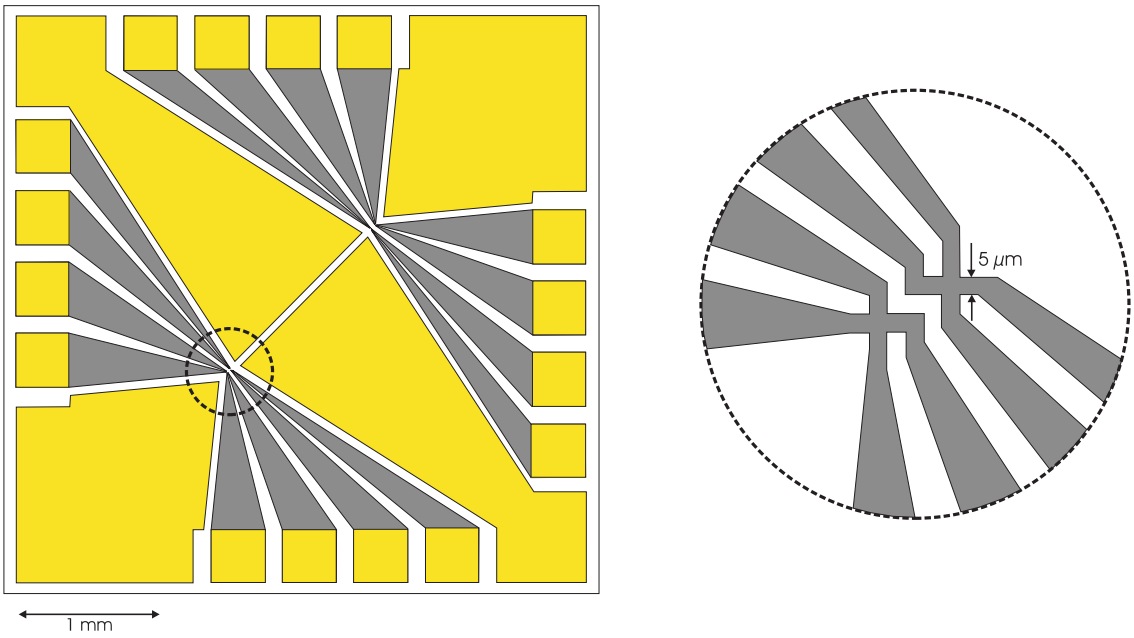

Figure 2.7: Hall probe setup with two pairs of Hall probes with an active surface of $5 \times 5\ \mu\text{m}^2$. The distance between the two pairs is 1.5 mm and between the probes of a pair is about 20 μm. The surface areas covered with CrAu are used for capacitive distance control. On the right side an extended view of two Hall probes is shown with the leads for current and voltage being dark shaded.

Sample ID	carrier concentration n at 4.2 K (1/cm^3 or 1/cm^2)	mobility μ at 4.2 K (cm^2/Vs)
71959	$4.3{\cdot}10^{16}$	1850
71960	$3.5{\cdot}10^{15}$	1270
71961	$2.9{\cdot}10^{18}$	1880
81504	$1.3{\cdot}10^{4}$	1440000

Table 2.1: Carrier concentrations and mobility of the GaAs heterostructures used for the fabrication of the Hall probe arrays. 81504 is a heterostructure with a 2DEG.

However, similar problems like discussed above for the previous Hall probe setup persisted for this setup because the same semiconductor material was used for its fabrication.

2.3.6 Hall probe arrays

A completely new Hall probe generation was finally developed to overcome the raised shortcomings. It was shown in equation 2.18 that the ratio of carrier mobility to carrier density provides a good figure of merit for the Hall probe. Table 2.1 shows the carrier concentrations and the mobilities of the semiconductor heterostructures that were selected in this purpose and were received from the molecular beam epitaxy group in Stuttgart. Heterostructure 81504 is a 2DEG. The other heterostructures consist of a 1 μm thick Si-doped GaAs layer sandwiched between two 10 nm thick undoped GaAs layers grown on a GaAs(100) substrate. It was noticed that the maximal current bias I_{max} imposes an equally severe constraint. Therefore, we used heterostructures with much thicker conducting layers (1 μm instead of 140 nm) in order to increase I_{max}. The Hall probe setup that was first received was made of layer 71959. With this setup all measurements presented in chapter 3 are made.

Figure 2.8 shows the design of the Hall probe setup. Two arrays of five Hall probes are placed at a distance of $b = 1$ mm. Each Hall probe has an active area of $10{\times}10$ μm^2. The distance between the centers of adjacent Hall probes in an array is 40 μm. The second array is rotated by 90° with respect to the first. We note that the design advantages of the Hall probe setup in figure 2.7 have been retained. Differential measurements between the applied magnetic field and the induction are possible. Moreover, the possibility to observe spatial inhomogeneities of the magnetization has been extended from two Hall probes to an array of five Hall probes. Finally, the second array was rotated by 90° with respect to the first to be able to measure magnetization profiles along and across an axis of symmetry of the sample.

Due to the rather thick conducting layer of the heterostructure high dc currents, usually 100 μA, could be applied in series to all five Hall probes of an array. Figure 2.9a shows

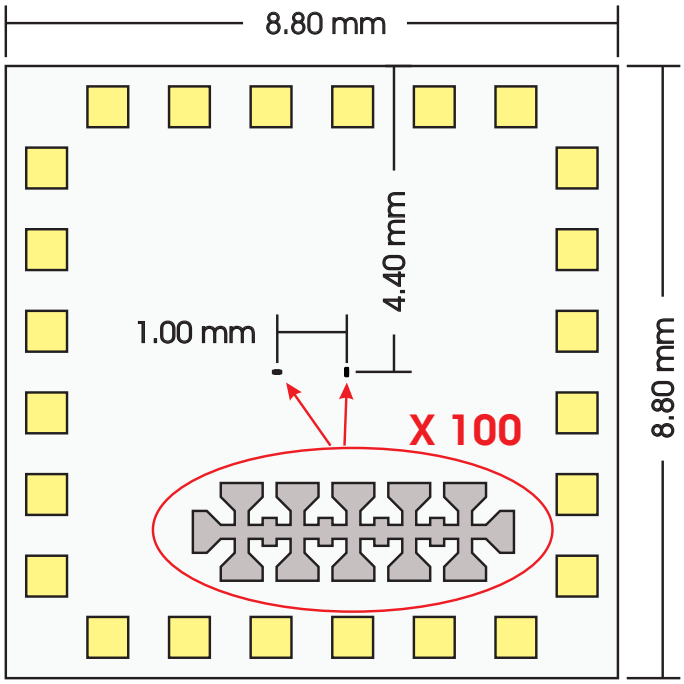

Figure 2.8: Hall probe setup with two arrays of Hall probes with an active surface of 10×10 μm^2 separated by $b = 1$ mm.

the two-terminal resistance of a Hall probe as function of magnetic field at 4.2 K. Well-pronounced Shubnikov-de Haas oscillations are observed and the resistance increases strongly for magnetic fields exceeding 6 T (insulator transition). Here, we used a stabilized dc current source to apply the Hall current. Therefore, the Hall current was constant even though the two-terminal resistance exhibits strong magnetoresistance and rises steeply at 6 T. Figure 2.9b shows the Hall resistances for three Hall probes of an array at 1.3 K. R_{xy} is in good approximation linear up to 10 T without deviation due to the quantum Hall effect. The Hall voltages were measured simultaneously with Keithley multimeters. A magnetic resolution of better than 1 G is reached with the Hall probes at magnetic fields up to 10 T. Furthermore, all five Hall probes of an array had very similar Hall resistances. The slight offsets are subtracted numerically.

2.4 Test of the spatial resolution of the Hall probes

Before we tried to visualize Condon domain structures which requires quite complicated measurement conditions (1.3 K and high offset magnetic fields) we tested the spatial resolution of the Hall probe setup. For this we needed a magnetic structure which has

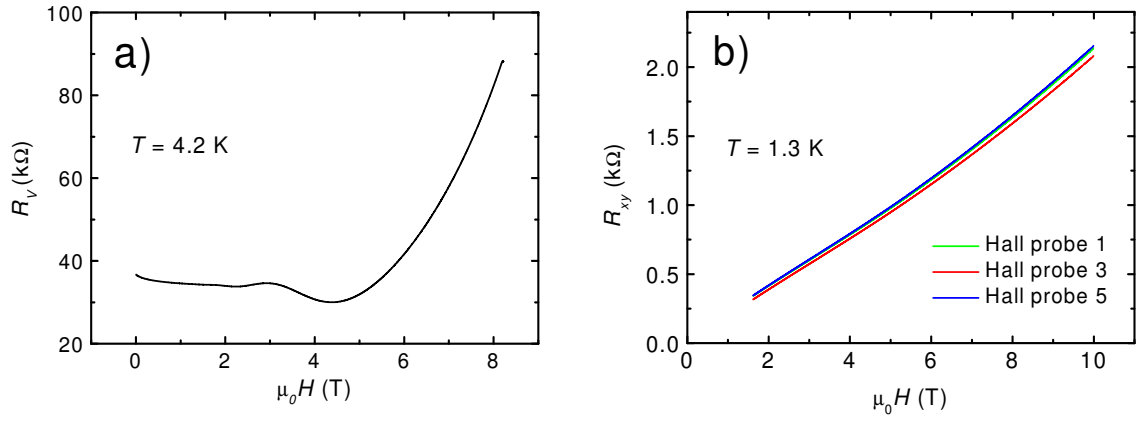

Figure 2.9: (a) Two terminal resistance R_V at 4.2 K and (b) Hall resistance R_{xy} for three Hall probes at 1.3 K as a function of magnetic field.

sizes comparable to the predicted Condon domain structure.

Actually, the well known [67, 68, 69] intermediate state domains in type 1 superconductors are very similar to Condon domain structures and the typical sizes can be made comparable to the expected Condon domain structures. In samples with nonzero demagnetization factor n the diamagnetism of the superconducting state distorts the applied field, producing a nonuniform field distribution. As a result superconducting and normal domains coexist in the intermediate state for applied fields H_a within the range

$$H_c(1-n) < H_a < H_c \tag{2.19}$$

where H_c is the critical field. In the frame of an unbranched laminar model [68] the period of the domain structure p can be estimated

$$p = \sqrt{t\frac{\delta}{\phi}}. \tag{2.20}$$

where t is the thickness of the sample, δ the surface energy parameter which corresponds roughly to the coherence length and ϕ a function tabulated by Lifshitz and Sharvin [70]. Here one should note the striking similarity between both formulas (2.20) and (1.45) for the respective domain periods of Condon domains and intermediate state domains. The main difference is that the coherence length δ is replaced by the domain wall thickness w in the formula for the Condon domain structure. This illustrates that the Condon domain state can be considered as physically similar to the intermediate state.

We decided to test the spatial resolution of the Hall probes by measuring intermediate state domains on a polycrystalline sample of tin. For tin intermediate state domains have

been extensively studied in the past [68, 71] with e.g. the powder decoration technique, the magneto-optic method and with field probes using the extreme magnetoresistance of bismuth. More recently the intermediate state of tin was studied by μSR [72]. Their sizes and topology is hence well known. In fact, intermediate state domains are very suitable to test the spatial resolution of the Hall probes for the possible observation of Condon domains. First, the temperature ranges are nearly the same (less than 3.7 K for tin) and secondly the sizes of both domain structures can be made quite similar. On the other hand the applied magnetic field is very low for the intermediate state and the magnetic contrast $(B_1 - B_2)/B_1$, where B_1 is the induction in the normal state domain and B_2 the induction in the superconducting domain, is 1 for intermediate state domains whereas for Condon domains the magnetic contrast is not more than 10^{-3}.

A plate-like sample of polycrystalline tin was prepared with a thickness of about 1 mm. The demagnetization factor of the sample was determined [73] to be roughly $n = 0.5$. The critical temperature T_c of tin is 3.72 K [74]. The critical field $\mu_0 H_{c0}$ at zero temperature is 305 ± 2 G [75]. According to equation (2.20) one could expect domain structures in the tin sample ($\delta \approx 10^{-4}$ cm) with p of the order of $20 - 80$ μm. We have chosen a base temperature of 2.7 K which reduces the critical field according the formula

$$H_c = H_{c0}\left(1 - \left(\frac{T}{T_c}\right)^2\right) \tag{2.21}$$

to $\mu_0 H_c = 140$ G. The sample was directly fixed on the 5×5 μm^2 Hall probe setup presented in section 2.3.5 and slightly pressed by a cotton pad to ensure a small distance between the Hall probes and the sample.

Figure 2.10 shows the induction B measured at the surface of the tin sample when the applied field is slowly swept. One can clearly distinguish three regions. First the superconducting region $0 < H_a < H_c(1 - n)$ between $0 < \mu_0 H_a < 80$ G where the measured induction is approximately zero. The very small slope in this field range might be due to the fact that there is a finite distance between the Hall probes and the sample. In the second region $H_c(1 - n) < H_a < H_c$ the sample is in the intermediate state. Finally, for applied fields higher than H_c the sample is in the normal state.

In the intermediate state fast variations of the measured induction are observed. They are caused by the normal and superconducting domains which are moving across the Hall probe setup. These variations appear only when the applied field is swept very slowly with about 0.1 G/s. Here we used the resistive modulation coil to sweep the field because the smallest sweep rate ($\approx$ 1 G/s) of the power supply of the superconducting magnet was still to high to resolve the fast induction variations. Figure 2.11 shows a zoom to the intermediate state. One can see a steep rise of the induction around $\mu_0 H_a = 85$ G followed by a drop at $\mu_0 H_a = 87$ G. This means that a normal state domain is passing across the Hall probes and then a superconducting domain follows. The induction was

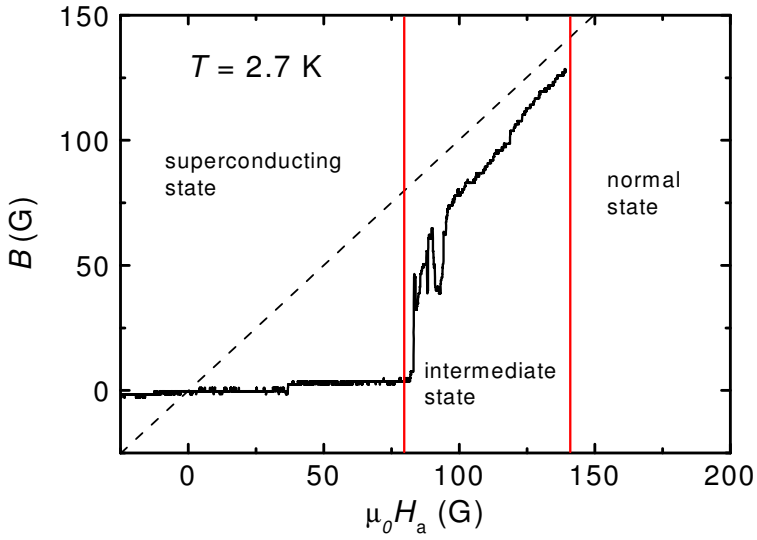

Figure 2.10: $B(H_a)$ measured with a Hall probe on a tin sample. The vertical lines separate roughly the field ranges of the three different states. The dashed line is a guide to the eye of unity slope $B = \mu_0 H_a$. In the intermediate state fast variations of the measured induction due to domains are visible.

simultaneously measured with two close (20 μm distance) Hall probes. For some applied fields exactly the same inductions are measured whereas there are also field regions where the induction clearly differs. This implies that a domain boundary is situated between the close Hall crosses.

In conclusion, we could clearly observe normal and superconducting domains of the intermediate state without moving the sample and the Hall probe setup with respect to each other. The sample sizes were arranged in a way that the typical domain period in tin is similar to the expected periods in beryllium at 4 T and silver at 10 T. The maximum amplitude of the steps was about 20 G whereas one would expect about 100 G. This means that we observe about $1/5$ of the real magnetization difference. The resolution of the Hall probes would therefore be sufficient to detect Condon domains in beryllium where a magnetization difference of 30 G [5, 29] between dia- and paramagnetic domains is expected.

2.5 Insert

In order to determine the geometry and the size of the Condon domain structure we need to measure the magnetization distribution at the surface of the sample using a Hall probe.

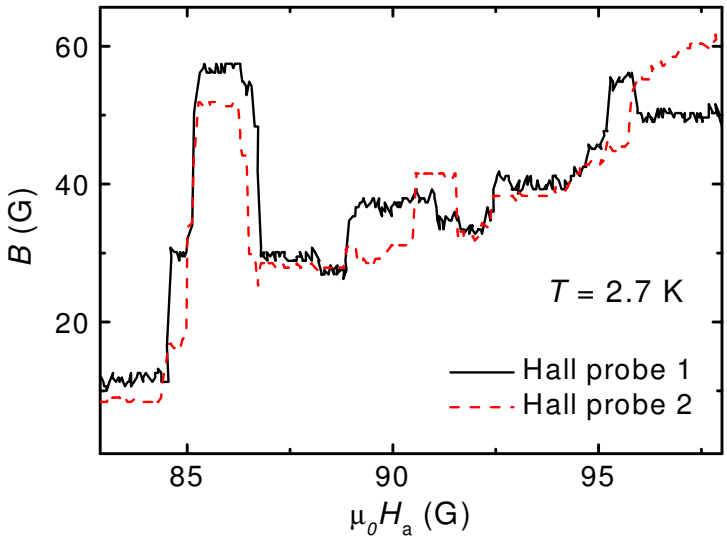

Figure 2.11: Zoom to a typical intermediate state region. The induction B is simultaneously measured with two close 5×5 μm^2 Hall probes (see section 2.3.5). The applied field was swept with a very low sweep rate of 0.1 G/s with the resistive modulation coil.

On the one hand we can use an array of Hall probes to detect the magnetization at some discrete points on the surface (see chapter 3) or on the other hand we can move the Hall probe with respect to the sample surface. Here, we present the mechanically driven scanner unit which was built for this purpose.

In chapter 1 theoretical estimations for the Condon domain size were given. If we assume a domain size of 30 μm [4] the scanning range of the Hall probe should be at least 100 μm in the x- and y-direction so that several domains could be resolved. Moreover, the spatial resolution of the motion on the surface should be of a few μm. Since the inhomogeneous magnetization distribution falls off outside the sample in a distance that corresponds to the domain size the distance sample-Hall probe should be as small as possible and must not exceed 10 μm. On the other hand, especially the hard beryllium samples will damage the Hall probes if the contact is too close. Furthermore, the scanning device needs to fit in the small tail of the ^{4}helium cryostat (diameter of 38 mm), should be leak-tight so that the cryostat can be pumped to 1.3 K and finally, should work reliably in high magnetic fields up to 17 T.

A considerable number of scanning probe techniques have been developed in recent years [76]. Common to all is the need for a positioning or a scanning movement of the probe tool with respect to the sample. For high resolution techniques like scanning tunneling microscopy [77] mechanical scanners incorporating piezoelectric actuators are the

appropriate choice. For large range scanning probe techniques, piezoelectric actuators are not favorable (see [78] and references therein). To access mm ranges, either their dimensions are inconveniently large, their deformation has to be amplified by lever systems or they have to be combined with multimorph elements [79]. In addition problems like creep, hysteresis and nonlinearity become more and more important the larger the excursion of the actuators is.

In order to avoid these problems mechanically driven scanners can be employed [57, 78, 80]. They offer easy construction, ease of operation (they can even be operated manually) and stable positioning while inactive. Among the disadvantages are of course vibrations during scanning operation and the necessity of a mechanical access to the experimental region.

Mechanical scanning unit

We used a mechanically driven scanner developed by Heil *et al.* [78] and built by Lehmann [66]. Figure (2.12) shows a schematic representation of the mechanical scanner. The positioning unit has an accessible range in three dimensions of approximately 2 mm with a resolution and reproducibility in the μm range. The key element of this construction is a three-dimensional parallelogram composed of five leaf springs and a wire cross. Three brass screws (M3$\times$350 μm) are associated to the motion in the x-, y-, and z-direction. The screw motion is transformed via a bronze wire of 0.6 mm diameter and a lever into a bending of the leaf springs. The screws work against restoring forces so that all mechanical play is suppressed. The upper end of these screws are attached to stainless steel tubes that lead through squeezable O-seals out of the cryostat. They can be controlled manually or be coupled to stepper motors. Due to the symmetry of the design (apart from the z-motion) the movements of the support in the x- and y-directions are orthogonal and decoupled from each other for small displacements. In [78] the scanning device was tested and calibrated resulting a sensitivity of 0.8 μm/step in x- and y-direction using a stepper motor with 1000 steps per revolution, a deviation from linearity of smaller than 10% per full range, and a reproducibility of positioning of smaller than 2 μm. The sensitivity in the z-direction was estimated from the pitch of the screw of 0.35 mm to be approximately 0.35 μm/step.

Implementation

In usual scanning Hall probe microscopes (see [49]), the active Hall sensor is patterned close to a corner of a deep mesa etch which is coated with gold to act as an integrated tunnel tip. A relative tilt angle between the sample and the sensor ensures that the tip is the closest point to the sample surface. The sample is first approached until tunneling is es-

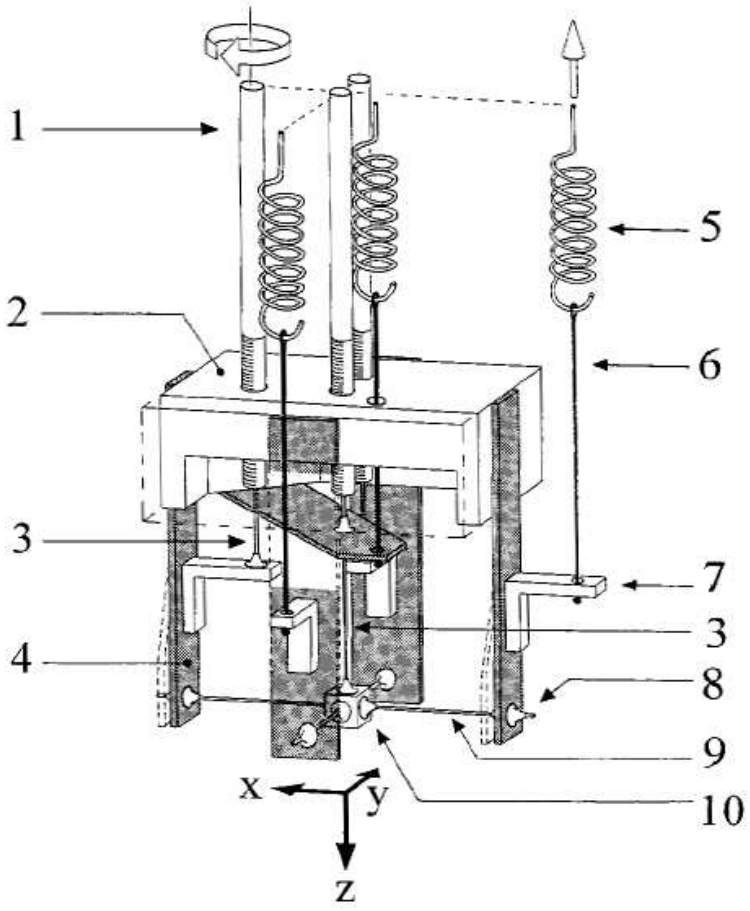

Figure 2.12: Schematic representation of the mechanical scanner from [78]. The rotation of the brass screw (1) is transformed via a lever system (3) into a bending of a bronze leaf spring (4) so that the sample holder (10) changes its position in x-direction. Restoring forces are provided by helical springs (5) to eliminate mechanical play.

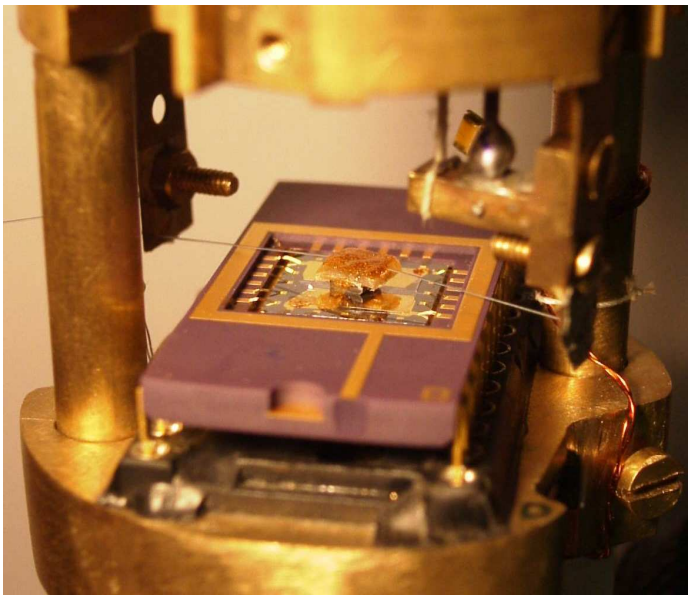

Figure 2.13: Setup with fixed Hall probes located in the chip carrier and a moving beryllium sample being glued on a copper wire. The setup allowed scans along one direction.

tablished, and then the Hall probe is scanned across the surface to measure simultaneously the magnetic field and surface topography.

The Hall probes of our setups were always more or less in the middle of the GaAs layer. Therefore, the above sketched technique was not practicable. In the following we show some scanning implementations realized with the mechanical scanning unit [78] and the existing Hall probe setups. For simplicity we decided to keep the relatively big chip carrier ($\approx$31 mm long and 15 mm large) containing the Hall probes fixed and to move the beryllium sample with respect to the sensors.

Figure 2.13 shows a setup allowing scans along one direction. The wire cross (9) and the probe support (10) in figure (2.12) were replaced by a 200 μm thick copper wire on which the sample was directly glued. To protect the Hall sensors and to reduce the friction, a thin mica flake was placed between the beryllium sample and the Hall probe. The copper wire provided a small restoring force in z-direction ensuring a close contact to the Hall sensors. However, a persistent problem was the poor positioning reproducibility and the high electronic noise during the sample motion due to the remaining friction at the interface sample-Hall probe.

A contact-less scanning method was developed to reduce the high mechanical noise. The beryllium sample was glued on the insulating support (10) in figure 2.12. The scanning unit offered the possibility of motion in the z-direction to adjust the distance sample-Hall probe from outside the cryostat. The areas coated with gold of the Hall setup in fig-

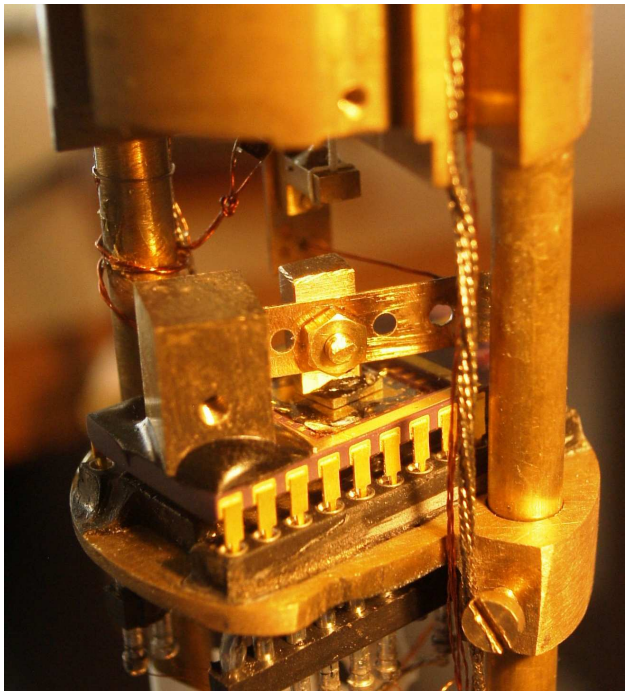

Figure 2.14: Setup resembling a record player. A brass lever is glued directly on the Hall probe carrier. The lever is driven by one leaf spring (4) of the scanning unit.

ure (2.5) were used for capacitive distance control. In fact, the capacity between the gold areas and the metallic sample was measured with a capacitance bridge. Unfortunately, the movements of the support (10) in the x-, y- and z-directions were not sufficiently decoupled. Especially for large excursions, the x-movement, for example, led to a slight rotation of the support (10) around the y-direction. As a result the big sample tilted a little with respect to the Hall probe setup.

To overcome the complicated problem of distance adjustment, we constructed a simpler setup with fixed distance sample-Hall probe. In order to minimize length changes during cool down the construction was made as small as possible and materials with similar thermal expansion were used. Figure (2.14) shows the design. A lever resembling a record player is directly glued on the chip carrier containing the Hall probes. The lever, on which the sample is fixed, is bent for scanning by one leaf spring (4) of the scanning unit which is connected to the lever by a copper wire. All components are made of brass and copper-beryllium and the construction is smaller than 1 cm^3.

In conclusion many technical problems have to be overcome to realize a reliable scanning motion of the sample especially with the requirements described above. While it was not clear whether Condon domains emerge to the sample surface we prefer to start the observation of Condon domains in the next chapter with a more simple static method

using an array of Hall probes.

2.6 Samples

In this section the sample preparation is described. Moreover, the Dingle temperature, which is an important parameter for the analysis of dHvA oscillations, will be determined for the beryllium and silver samples.

Beryllium

The beryllium single crystals were received from V.S. Egorov from the Russian Research Institute "Kurchatov Institute", Moscow. The samples were cut by electric spark erosion from the same single crystal on which Condon domain formation was observed using μSR [5, 28, 29]. The residual resistance ratio of the samples was $R_{300\mathrm{K}}/R_{4.2\mathrm{K}} \approx 300$. After cutting no further treatment was made to remove deposits and damages of the spark erosion. Especially chemical etching turned out to be difficult on beryllium as the etching rates were highly anisotropic in the hexagonal lattice. For domain observation experiments with Hall probes we polished slightly one side of the sample with the method described below to achieve a flat and mirror-like surface.

An important measure of the crystalline quality of the sample is the Dingle temperature T_D [19]. In the following we will show briefly how T_D is obtained from dHvA measurements [11].

The field dependence of the pth harmonic of the dHvA oscillations should be given by

$$M_p = C_p T H^{-n} R_D \frac{1}{\sinh\left(\alpha m^* p T/H\right)} \tag{2.22}$$

where R_D is the Dingle reduction factor introduced in equation (1.19). The values of C_p and n depend on the particular method of measurement. For instance, if it is M that is measured, it can be seen from (1.23) that $n = 1/2$, while if it is $\mathrm{d}M/\mathrm{d}H$, as in the ac modulation method for weak modulation, then $n = 5/2$.

The usual procedure to determine T_D from the field dependence of M_p (which need not to be measured absolutely) is to make a "Dingle plot". This is a plot of

$$\ln\left(M_p H^n \sinh\left(\frac{\alpha m^* p T}{H}\right)\right) \tag{2.23}$$

against $1/H$, which should be linear if equation (1.19) is valid. The slope of the plot gives immediately $\alpha p m^* T_D$. A variant of the procedure, valid if $\alpha p m^* T/H$ is large enough for

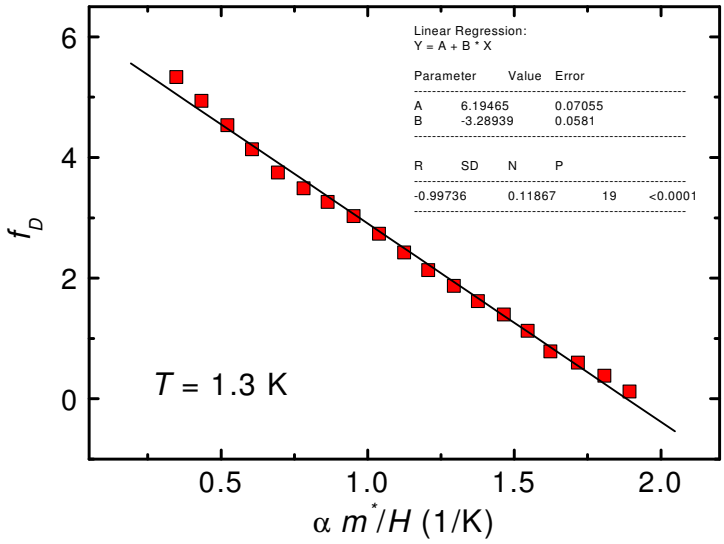

Figure 2.15: Dingle plot for the beryllium sample measured at 1.3 K. The slope is 3.3 K which results Dingle temperature $T_D = 2.0$ K.

sinh to be replaced by $\frac{1}{2}\exp$, is to plot simply $f_D = \ln\left(M_p H^n\right)$ against $\alpha m^* p/H$ and the slope then gives $T_D + T$.

Figure 2.15 shows a Dingle plot measured on a rod-like beryllium sample of sizes $8 \times 2 \times 1$ mm^3 with the long side being parallel to the $[0001]$-axis of the crystal. Here, the fundamental ($p = 1$) of the dHvA magnetization was directly measured with a Hall probe. In section 1.7 we have seen that two dHvA frequencies coexist in this orientation leading to a beat in the dHvA magnetization (see figure 1.14). For the determination of the Dingle temperature in figure 2.15 the dHvA amplitude at the beat antinodes was used. From the slope of the Dingle plot we obtain $T_D = 2.0$ K. The Dingle temperature can be assumed to be roughly the same for all samples cut from the same single crystal. In this respect we note that J. Hinderer [81] determined similar Dingle temperatures for the samples using the torque method [48].

Silver

The high quality silver single crystals were received from V.A. Gasparov from the Institute of Solid State Physics in Chernogolovka. The crystals were prepared in the same way as in experiments on radio frequency size effect and time of flight effect (see [82, 83] and references therein).

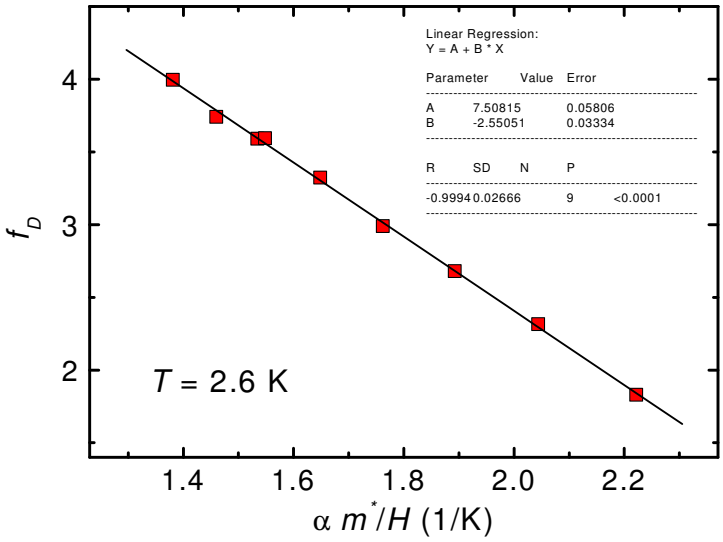

Figure 2.16: Dingle plot for the silver sample used in chapter 3 measured at 2.6 K. The slope is 2.6 K which results a Dingle temperature $T_D = 0$ K.

Plane-parallel silver plates of about 1 mm thickness were cut from a single crystal which had an initial residual resistance ratio of $R_{300\mathrm{K}}/R_{4.2\mathrm{K}} \approx 7000$. The largest surface of the samples was perpendicular to the $[100]$-axis of the crystal. After a subsequent oxygen (10^{-2} Pa) annealing at 750°C during 10 hours, the residual resistance ratio increased to 16000. The resistance ratio was measured by the contact-less Zernov-Sharvin method [84] which consists of measuring the torque on a sample caused by a rotating magnetic field. Finally, to obtain a flat and mirror-like surface, necessary for the Hall probe measurements, the samples were slightly repolished with the method described below.

The very high quality of the samples results in a very low Dingle temperature[1]. Figure 2.16 shows a Dingle plot for the sample ($2.4 \times 1.6 \times 1.0$ mm^3) on which Condon domains are directly observed in the next chapter. The fundamental of the dHvA magnetization was directly measured with a Hall probe. From the slope we obtain a Dingle temperature of $T_D = 0$ K. Considering all measurement errors we conclude that the Dingle temperature of the sample is certainly not bigger than $T_D = 0.2$ K.

[1] One should note that a high residual resistance ratio of the sample does not necessarily yield a low Dingle temperature as the scattering mechanisms of electrical conductivity and the dHvA effect are different [11].

Polishing

Usually chemical polishing is used to achieve a flat mirror-like surface of high quality single crystals [82]. Here, however, we carefully repolished the samples using abrasive polishing with small grit diamond paste. The sample was embedded at one end of a cylinder made of cold mounting resin (acrylic). The sample holder was then slightly pressed to the polishing disk which was covered with a cloth. The type of cloth used is important to the final result and we have been most successful with the Mecaprex polishing disks HS Lavande and TFR. Diamond paste with different grit sizes, first 1 μm and later for the finishing 0.1 μm, was dispersed on the cloth surface and diluted with distilled water. The silver removal rate was controlled with the rotation speed of the polishing disk and the weight put on the sample holder. After polishing the cylindrical sample holder made of acrylic was removed with a solvent and the sample was washed in acetone.

Chapter 3

Direct observation of Condon domains with Hall probes

Dans ce chapitre, on présentera les expériences de visualisation des structures magnétiques des domaines de Condon dans des échantillons d'argent. L'induction (ou l'aimantation locale) est mesurée avec des microsondes de Hall, un dispositif contenant deux séries de cinq sondes. Les sondes mesurent périodiquement une différence locale d'aimantation dans la partie paramagnétique des oscillations dHvA. Cette différence est attribuée aux domaines de Condon. Du comportement d'une série de sondes, on va déduire la direction de propagation des parois des domaines et de leur orientation. Ces mêmes expériences ont été réalisées sur un échantillon en béryllium, et d'après les résultats obtenus avec la rotation de spin des muons (μSR) sur cet échantillon de béryllium, on s'attendait à des différences d'aimantation plus importantes à la surface, ce qui n'a pas été vérifié expérimentalement.

3.1 Introduction

We have seen in chapter 1 that a phase with Condon domains appears periodically in normally nonmagnetic metals in strong magnetic fields at low temperatures under the condition $\chi_B = \mu_0 \partial M/\partial B > 1$. In a plate-like sample, oriented perpendicular to **H**, domains are formed with alternating regions of diamagnetic ($M < 0$) and paramagnetic ($M > 0$) magnetization in the paramagnetic part ($\partial M/\partial H > 0$) of the dHvA period [3]. The volume fraction of the domains varies with H so that $\overline{B} = \mu_0 H$ is fulfilled as an average over the sample [4, 29].

Condon and Walstedt [4] discovered these domains on a silver single crystal by a periodic splitting of the NMR line, corresponding to a local magnetic induction difference of about 12 G between the paramagnetic and diamagnetic regions in magnetic fields of about 9 T. More recently, Condon domains were observed in beryllium, white tin, aluminum, lead, and indium [5, 6, 13, 28, 29, 30, 31] by muon spin rotation (μSR). After all, Condon domain formation is expected to be a general phenomenon occurring in pure single crystals of all metals. Moreover, thermodynamic aspects of the Condon domain phase transition have been treated theoretically [12] and the state of the art in this field has been recently reviewed [9]. Some important questions, however, concerning domain size and topology, domain wall energy, and pinning properties can only be solved with a detailed knowledge of the domain structure. For this purpose, however, the local induction or magnetization must be measured with spatial resolution which is hardly possible with the above cited methods using NMR and μSR.

The state with Condon domains can be considered as physically similar to the intermediate state of type-I superconductors, where superconducting and normal regions form in an applied magnetic field. Therefore, domain structures resulting of such different phenomena as superconductivity and dHvA effect may be rather similar. Unfortunately, the magnetic contrast which is the ratio of the induction difference between both sorts of domains δB to the average induction is not more than 0.01 $\%$ for Condon domains (compared to 100$\%$ for intermediate state domains). Besides, the applied magnetic field itself is here hundred times higher. Thus, methods like magnetic decoration or magneto-optical detection used for intermediate state imaging [49, 68] can not be used for Condon domains.

In this chapter we present the first experimental results for a direct observation of Condon domain structures in silver by a system of ten micro Hall probes held close to the single crystal surface. In the homogeneous state, without domains, all probes show the same dHvA signal $B(H)$, i.e. all $B_i = B(H)$, where $i = 1, 2...10$ are the Hall probe numbers. In the domain state, the Hall voltages differ between the different probes in the paramagnetic part of the dHvA period. This implies an inhomogeneous magnetic field distribution due to Condon domains at the sample surface. In our measurements the surface of the crystal was either normal to direction of the applied magnetic field or slightly tilted (13°). By comparing data of neighboring Hall probes, new information about the Condon domain structure is extracted. At the end of this chapter exactly the same experiments are performed on a beryllium sample. Here, the magnetic field inhomogeneity at the surface due to Condon domains is expected to be bigger than for silver.

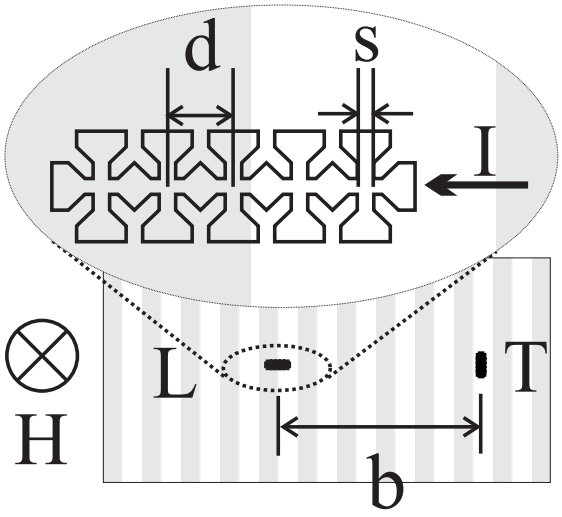

Figure 3.1: Experimental configuration with the longitudinal (L) and transverse (T) arrays of Hall probes at distance $b = 1$ mm ($s^2 = 10 \times 10$ μm^2; $d = 40$ μm). Shaded and non-shaded areas indicate a Condon domain structure with diamagnetic and paramagnetic domains, respectively.

3.2 Experiment

Figure 3.1 shows schematically the Hall probe setup made of a 1 μm thick Si doped GaAs layer sandwiched between two 10 nm thick undoped GaAs layers. The Hall probe setup has been presented in more detail in section 2.3.6. Two arrays of five Hall probes (10×10 μm^2 at 40 μm distance) are placed at a distance of $b = 1$ mm. One array, L, is oriented along the long axis of the sample; the other, T, transverse to this axis. A dc Hall current of 100 μA was applied in series to all five Hall probes of an array. The Hall voltages were read out simultaneously by five Keithley multimeters; the arrays L and T were measured one after another. Due to the 3D conducting layer the $V_i(B)$ characteristics of the Hall probes showed no quantum Hall effect and they were in good approximation linear up to 10 T even at 1.3 K. The correct calibration of the Hall probes was tested at temperatures between 4.2-3.6 K where all Hall probes showed exactly the same dHvA oscillations of the homogenous silver sample. The detection limit of the Hall probes was smaller than 1 G. A high homogeneity (better than 10 ppm in a sphere of 1 cm diameter) 10 T superconducting magnet was used to set a fixed offset magnetic field H_0. The slowly varying superimposed field H_V (±15 mT) was made by a water-cooled resistive coil. Thus the total applied magnetic field was $H = H_0 + H_V$.

The measurements were performed on a high quality silver single crystal of $2.4 \times 1.6 \times 1.0$ mm^3. The largest surface of the sample was normal to the [100]-axis of the crystal. The sample was prepared in the same way as in experiments on radio frequency

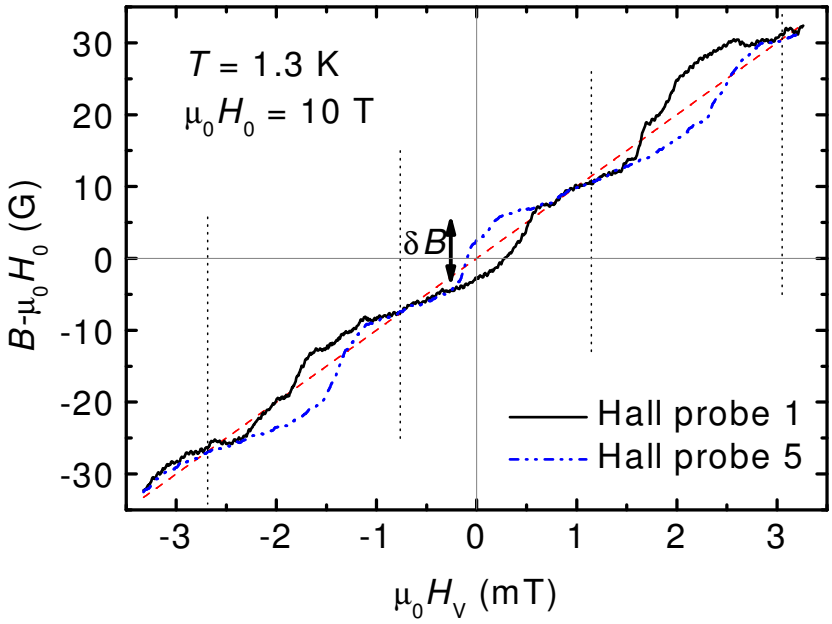

Figure 3.2: $B(H)$ trace for silver single crystal with $H \parallel [100]$ showing the splitting δB of B_1 and B_5 of the L-array for three dHvA periods separated by dotted lines. The dashed line is a guide to the eye for $B - \mu_0 H_0 = \mu_0 H_V$.

size effect [82, 83]. The sample was annealed in O_2 (10^{-2} Pa) at 750°C during 10 hours. It has a residual resistance ratio $R_{300\mathrm{K}}/R_{4.2\mathrm{K}} = 1.6{\times}10^4$, measured by the contactless Zernov-Sharvin method [84]. The very good quality of the sample results in a very low Dingle temperature, which was estimated from our measurements to be about $T_D = 0.2$ K. For a mirror-like surface, the crystal was slightly repolished by 0.1 μm diamond paste after annealing. The surface before polishing had a roughness of about 20-30 μm and the distance sample-Hall probe was too big so that no induction splitting due to Condon domains could be resolved. The sample was glued by narrow strips of cigarette-paper to the setup frame to fix the crystal on the Hall probes in order to avoid damage or strain of the single crystal upon cooling down. Moreover, the sample was slightly pressed by a spring and a cotton pad on the surface of the Hall probe setup to ensure a close contact. This procedure guaranteed that the sample was fixed reliably in high magnetic fields.

3.3 Results

Figure 3.2 shows typical $B(H)$ traces of Hall probes B_1 and B_5 of the L-array over three dHvA periods at 10 T and 1.3 K. At each paramagnetic part of the dHvA period, i.e. the steeper part of the period in the representation of figure 3.2, two different inductions are measured at the surface of the sample. At the diamagnetic part ($\partial M/\partial H < 0$), however, the induction is homogeneous. The measured traces are reversible for increasing and decreasing magnetic field[1]. We ascribe the measured difference between the induction of neighboring Hall probes to the existence of Condon domains.

The maximal induction splitting δB in a dHvA period was measured as a function of temperature at 10 T in figure 3.3a and as a function of magnetic field at 1.3 K in figure 3.3b. One can see in figure 3.3 that the induction splitting disappears at about 3 K at 10 T. This means that the phase boundary of the Condon domain state is crossed at about 3 K for this applied field. The solid line in figure 3.3a is a guide to the eye representing the induction splitting δB calculated with the LK-formula [29, 34]. We used for this calculation the phase transition temperature of 3 K and the maximum induction splitting in silver of 12 G, measured by Condon and Walstedt [4], as parameters. At 1.3 K, the crossing is expected to occur at about 5 T. The inset of figure 3.3a shows a theoretical phase diagram for silver with a Dingle temperature $T_D = 0.2$ K (see also section 1.6.2 and [34, 85]). We see that the field and temperature range for the occurrence of the induction splitting is in good agreement with the calculated Condon domain phase diagram. Moreover, it agrees as well with the experimental phase diagram obtained by nonlinear response measurements which will be presented in chapter 5.

As was mentioned above, the relative areas occupied by the two types of domains change when the applied magnetic field is slowly varied [4]. From the order in which the five Hall probes of an array detect the induction change, corresponding to the respective domain magnetizations, we can deduce the direction of the domain wall motion. Figure 3.2 shows an anomalous alternating transition order of the Hall probes between the diamagnetic and paramagnetic phase. In other words, in one period Hall probe 1 detects first the transition from the diamagnetic to the paramagnetic magnetization whereas in the following period it is Hall probe 5. Although reproducible, we will see that the observed order depends strongly on the experimental configuration. In the following we will examine in more detail the direction of the domain wall motion observed by the Hall probes within an array and compare the behavior between the L- and T-array.

A basically different behavior can be seen between the T-probes, shown in figures 3.4 and 3.4, and the L-probes shown in figure 3.5. No regular transition order was observed for T-probes. Sometimes, they transit in ascending (1-5) or in descending order. This

[1] Regarding the next chapter, the experiments presented here did not offer the possibility to determine whether there is a small hysteresis in the dHvA magnetization because all Hall probes were covered by the sample. Therefore, the applied magnetic field could not be determined with the required precision.

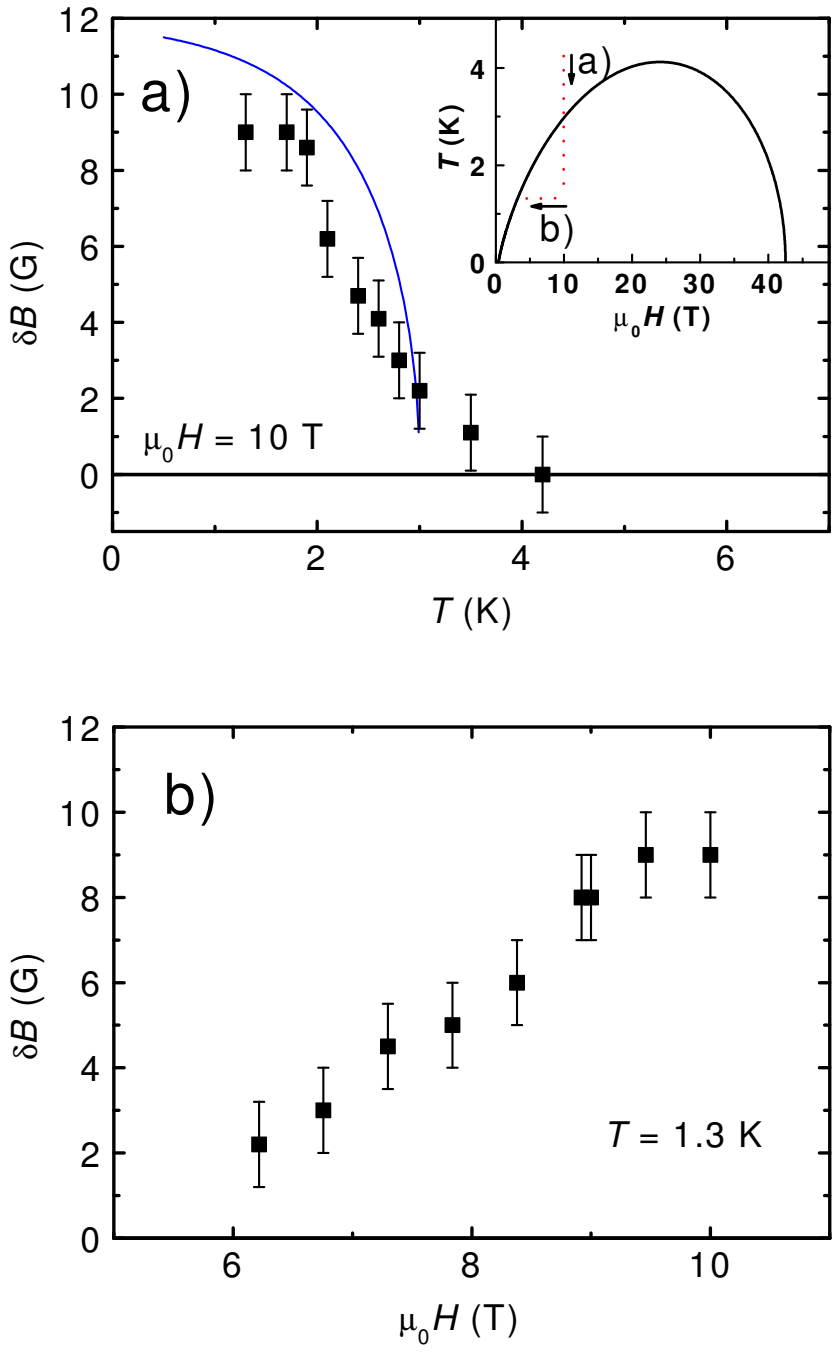

Figure 3.3: Maximum induction difference δB as a function of temperature (a) and magnetic field (b). Solid line in (a) is calculated from [34]. Inset shows the theoretical phase diagram [34, 85] with dotted lines (a) and (b) indicating the two measuring tracks.

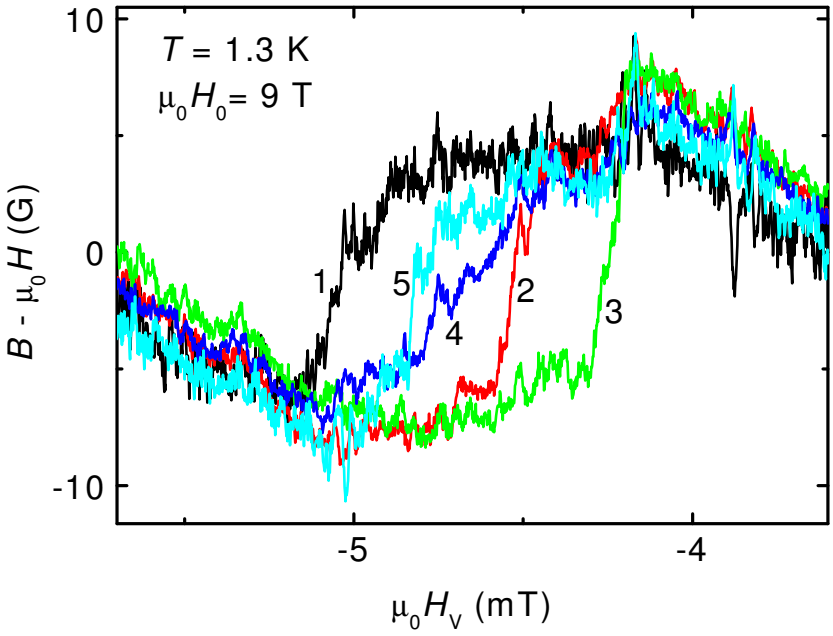

Figure 3.4: Example of successive transitions for five T-probes between the diamagnetic and paramagnetic phase. Here, the applied magnetic field was swept extremely slowly with about 0.5 mT/min.

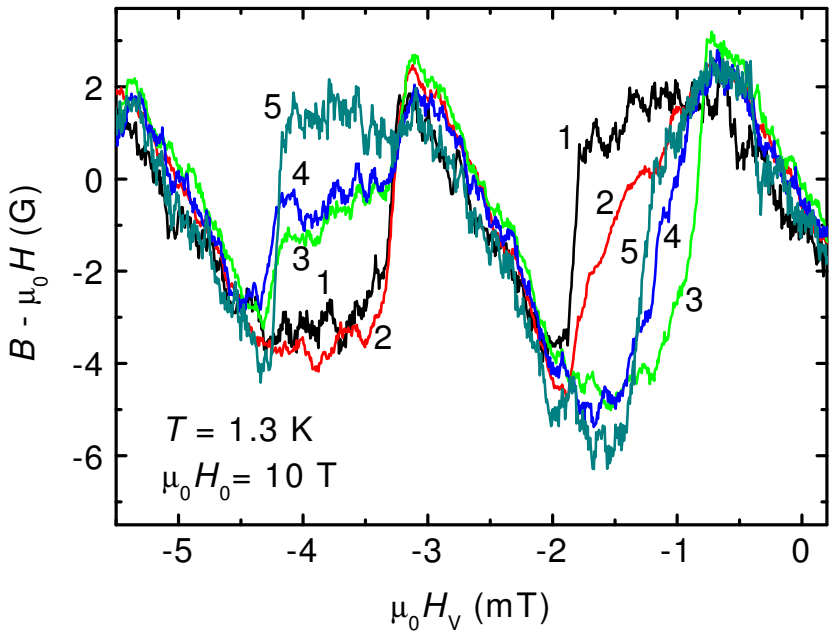

Figure 3.4: Example of successive transitions for five T-probes for two successive dHvA periods. The transition order varies from one period to the next.

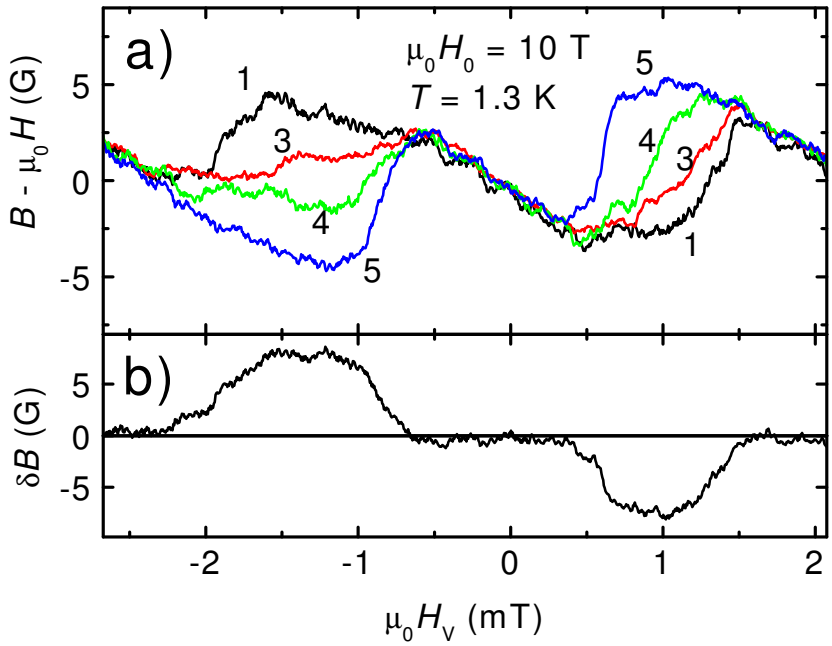

Figure 3.5: (a) Example of transitions for two dHvA periods for L-probes. The transition order is always either 1-3-4-5 or opposite.(b) shows the difference $B_1 - B_5$ vs H_V.

would imply that the domain boundaries are slightly tilted to the long axis of the sample. Sometimes, as shown in figure 3.4, a middle T-probe transits the last or the first, as if the domain wall is bent. In contrast, the transition order of the L-probes is always 1-2-3-4-5 or reversed, as it is shown in figure 3.5a. This implies that domain walls move always along the long side of the sample and that the domain structure is mainly oriented transverse to the long side of the sample.

However, we found that the L-probe sequence changes alternately between successive dHvA periods. This means that the domain wall motion changes direction along the long sample axis from one dHvA period to the next (see also figure 3.2). At the diamagnetic part of the dHvA period on the other hand, domains disappear completely and the sample is homogenously magnetized. One would expect that Condon domains, like intermediate state domains of type I superconductors, nucleate always at the same place in the sample volume, for example at defects, small scratches or at the sample edge [68]. After nucleation the domain walls would then propagate always more or less in the same direction. Here, however, we observed that the wall motion changes direction between successive dHvA periods. The sense of the domain wall motion can be expressed by the induction difference $\delta B = B_1 - B_5$, shown in figure 3.5b. δB changes sign alternately during four or five periods (see figure 3.8a). Then the, what we will call, "pendulum" effect breaks

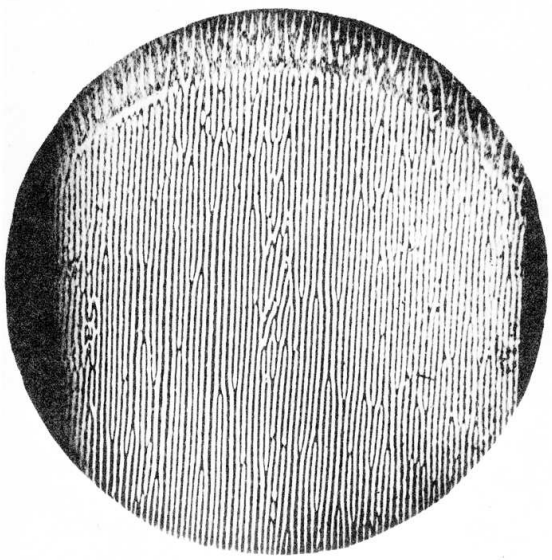

Figure 3.6: Laminar structure of superconducting and normal state domains observed in a tin disk. Normal state regions are dark. The ratio of the applied field H_a to the critical field H_c was $H_a/H_c = 0.95$ and $T = 2.165$ K. The applied field makes an angle of 15° with the surface. Photograph taken from [68] after [86].

down during two periods where the transition order is not clear. After this the pendulum effect repeats.

In the following we are going to tilt the sample with respect to the applied magnetic field. The idea to tilt the sample is motivated by an experiment by Sharvin [86] on intermediate state domains in a type I superconductor. He observed on tin that the intermediate state domain structure, being disordered in a symmetrical disk-shaped sample oriented perpendicular to the applied magnetic field, becomes laminar when the applied field makes an angle with the sample surface. An example of the laminar domain structure observed in a slanted field is shown in figure 3.6 [68, 86]. This experiment indicated the preference of the domain walls to align along the sample surface and to be parallel with the applied magnetic field. We expected that Condon domains behave in the same manner because, as was mentioned above, Condon domains can be considered as physically similar to intermediate state domains.

Figure 3.7a shows the magnetizations measured with the same Hall probes as in figure 3.5 after rotating the sample around the long sample axis by 13°. In fact, the entire chip carrier with the Hall probe setup, shown for example in figure 2.13, was rotated around its long axis together with the sample glued on it. This ensured that the distance sample-Hall probe was not changed. In figure 3.7a we see that the transition order is now the same for both dHvA periods and that the pendulum effect, observed above on the

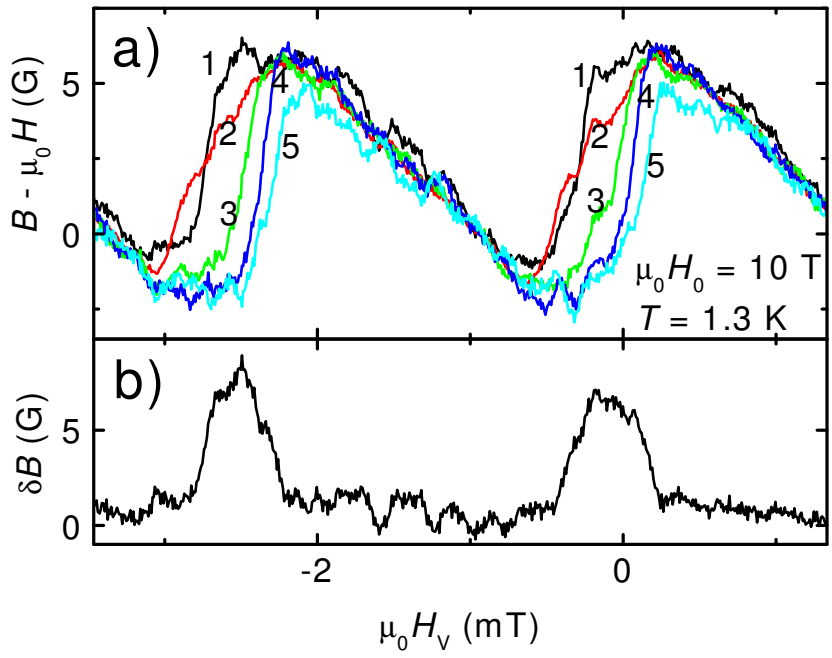

Figure 3.7: (a) Example of transitions for two dHvA periods for L-probes. The transition order is always either 1-3-4-5 or opposite.(b) shows the difference $B_1 - B_5$ vs H_V.

non-tilted sample, has disappeared. In figure 3.8 the behavior of δB before and after rotation, shown respectively in figure 3.5b and 3.7b, is compared for several dHvA periods. The transition order is the same for all dHvA periods in figure 3.8b. For the T-probes, on the other hand, the transition order did not essentially change under rotation from the previously observed behavior. We conclude that domains draw up to a regular laminar structure oriented always transverse to the long axis after rotation around the long sample axis by 13°. Furthermore, the pendulum effect disappeared after rotation.

The rotation of the silver single crystal with respect to the magnetic field affects the dHvA frequency spectrum. Figure 3.9 shows the difference in the dHvA spectra and waveforms between the non-tilted and the tilted sample. For the non-tilted situation (see figure 3.9a and b), where the magnetic field is applied along the [100]-axis of the crystal, several frequencies are observed in the Fourier transform of the dHvA oscillations[2]. They are due to other orbits, e.g. the four-cornered rosette orbit at about 19700 T, which exist for this orientation as a consequence of the multiply connected Fermi surface of silver (see chapter 1 and [11]). Taking into account the main frequencies, the dHvA magnetization

[2]The Fourier transforms are obtained from Hall probe measurements over a large field range. For the magnetic field sweeps the lowest speed (1 G/s) of the magnet power supply was used. The water-cooled resistive coil was disconnected.

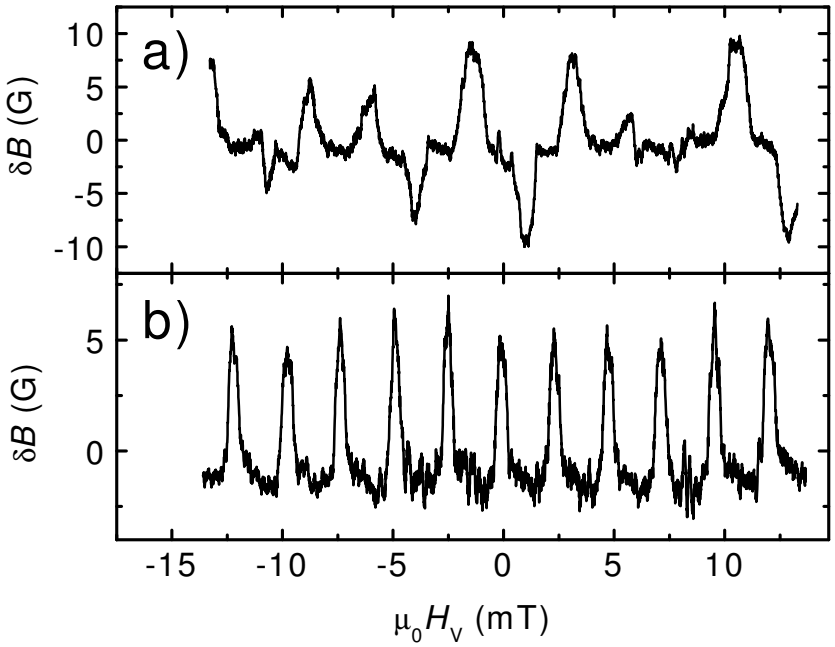

Figure 3.8: (a) "Pendulum" effect for sample surface oriented normal to **H** showing a regular change of sign in the difference signal $\delta B = B_1 - B_5$ during 4 or 5 periods. (b) Same dependence for the 13° tilted sample. In both the temperature was 1.3 K and the offset magnetic field was $\mu_0 H_0 = 10$ T.

waveform was then synthesized in figure 3.9b. We see that the magnetization amplitude varies strongly between successive periods. For the slightly tilted sample (see figure 3.9c and d), on the other hand, only the frequency due to the "belly" orbit exists. This leads to a dHvA magnetization without any frequency beat pattern.

The beating pattern in the dHvA magnetization for the non-tilted orientation might play a role in the occurrence of the pendulum effect. In this respect we note that the dHvA magnetization alternates between small and high amplitude during five dHvA periods, marked by the rectangles in figure 3.9b. This is compatible with the observed pendulum effect of figure 3.8a if we assume that the domain wall motion changes direction for low and high dHvA amplitude, respectively. Even though there is strong evidence that the occurrence of the pendulum effect is linked to the complicated frequency spectrum of the non-tilted sample and not to the geometry of the sample or a memory effect, the circumstances should be tested in more detail. For this purpose a plate-like silver sample should be prepared where the $[100]$-axis of the crystal is slightly inclined with respect to the surface of the parallelepiped.

The transitions of the individual Hall probes are very sharp (see figure 3.4) compared

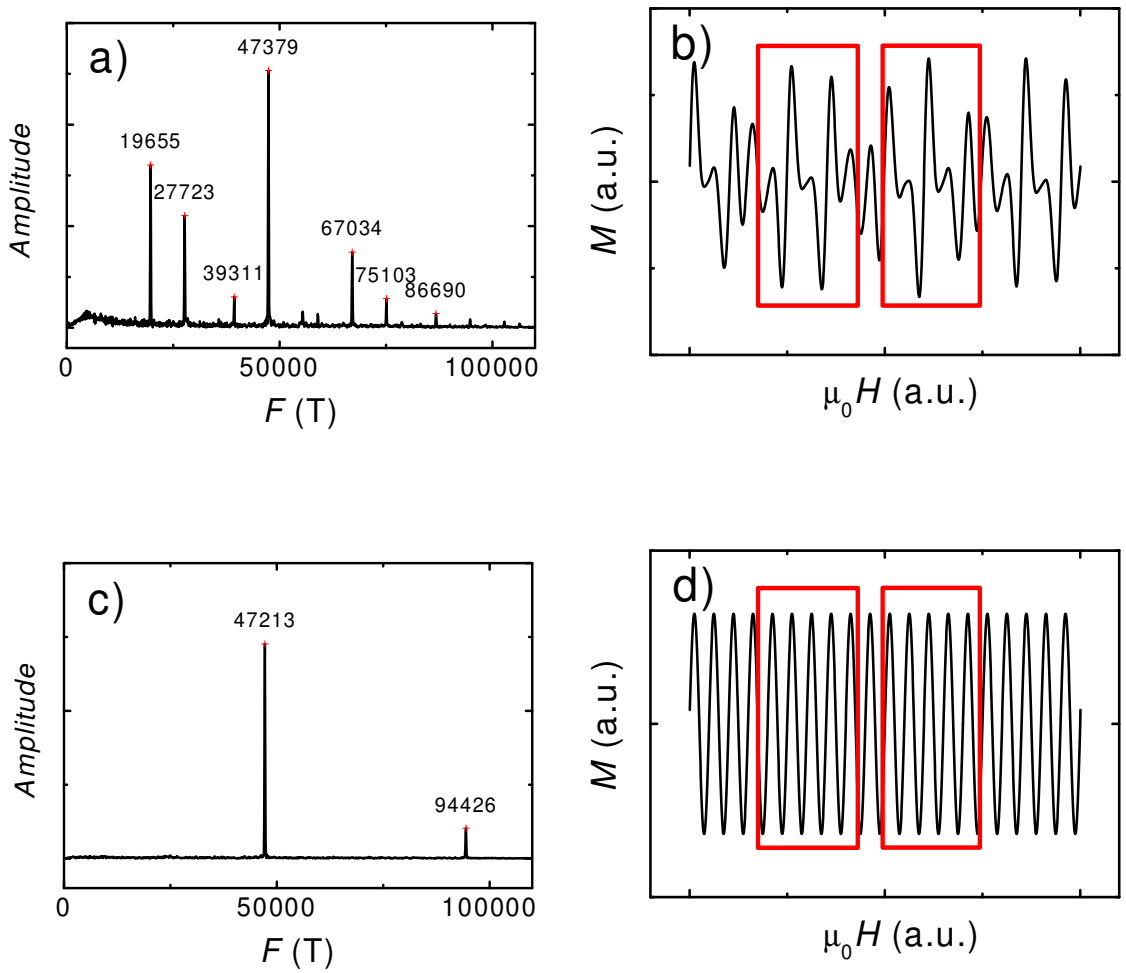

Figure 3.9: Possible origin of the pendulum effect. (a) Fourier transform of the dHvA oscillations for the non-tilted sample. In addition to the main frequency at 47300 T several other frequencies occur. (b) dHvA waveform simulated using the fourier spectrum of (a). (c) Fourier transform of dHvA oscillations measured on the tilted sample. Only the "belly" frequency remains. (d) dHvA waveform corresponding to (c). The rectangles in (b) and (d) mark five dHvA periods, respectively. boxes

to the whole field range of the domain state especially when the applied magnetic field is increased very slowly. This means that the thickness of the domain wall is much smaller than the period of the domain structure. Moreover, a single Hall probe has never detected more than one transition during a dHvA period. This implies that we saw always only one boundary or domain wall between a dia- and a paramagnetic domain within the range of five successive Hall probes. This means, however, that the period of the domain structure is certainly bigger than the distance of ≈ 150 μm between the edge Hall probes of an array. This lower limit for the domain period p should be compared with the value obtained from the square-root averaged expression

$$p \propto \sqrt{wt} \tag{3.1}$$

for a sample with thickness t and domain wall thickness w, introduced in chapter 1 [11]. With the proposed cyclotron radius for the wall thickness (1 μm at 10 T in silver), one obtains at least a five times smaller value ($\approx$ 30 μm) [4] for the period of the Condon domain structure. If we insert, on the other hand, the lower limit of the domain period of 150 μm in formula (3.1) we find a domain wall thickness of $\approx$ 20 μm. This is in agreement with the observation that two neighboring middle L-probes, which are separated by 40 μm, show often intermediate but different induction values. Therefore, the thickness of a domain wall can not be much smaller than 20 μm.

As the real domain pattern turns out to be somewhat bigger than expected, we need either a new setup with better adapted Hall probe distances or a scanning Hall probe for more detailed measurements of the domain structure. Another idea would be to reduce the thickness of the sample. According to formula (3.1) the period of the domain structure should decrease in this case and we should be able to detect a complete domain period with the existing Hall probe setup. On the other hand it would be more difficult to resolve the magnetization difference due to the domain structure because the distance sample-Hall probe remains the same.

3.4 Beryllium

Exactly the same measurements as presented above were performed on a beryllium sample of $4.5 \times 1.0 \times 0.8$ mm^3 cut from the same single crystal on which Condon domain formation was observed using muon spectroscopy [5, 28, 29]. The largest surface, being normal to the $[0001]$-axis of the crystal, was prepared with a quality comparable to the silver crystal. Figure 3.10a shows dHvA oscillations observed with Hall probe 1 and 2 of the L-array around the beat antinode at 4.8 T. Their amplitude is about four times bigger compared to the dHvA amplitude observed on silver at 10 T. Consequently we expect a much bigger δB inside the crystal than in silver. The sizes of the domain structures, on the other hand, should be similar for both samples because their thicknesses and the cyclotron

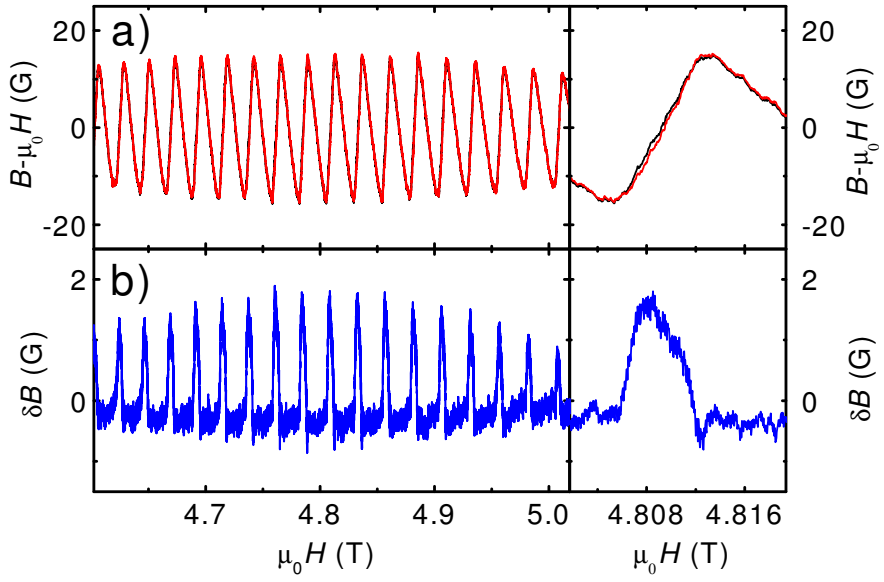

Figure 3.10: (a) dHvA oscillations in beryllium measured with Hall probe 1 and 2 of the L-array at 1.3 K. (b) shows the difference $\delta B = B_1 - B_2$ versus H. On the right side are respective zooms.

radii, at the respective applied magnetic fields, are roughly the same (see formula (3.1)). However, figure 3.10b shows that only a $\delta B < 2$ G is detected at the sample surface. We conclude from these measurements that Condon domains do not emerge to the sample surface in beryllium like it was observed on silver. The attempt of Condon and Walstedt to find domains in beryllium by NMR was not successful, either [4]. The authors gave explanations related to the quadrupole broadening and the long nuclear thermalization time in beryllium. However, now we believe that the main reason is the absence of an induction splitting δB at the sample surface.

This could be an intrinsic property of beryllium related to its anisotropic magnetostriction [87, 88]. Another reason could be that the crystalline quality of the beryllium sample decreases close to the surface. In this case dHvA effect would not be possible in a surface layer of finite thickness. As a result the Hall probes would be too far from the domain structure so that only a small induction splitting would be resolved. The surface layer could, in principle, be reduced by annealing the sample, like it was done with the silver sample. However, annealing beryllium is very difficult because extremely high temperatures are needed and beryllium vapor is very toxic.

3.5 Conclusion

In conclusion, Condon domains in silver with an induction splitting up to 10 G were observed by micro Hall probes at fields and temperatures which are in agreement with the theoretically estimated phase diagram. A laminar domain structure was found with the orientation mainly transverse to the long sample axis. The domain motion was always reversible for increasing and decreasing magnet field. However, the question of small hysteresis in the dHvA magnetization was not addressed in these experiments. Moreover, for the sample oriented perpendicular to the applied magnetic field a strange alternating change of the domain wall propagation was observed during several dHvA periods. This effect disappeared for a slightly tilted sample. From the known dimensions of the Hall probe array we could deduce that the domain period is not smaller than 150 μm and the domain wall thickness must be about 20 μm. The same experiments were made on a beryllium sample. Here, only a induction splitting of 2 G was measured at the surface and we conclude that Condon domains do not emerge to the surface in beryllium.

Chapter 4

Hysteresis in the dHvA effect

Dans ce chapitre, on va étudier la réversibilité de l'aimantation d'un échantillon en présence de domaines de Condon. Les calculs théoriques ont montré que la transition entre l'état homogène et l'état avec domaines est de premier ordre. En principe, l'hystérèse de l'aimantation accompagne une telle transition de phase. D'abord on détectera l'hystérèse à l'aide des sondes de Hall en variant lentement le champ magnétique appliqué. Comme l'hystérèse mesurée est très petite, on vérifiera ces observations à l'aide des mesures de susceptibilité AC. En présence des domaines de Condon, à très faible amplitude de modulation, la susceptibilité n'est plus linéaire en fonction de l'amplitude. Par ailleurs, la troisième harmonique de la susceptibilité montre des valeurs exceptionnellement grandes. Ces observations sont expliquées par la présence des domaines de Condon, responsables de l'hystérèse de l'aimantation.

4.1 Introduction

It is well known that the irreversibility of the magnetization process by domain wall motion is due to energy barriers arising from a variety of defects inside magnetic material [10, 89]. The resulting hysteresis effects in usual magnetic substances, i.e. in substances where the atomic magnetic moments, due largely to the electron spin, are the reason of magnetism, have been investigated in detail in the past. However, in an applied magnetic field, the orbital motion of free electrons in metals leads also to magnetization. For Landau quantization [90] of the electronic system the oscillating magnetization (dHvA effect) has been extensively studied in single crystals at low temperatures [11]. There is no experimental data reporting hysteresis in the dHvA effect apart from the trivial

case caused by eddy currents when the applied magnetic field is varied fast enough [47].

After the discovery of Condon domains [3, 4] hysteresis in the dHvA effect needs to be considered again. Indeed, the Condon domain state (CDS) consists of two phases of different induction values with a magnetization current in the domain walls. This needs usually extra energy. It was shown that the transition from the homogeneous state to the CDS is of first order [7]. At this phase transition one could expect, in principle, all phenomena like irreversibility, supercooling and hysteresis that exist at first order phase transitions, e.g. the liquid - gas transition. Naturally, Condon discussed these problems in his first paper on domains [3] concluding that neither supercooling nor hysteresis had been observed in all reported data. Since then, the above phenomena were discussed in several papers [9, 14]. Despite of the fact that Condon domains themselves have been observed and investigated experimentally [5, 29, 88, 91], there is nevertheless up to now no experimental data proving hysteresis.

In this chapter we present the first experimental observation of hysteresis in beryllium single crystals. The hysteresis itself turns out to be very small. Therefore, several methods were used to prove the existence of hysteresis. First the hysteresis effect is measured directly by Hall probes in dc fields, then a standard ac method is used with various modulation levels, frequencies, and magnetic field ramp rates. Finally, the dc hysteresis loop is reconstructed by assembling several higher harmonics of the ac pickup voltage. Moreover, it is shown that the Condon domain phase diagram can be measured directly from the response to sufficiently small ac fields. Finally, Plummer's [92] strange and up to now only incompletely understood data is explained.

4.2 Experiment

Beryllium is to our knowledge the best metal to investigate hysteresis effects related to Condon domain formation. First, due to its cigar-like Fermi surface (small curvature at the maximal cross sections) the dHvA amplitude is very high for $\mathbf{H} \parallel [0001]$. Secondly, in this configuration two rather close dHvA frequencies 970 T and 940 T coexist leading to a beat in M and χ. Because of this beat there is the unique possibility to change the dHvA amplitude and the critical parameter χ by a factor three at constant T by varying the magnetic field only very little. Thus, experimental conditions can be adjusted so that the transition to the inhomogeneous CDS occurs in a part of each beat period. The sample was cut from the same piece that was used earlier for the preparation of the plate-like sample in which Condon domains were first observed by μSR [5]. The results shown here were measured on a rod-like sample of size $8 \times 2 \times 1$ mm^3 with the long axis parallel to $[0001]$. The Dingle temperature was $T_D = 2.0$ K. The measurements were made either directly by a micro Hall probe placed close to one end of the sample or by a compensated pickup coil using low frequencies of about 21 Hz and small modulation level (< 6 G).

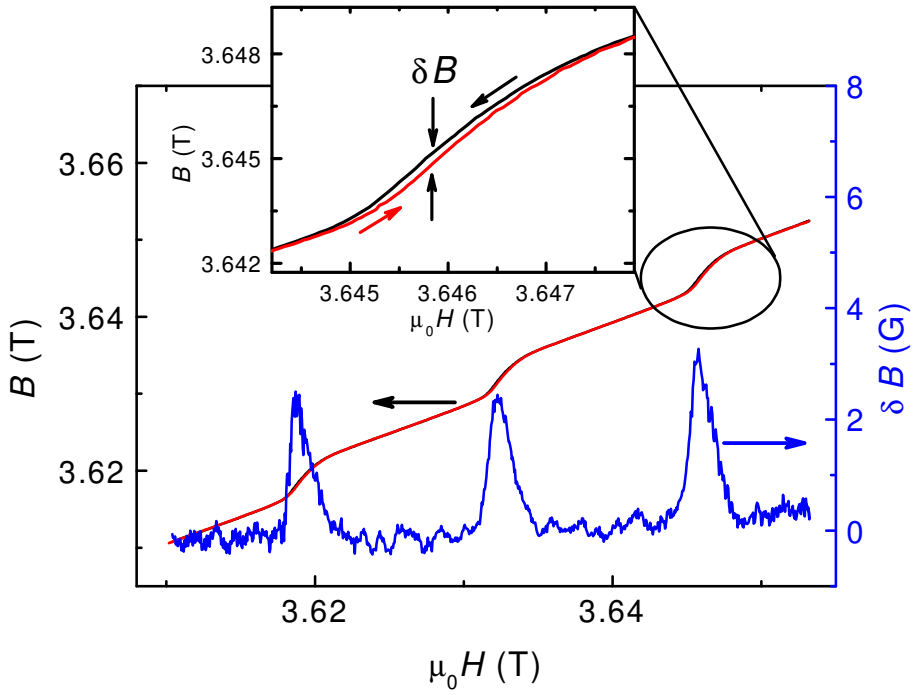

Figure 4.1: Hysteresis loop observed by Hall probes in the paramagnetic part of the dHvA oscillations of beryllium. $B(H)$ traces for an up and down sweep of the applied magnetic field around a dHvA antinode at 3.6 T and $T = 1.3$ K (scale on the left). The hysteresis loop is visible in the inset. The induction difference δB between these curves shows the value of the hysteresis (scale on the right).

The Hall probes used here were presented in section 2.3.6 and the pickup coil system was discussed in section 2.2. The experiments were carried out in a 10 T superconducting coil with homogeneity better than 10 ppm in a sphere of 1 cm diameter.

4.3 Results

Figure 4.1 shows Hall probe traces for an up and down sweep of the applied magnetic field around a dHvA antinode at 3.6 T and at $T = 1.3$ K. The hysteresis loop is very small and only visible by a zoom. A periodically arising induction difference δB of about 3 G between the up and down sweep is measured at the steeper part, i.e. the paramagnetic part, of each dHvA period. The signal is about ten times higher than the noise level. The applied field is measured here by another Hall probe, placed sufficiently far from the sample, as the superconducting solenoid has its own small hysteresis when the current is swept. The particularity of these measurements is that both, the applied magnetic field

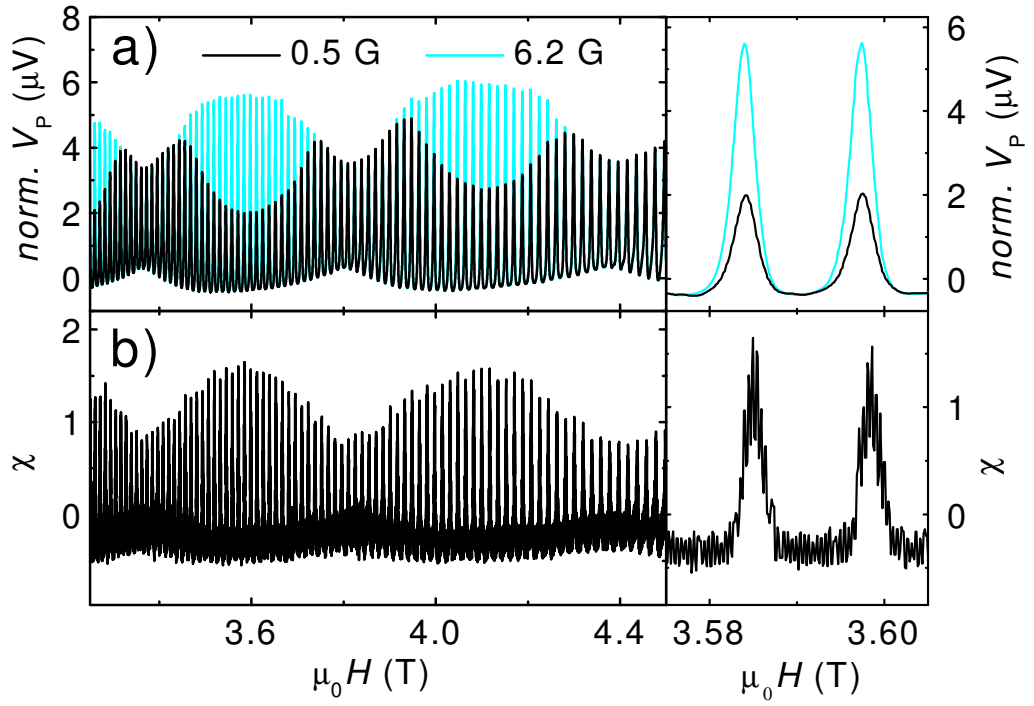

Figure 4.2: (a) Pickup voltages divided by the modulation level for low and high modulation amplitude at 1.3 K. (b) Dc susceptibility derived from magnetization measurements with Hall probes without field modulation. Graphs to the right show respective zooms.

and the magnetization are measured with high precision. The hysteresis effect is clearly observed in figure 4.1 using dc Hall probes but rather under the most favorable conditions at 1.3 K around a maximum of a magnetization beat. The dc Hall technique is not sensitive enough to study hysteresis as a function of temperature and field.

A standard ac modulation method with a compensated coil system used at *very* low modulation level h is much more sensitive to detect nonreversible magnetization or hysteresis. This method is used to determine exactly the point of its appearance. If the modulation amplitude h is much smaller than the oscillation period ΔH, the measured response corresponds in good approximation to the derivative, i.e. the susceptibility $\chi(H) = \partial M/\partial H$ (see section 2.2 and [11]). If the modulation is further decreased, the result should not change, the measurements should only be more precise.

Figure 4.2 shows a different behavior as a function of modulation field amplitude h. All $\chi(H)$ curves of figure 4.2a and b are measured at low temperature where in the regions of each antinode hysteresis exists like it was shown in figure 4.1. Figure 4.2a shows the normalized pickup voltage, i.e. response divided by the modulation level, measured by the ac method with 6.0 G and 0.5 G modulation amplitude. In both cases $h \ll \Delta H$

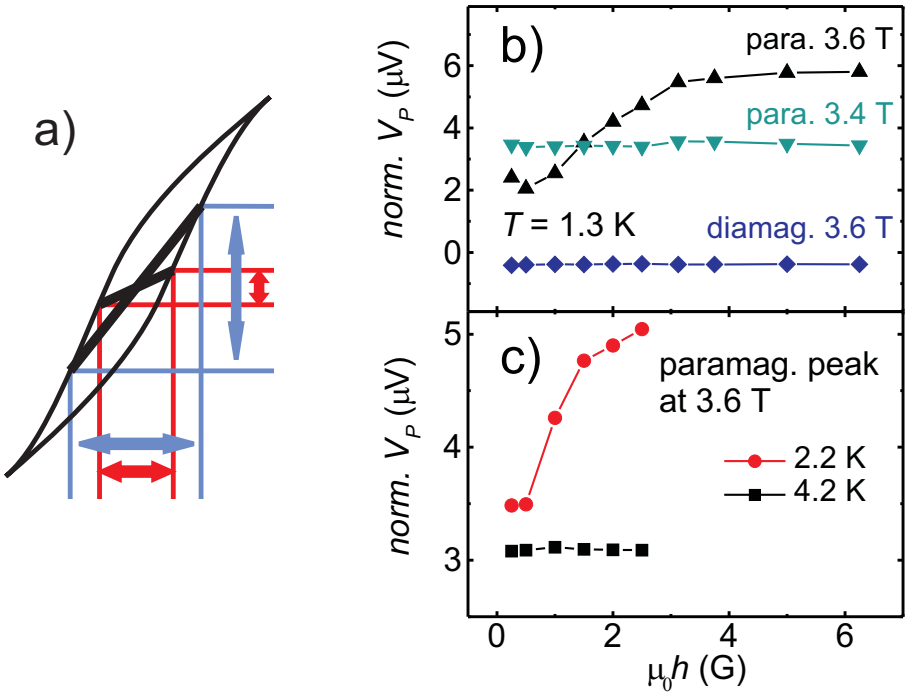

Figure 4.3: (a) Schematic representation of the hysteresis loop showing that the response to an applied ac modulation field is nonlinear. (b) Modulation level dependence of the normalized pickup voltage for characteristic magnetic fields at 1.3 K. (c) The same dependence at the antinode at $T = 2.2$ K and $T = 4.2$ K. Nonlinearities arise at a critical temperature of 3.2 K.

so that one could expect identical curves. In fact, both curves are completely congruent except at the regions near the antinodes. Here, only the high modulation level (6 G) gives the expected result, which is the well known dHvA oscillation beat of beryllium. For comparison figure 4.2b shows $\chi(H)$, calculated from $B(H)$ curves measured with Hall probes like in figure 4.1 without field modulation. For small modulation amplitude deep "notches" in the dHvA oscillation envelope are observed. The notches occur at magnetic fields where the dHvA amplitude is big enough that Condon domains arise. Instead of a further increase, after having crossed the critical point, the dHvA amplitude decreases at the paramagnetic ($\chi > 0$) part of the dHvA period only. The diamagnetic part does not change.

One would expect that dHvA oscillations $M(H)$ oscillate in average around zero magnetization (see figure 1.14). This requires that the areas under the paramagnetic $\chi(H) > 0$ part and under the diamagnetic $\chi(H) < 0$ part are equal in each dHvA period. Then the integral of $\chi(H)$ over one dHvA period is zero. On can see in figure 4.2a that this is indeed the case for the waveform measured with high modulation level. For the small modulation level, however, the areas are certainly not equal for magnetic fields where the

notches appear because the diamagnetic part remains unchanged whereas the amplitude of the paramagnetic part is reduced. This shows that the small modulation measurements can not correspond to the real $\chi(H)$ waveform. The amplitude decrease is absent at temperatures $T > 3.2$ K and at the nodes of the dHvA beat where the single crystal is in the homogeneous state.

The decrease of the dHvA amplitude at low modulation level is schematically shown in figure 4.3a. If the modulation is much bigger than the width of the hysteresis δH the ac response corresponds in good agreement to the slope, i.e. $\chi(H)$. As soon as the modulation becomes comparable to the hysteresis loop size the response decreases [89]. The effect was measured for several modulation levels at different temperatures and at different magnetic fields with respect to the dHvA beat phase. The results are shown in figure 4.3b and c. The modulation level where the dHvA amplitude decreases gives the hysteresis width δH which agrees with the above observed values of δB. No decrease is observed at temperatures $T > 3.2$ K and near the beat nodes.

This explanation is checked in another way. Usually the applied magnetic field H ramps much slower than the ac modulation field h, i.e. the full magnetic field $H + h$ always oscillates around the quasi static offset field H and $B(H + h)$ makes a loop in presence of hysteresis. If the ramp rates are changed in a way that $\mathrm{d}h/\mathrm{d}t$ and $\mathrm{d}H/\mathrm{d}t$ are the same, then the magnetic field sweeps only forward with small steps in the direction of the ramp. Under this condition $B(H + h)$ never makes a loop as we go always along the hysteresis loop boundary and never inside. In this regime, which is usually not used, the lock-in amplifier does not measure the correct amplitude. Nevertheless, we observed in this regime the usual dHvA beat signal without notches.

The notches in the envelope of the first harmonic in-phase ac response are "compensated" by steeply rising higher harmonics at the same critical point. At the same field a phase shift appears in the pickup voltage. This means that the response to an ac modulation becomes extremely nonlinear in the presence of hysteresis. Figure 4.4 shows the third harmonic (a) and the imaginary part (b) of the pickup voltage in a wide region of magnetic field at 1.3 K. The amplitude is big in both curves only around the beat antinodes. In the regions of nodes the signal is about zero. The inset of figure 4.4a shows the 3^{rd} harmonic in the same field interval as in figure 4.2. The comparison shows that the signal appears and disappears with a threshold character at the critical points of the transition to the CDS. The inset in figure 4.4b shows schematically that the response to an initially sinusoidal modulation field becomes highly distorted in the presence of a hysteresis loop. The response becomes more rectangular shaped like a window-function. This function can be composed, as it is well known, of odd harmonics of a sine. This explains that the third harmonic content of the pickup voltage is very high in the CDS. At magnetic fields without hysteresis the 3^{rd} harmonic is very small as the modulation level $h = 2.5$ G is much less than the dHvA period of about 130 G at 3.6 T.

The hysteresis shape and size is reconstructed in figure 4.5 like e.g. in [93]. The

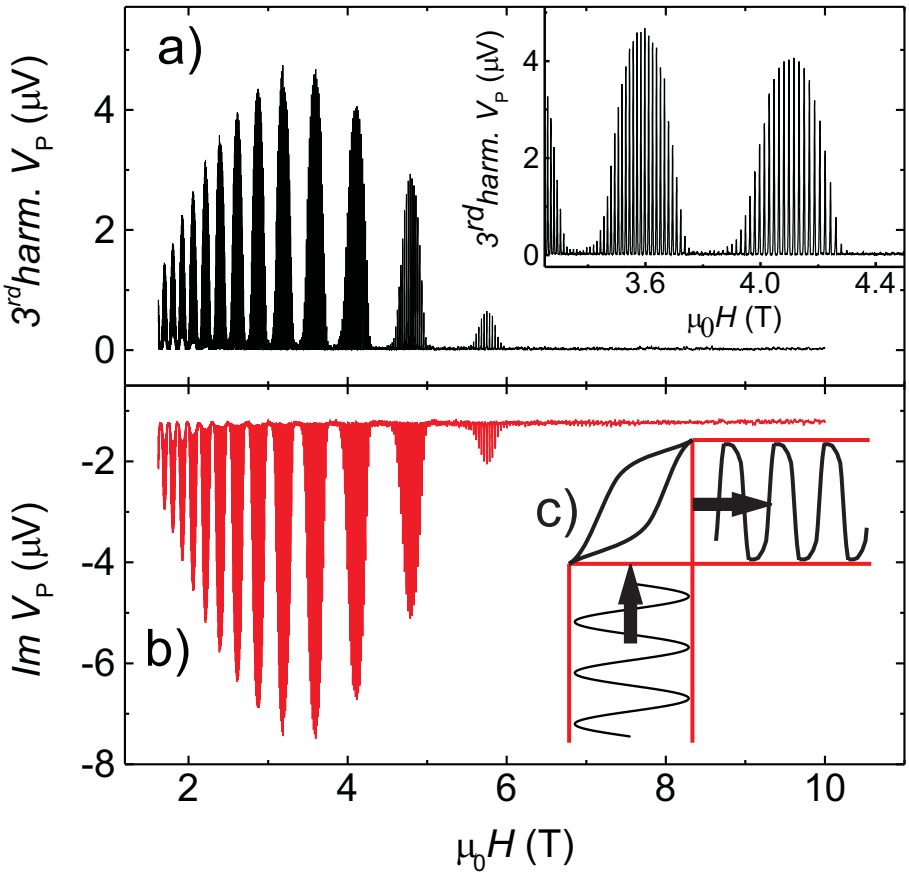

Figure 4.4: (a) Third harmonic of the pickup voltage. The inset shows a zoom to the above discussed field range. (b) Out of phase part of the pickup voltage. (both at 2.5 G modulation level and 1.3 K). The inset shows a schematic representation of the hysteresis showing that the response to a sinusoidal field modulation becomes window shaped and is slightly phase shifted with respect to the input.

response to the sinusoidal modulation of 2.5 G amplitude is calculated by adding all in- and out-of-phase contributions up to the fifth harmonic. The same procedure was applied at different positions along the dHvA oscillations. At the diamagnetic part ($\chi < 0$) of every dHvA period all harmonics vanish and only the in-phase response persists. Hence, a line with negative slope is calculated. The same behavior is found for $\chi > 0$ around a node with a line with positive slope. Whereas at the paramagnetic part in the region of the notches hysteresis arises and its size is maximal at the dHvA beat antinode.

The observed threshold behavior of the third harmonic and of the out-of-phase signal does not essentially change when the modulation level is varied. This behavior was observed in the frequency range from 8 Hz up to about 200 Hz. Thus, these measurements

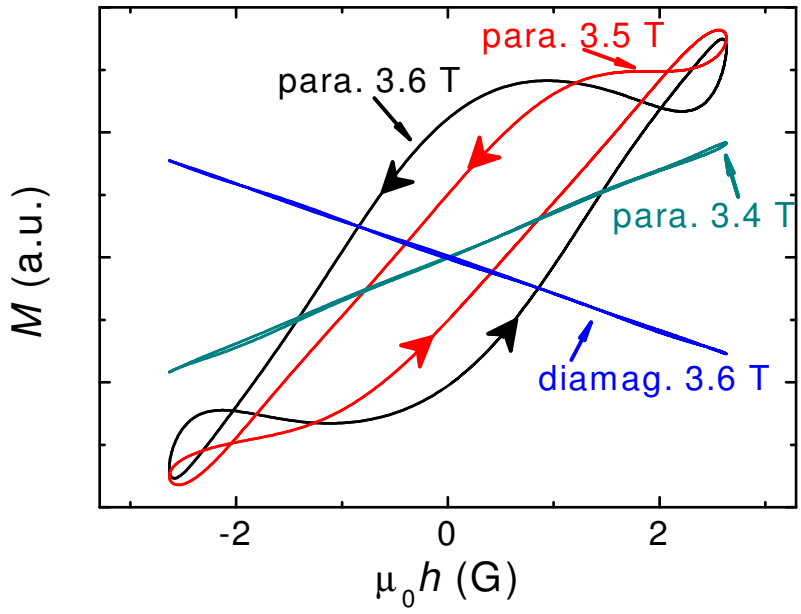

Figure 4.5: Hysteresis shape reconstruction for modulation amplitude 2.5 G for several characteristic magnetic fields at 1.3 K.

offer a simple way to determine the Condon domain phase diagram.

4.4 Discussion

Hysteresis may explain the data measured by Plummer [92] with an ac mutual inductance method at low modulation level. Plummer first interpreted the observed dHvA waveform as a consequence of a new dHvA frequency. As the Fermi surface of beryllium was not consistent with this frequency, eddy currents at the rather high frequency of 100 Hz were invoked [47, 94]. A comparison of Plummer's data with our results (see figure 4.6) shows the similarity. The deep notches in the dHvA oscillation envelope seem indeed to be the result of a new frequency. However, if we increase the modulation amplitude the notches disappear and the known dHvA waveform is obtained. In figure 4.6 we repeated Plummer's measurements at higher frequencies and found the same behavior. In the following we will check whether the notches at the beat antinodes persists down to very low modulation frequencies in order to rule out effects due to eddy currents.

In section 2.2 and in [47] a frequency limit for field modulation methods is calculated. For frequencies higher than this limit eddy currents might considerably influence the dHvA waveform. According to equation (2.9) the limiting frequency is very low especially in metals at low temperatures because the conductivity is very high. To exclude

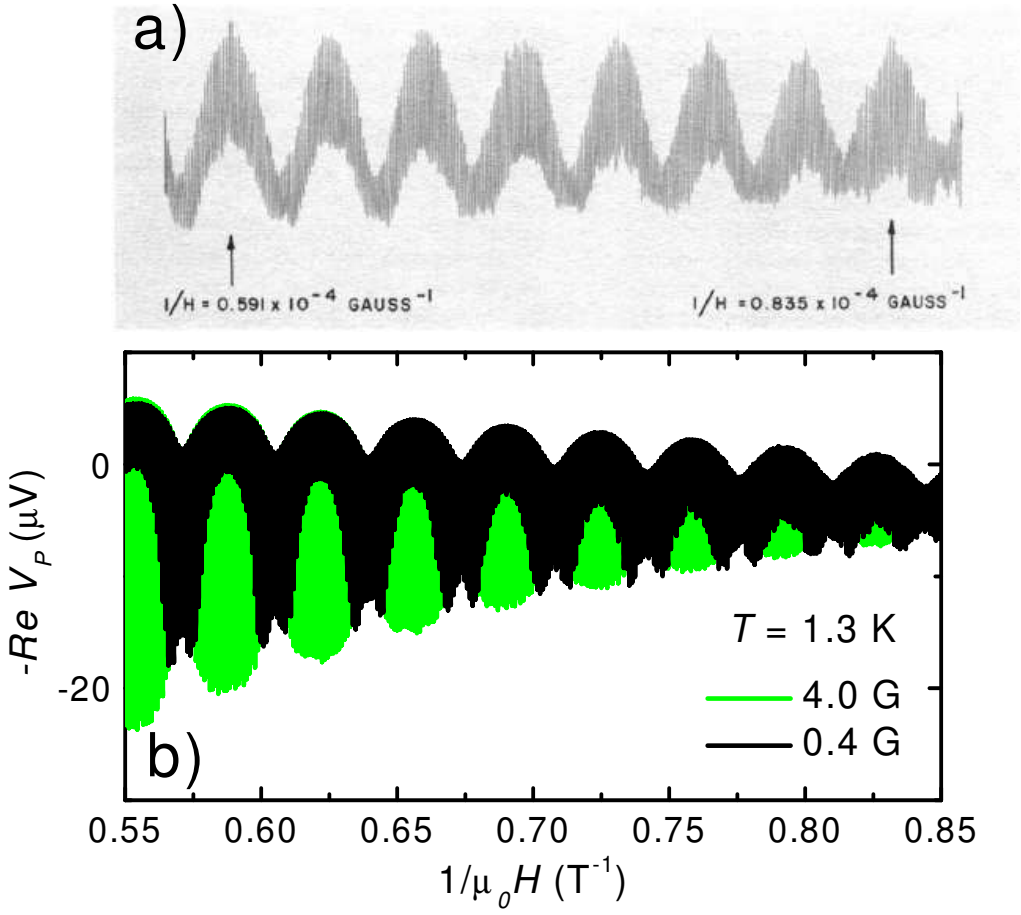

Figure 4.6: (a) Susceptibility measured by Plummer [92] on a rod-like sample with 0.25 mm diameter and 10 mm length at 2.0 K with 100 Hz modulation frequency and 0.5 G amplitude. (b) Susceptibility measured on our rod-like sample at 1.3 K with 160 Hz at low and high modulation level.

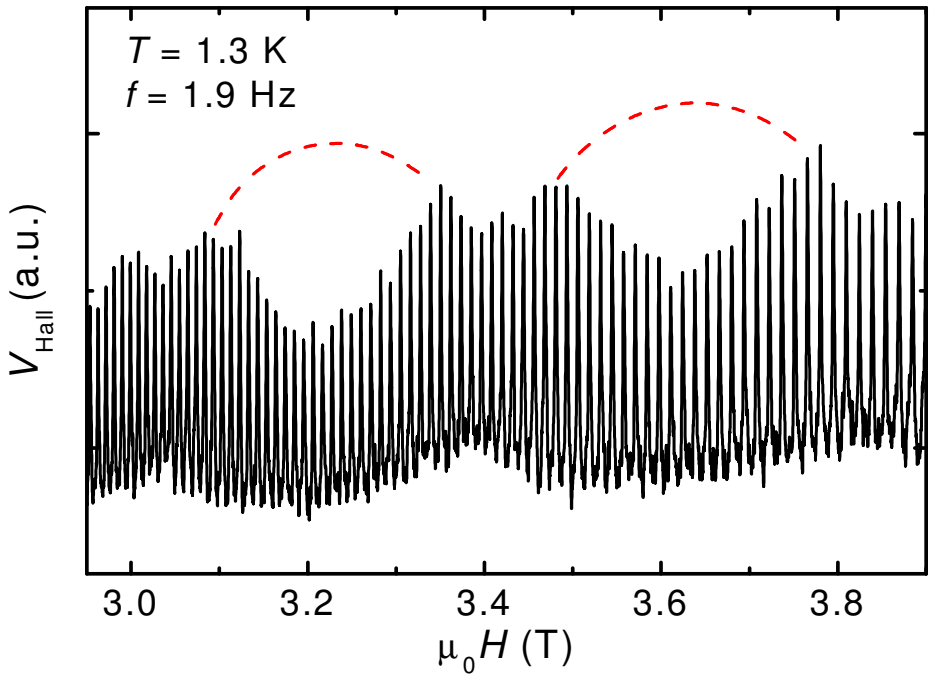

Figure 4.7: Susceptibility measured at 1.9 Hz and 1.0 G modulation amplitude with a Hall probe placed close to one end of the rod-like beryllium sample. The notches in the dHvA oscillation envelope exist even at this low frequency. The dashed lines indicate the expected envelope of the dHvA oscillations.

reliably eddy currents as the reason for the nonlinearity of the pickup voltage we made ac modulation measurements at very low frequencies (1.9 Hz). For these measurements we used a Hall probe because the pickup voltage of the coil system vanishes at this very low frequency. The Hall probe setup presented in section 2.3.6 was used like in chapter 3 with a dc current. The Hall probe was placed as close as possible to one end of the rod-like beryllium sample. A small ac modulation field with an amplitude of 1.0 G was applied and the Hall voltage was measured with a phase sensitive detection. The resulting signal from the lock-in amplifier is proportional to the susceptibility of the sample ($\propto 1 + \partial M/\partial H$). Figure 4.7 shows that the same notches appear in the susceptibility at the antinodes of the dHvA waveform like in figure 4.2a for small modulation level. These measurements show that the notches in the dHvA oscillation envelope exist in a large modulation frequency range. Therefore, eddy currents can not explain this behavior but rather the hysteresis loop observed with Hall probes in dc fields in figure 4.1.

Hysteresis accompanies without doubt the appearance of the CDS. For any sample

shape, not only in plate-like samples, two phases B_1 and B_2 with domain walls between them coexist in the CDS. The wall motion and pinning might, in principle, depend on the sample shape. Therefore, a plate-like sample was measured in the same T and H range. We found the same phase diagram for hysteresis formation in both samples. The hysteresis size, however, needs to be investigated more precisely as function of temperature, magnetic field and for various n.

Hysteresis itself is a result of interaction or pinning of domain walls with defects, impurities and the surface of the crystal. Moreover, the question of domain wall motion can not be neglected in many phenomena like e.g. acoustic wave propagation and absorption, and helicon waves [91]. Recently, the question of Condon domain wall motion was considered in detail theoretically [95]. Unfortunately, an idealized model of a domain wall was used without taking into account the direct link with lattice deformation [88] and the metastable behavior due to hysteresis.

4.5 Conclusion

In conclusion we have shown that hysteresis occurs in the dHvA effect under the conditions of the Condon domain state. The observed hysteresis loop width is rather small, only a few Gauss. Due to the hysteresis deep notches appear in the dHvA oscillation envelope of the ac susceptibility measured at low modulation amplitude. Furthermore, we have shown that the out-of-phase part and the third harmonic of the pickup voltage rise steeply when a hysteresis loop arises in the dHvA magnetization of the sample. This threshold behavior is independent on the modulation frequency and amplitude and offers therefore a simple and robust possibility to measure a Condon domain phase diagram.

Beryllium, as mentioned above, is certainly the best candidate to observe this new effect. In other metals, like for example silver or gold, the hysteresis loop is expected to be even smaller than in beryllium because the dHvA frequencies are much higher and consequently the dHvA period much smaller. This makes it certainly impossible to observe the hysteresis loop directly with Hall probes. However, we will see in the next chapter that analogous features in the pickup voltage are discovered on silver with the ac modulation method. This makes us believe that hysteresis occurs in the dHvA effect of all metals that exhibit Condon domain formation.

Chapter 5

Experimental phase diagrams of the Condon domain state

Dans ce chapitre, on va déterminer expérimentalement les diagrammes de phase $(T-H)$ des domaines de Condon pour un échantillon d'argent puis pour un échantillon de béryllium par les mesures de susceptibilité AC (cf. chapitre 4). On va montrer que la détection de la réponse non linéaire est suffisamment sensible pour des expériences en champ magnétique intense d'une bobine résistive. Les diagrammes de phase expérimentaux de l'argent et du béryllium sont ensuite comparés aux prédictions théoriques.

In this chapter the nonlinear response due to the discovered hysteresis in the Condon domain state (CDS) is used to detect the phase boundary between the homogeneous and the domain state. Experimental phase diagrams for silver and beryllium will be presented.

5.1 Introduction

We have seen in chapter 1 that the equation

$$\chi_B = \mu_0 \frac{\partial M}{\partial B} > 1 \tag{5.1}$$

defines a boundary between the uniform and the CDS. If the Fermi surface parameters like the curvature A'' and the effective mass m^* are known for a given metal and the Dingle temperature T_D has been determined for a given sample, the CDS phase diagram in the (H,T) plane can be predicted using the Lifshitz-Kosevich (LK) formula [9]. Theoretical phase diagrams based on the LK-formula were presented in sections 1.6.2 for silver and section 1.7.2 for beryllium.

Up to now Condon domains have been observed by different experimental methods: by NMR [4], μSR spectroscopy [5, 6] and as described in chapter 3 they where directly observed by Hall probes [96]. All experimental observations have in common that two distinct inductions B_1 and B_2 corresponding to an induction splitting $\delta B = B_2 - B_1$ are measured at a given applied field H_a and temperature T. However, all measurements yield only a few values of (H, T) where Condon domains exist which might be in agreement or not with theoretical calculations of the phase diagram. For example, the data on beryllium obtained by μSR required new phase diagram calculations with a modified LK-formula for the susceptibility [8]. The determination of the CDS phase boundary, where δB approaches zero, is difficult and time-consuming with the above cited methods [29]. Moreover, the result is not precise enough. In chapter 3 the phase boundary was found, for example, with Hall probes for an applied field of 10 T (see figure 3.3a).

It was shown in the previous chapter that small hysteresis occurs in the dHvA effect under the conditions of the CDS [97]. Due to the irreversible magnetization, an extremely nonlinear response to a very small modulation field arises in standard ac susceptibility measurements. The out of phase part and the third harmonic of the pickup voltage rise steeply at the transition point to the CDS. Moreover, it was shown that the point (H, T) where the hysteresis arises, which corresponds to the transition point to the CDS, does not depend on the sample shape. The threshold character of these quantities offers therefore a possibility to measure a Condon domain phase diagram with much higher precision than with the above cited methods. One should note that the third harmonic of the susceptibility is commonly used as a very sensitive tool to detect phase boundaries also of other systems like e.g. the vortex-glass transition in superconductors [98].

5.2 Silver

In this section we determine the Condon domain phase diagram for silver using the third harmonic of the susceptibility. It was shown earlier [85] that calculations based on the LK-formula are in very good agreement with experimental dHvA data up to 10 T on silver. This is certainly due to the nearly spherical Fermi surface of silver. Because the LK-formula describes well the dHvA oscillations in silver, we would expect good agreement with a theoretical phase diagram based on the LK-formula (see figure 1.12). Therefore, we actually start the CDS phase diagram investigations with silver.

5.2.1 Experimental

The measurements were performed on a high quality silver single crystal of $4.1 \times 2.1 \times 1.0$ mm^3. The largest surface of the sample was normal to the $[100]$-axis of the crystal. The sample was cut from the same piece than the sample used for the direct observation

of Condon domains [96] in chapter 3. The sample preparation is described in section 2.6 and in more detail in [83]. The sample has a residual resistance ratio $R_{300\mathrm{K}}/R_{4.2\mathrm{K}} = 1.6\times10^4$, measured by the contactless Zernov-Sharvin method [84]. The very high quality of the sample results in a very low Dingle temperature, which was estimated from our measurements to be about $T_D = 0.2$ K.

A standard ac modulation method with a compensated pickup coil system, which is commonly used for dHvA measurements, was used. The coil system is presented in section 2.2 and is shown in figure 2.2. Both pickup coils are identical and consist of about 400 turns. A long coil wound by a copper wire produced the modulation field with various amplitudes at frequencies of $20-200$ Hz. The pickup voltage was simultaneously measured by lock-in amplifiers (SRS 830) on the first and on higher harmonics. The measurements were performed in a superconducting coil up to 16 T as well as in a resistive coil up to 28 T at temperatures of $1.3-4.2$ K. The long side of the sample was parallel to the $[100]$-axis of the single crystal. In the setup the long side of the sample was slightly tilted with respect to the direction of the applied magnetic field so that only the dHvA frequency from the "belly" orbit of 47300 T existed in the frequency spectrum.

The method, we use here, is to our knowledge applied for the first time to find a CDS phase diagram. Therefore, we have to present more precisely the technical details of the measurements. We where especially concerned about the changing measurement conditions between the superconducting and the resistive coils. The magnetic field of the latter is, for example, much more noisy and less homogeneous.

5.2.2 Hysteresis in Silver

As was mentioned above, the idea of this method to determine a Condon domain phase diagram is based on the appearance of hysteresis in the CDS which was first discovered on beryllium and has been presented in chapter 4. At the phase transition to the CDS hysteresis appears [97] and this results in some radical changes in the response to an ac modulation field. In principle, all these changes can be used to trace the phase boundary of the CDS. In the following, we will show that the same characteristic features in the ac response, like in beryllium, are found in silver.

First of all, the amplitude of the susceptibility, normalized on the modulation level, should depend on the modulation amplitude in presence of hysteresis. This is expected to occur when the modulation level is of the order of the hysteresis loop width, like it is schematically shown in figure 5.1a. As a result, after the transition to CDS, the positive (paramagnetic) part of the susceptibility turns out to be reduced. From a comparison of two normalized susceptibilities, one measured with high and the other with low modulation level, we can in principle find where the amplitude reduction starts and thereby the transition point to the CDS. One disadvantage of this method is that it requires measure-

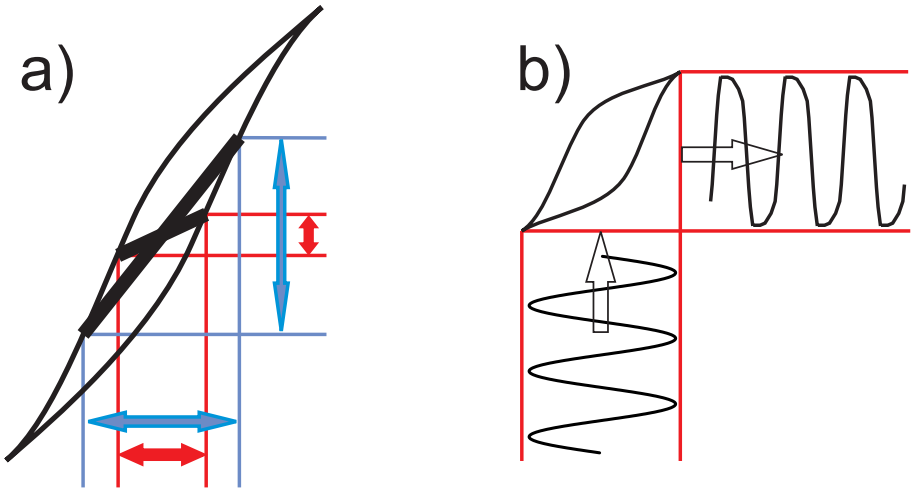

Figure 5.1: (a) The response to a field modulation is nonlinear in presence of hysteresis when the modulation amplitude is of the order of the width of the hysteresis loop. (b) The ac response becomes more window-like and is slightly shifted in phase due to the hysteresis.

ments at the lowest possible modulation level. Moreover, one needs to measure at least two or more field dependencies, which takes time.

Secondly, as soon as hysteresis arises, the ac response becomes extremely nonlinear. It is shown schematically in figure 5.1b that the response to a sinusoidal field modulation becomes window shaped and is slightly shifted in phase with respect to the input. Therefore, both the third harmonic and the out-of-phase signal of the pickup voltage increase steeply when the CDS phase boundary is crossed [97]. This threshold behavior offers a simple way to determine the transition point of the CDS. The major advantage of third harmonic measurements is that only one magnetic field or temperature sweep is needed. Moreover, we will see below that the obtained values for the phase boundary (H, T) do not depend drastically on the frequency and level of the field modulation. This will be important for measurements in the resistive coil.

Before we start the measurements for magnetic fields up to 28 T, it was necessary to investigate the above mentioned features in more detail. Furthermore, we need to compare quantitatively the results between superconducting and resistive coils. In the latter we have much more noise so that we need to increase the amplitude of the measurement signal by raising the modulation level and frequency.

Figures 5.2a and b, 5.3a and b show the above discussed features in the pickup signal at constant temperature $T = 2.7$ K measured in the superconducting coil. Figure 5.2a shows two traces of the normalized pickup voltage, i.e. the susceptibility, obtained in the same conditions with 1.0 G and 0.2 G modulation amplitude at 160 Hz modulation

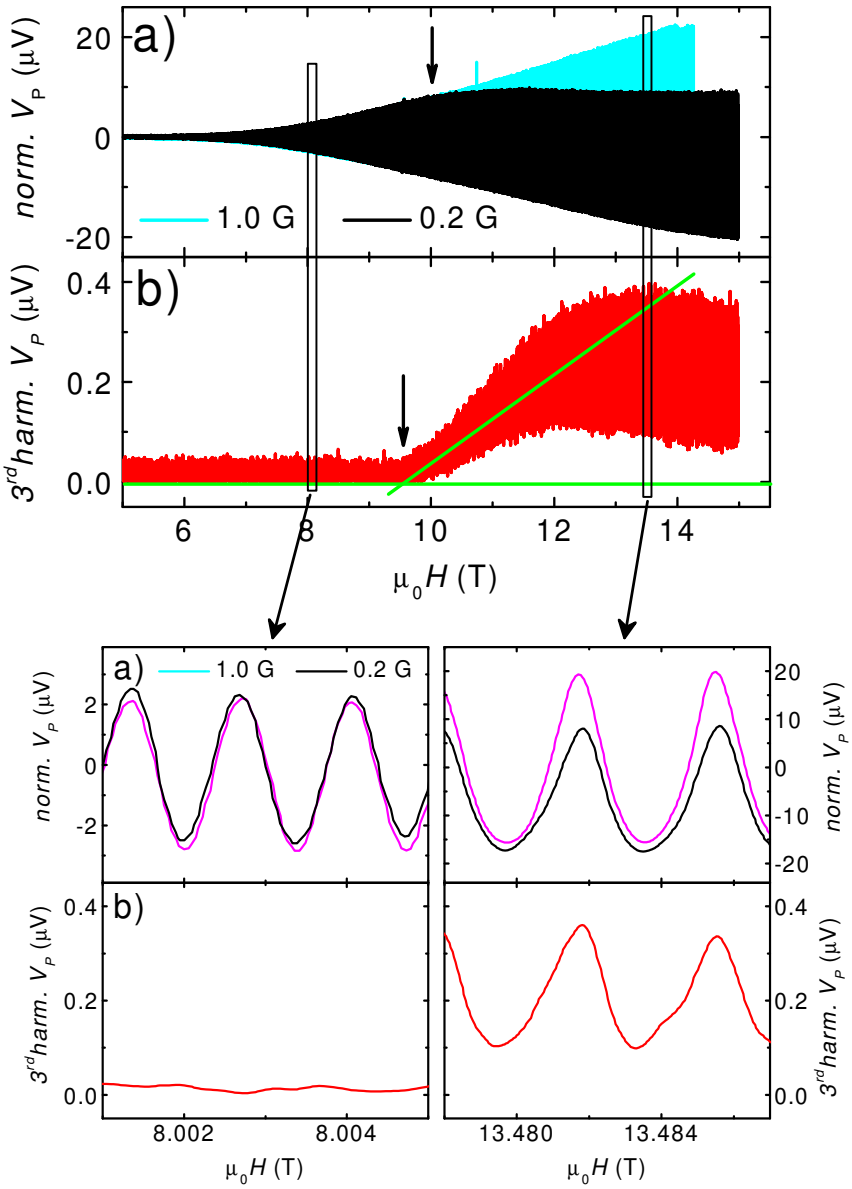

Figure 5.2: (a) Pickup voltage normalized on the modulation level for low and high modulation level. Up to about 10 T the response is linear with respect to the modulation level. (b) Third harmonic of the pickup voltage measured at 0.2 G modulation amplitude showing that starting from 9.5 T the harmonic content in the response increases steeply. Lower part of the figure shows respective zooms.

frequency. In principle, both modulation levels are small enough compared to the dHvA period of about 20 G at 10 T that identical traces are expected for the susceptibility (see section 2.2). The zoom for lower fields around 8 T, which is outside the CDS, shows that the normalized signals are indeed identical. For higher fields, on the other hand, the upper part of the susceptibility waveform, measured with the smaller modulation level, is reduced. The zoom shows in detail that the signals are identical except for the positive part of the oscillation. This implies that at this part of the dHvA oscillation the magnetization is slightly irreversible and there is a small hysteresis loop. The width of the hysteresis loop is certainly less than 1.0 G and might be of the order of 0.2 G.

A similar decreasing of the normalized response was observed earlier [14] on silver at low temperatures and in magnetic fields less than 8 T. Unfortunately, it is impossible to compare the presented data in [14] with our results.

The magnetic field where the normalized pickup voltages start to differ between low and high modulation level is marked approximately by an arrow in figure 5.2a. We obtain for the critical magnetic field $\mu_0 H_{c1} = 10.0$ T. It seems to us that this method to determine the phase boundary of the CDS is not the most convenient because the difference between the waveforms occurs only very gradually. Furthermore, the value of the critical field might decrease slightly if one could measure with even lower modulation levels. Nevertheless, the critical field of 10 T at 2.7 K corresponds roughly with the phase boundary conditions found by Hall probes in chapter 3 in figure 3.3a.

Figure 5.2b shows the behavior of the third harmonic which was simultaneously measured with the first harmonic response in figure 5.2a with 0.2 G modulation amplitude. For magnetic fields lower than the critical field there is only noise. At the transition to the CDS hysteresis arises and the third harmonic starts to increase very steeply. This is nicely seen in the respective zooms. The critical field of the CDS phase boundary can be obtained as the intersection of the two straight lines shown in figure 5.2b. Here, the critical field is found as $\mu_0 H_{c2} = 9.5$ T.

Comparing the waveform of the third harmonic measured on silver in figure 5.2b with the waveform measured on beryllium (see figure 4.4) we notice that the minima of the third harmonic oscillations are at zero voltage for beryllium whereas for silver the oscillations lift off at the transition field. We expect that the amplitude of the third harmonic goes to zero in each oscillation period because in the diamagnetic part of the dHvA oscillation the sample is homogeneous and therefore there is no hysteresis that would cause higher harmonics. The result for silver is therefore not "ideal" as the third harmonic does not go to zero in each period. This is certainly a result of small rectification or, what is the same, a result of phase smearing of the oscillation signal. Generally speaking, there are at least two reasons for this. The homogeneity of the coil is not high enough (it is about 30 ppm in a sphere with 1 cm diameter which may result in a field inhomogeneity of about 1 G in the sample volume at 10 T) which means that the transition to the CDS does not occur simultaneously in the whole sample. This is the main reason here and this effect will be

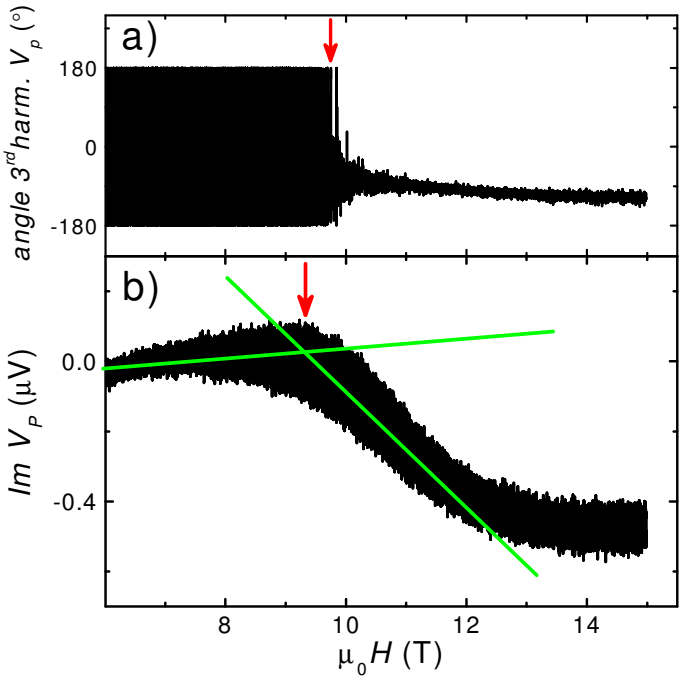

Figure 5.3: (a) Phase angle of the third harmonic showing clearly the transition between noise outside the CDS and a fixed phase in the CDS. (b) The out-of-phase part of the first harmonic response changes due to the arising hysteresis. Both data measured at 2.7 K and 0.2 G modulation level.

much bigger in a resistive coil where the homogeneity is 20 times less. Another possible reason is the finite ramp rate of the field sweeps. In the superconducting coil this effect is practically absent because the ramp rate can be arbitrarily low. But in the resistive coil the latter reason might occur, too. Nevertheless, as we will see below, both reasons for the third harmonic rectification do not affect the determination of the critical field of the CDS.

In figure 5.3a the phase angle of the third harmonic is shown for the same conditions like in figure 5.2. For magnetic fields where the amplitude of the third harmonic is below the noise level its phase angle is not determined. Therefore, the phase varies from $-180°$ to $+180°$. With the appearance of a third harmonic signal at the transition to the CDS the phase becomes finite. This passage has a threshold character as well. The arrow in figure 5.3a shows the position of the threshold which yields the critical field $\mu_0 H_{c3} = 9.8$ T.

The behavior of the out-of-phase part of the first harmonic response, shown in figure 5.3b, offers the last possibility to determine the critical field. In the uniform state, without domains, the imaginary part is small and varies smoothly especially at low mag-

netic field due to the magnetoresistance and changing eddy currents. After the transition to the CDS the out-of-phase signal changes rapidly. The transition point can be again found as the intersection of two lines, as it is shown in figure 5.3b. Here, we obtain for the critical field $\mu_0 H_{c4} = 9.3$ T.

A comparison of the values $H_{c1\ldots c4}$ for the transition field at 2.7 K shows that they are very close. In addition the critical field of about 10 T correspond roughly with the phase boundary found by Hall probes in chapter 3 in figure 3.3a. This means that all above presented methods could be, in principle, used to determine the phase boundary of the CDS at least when a superconducting coil with high field homogeneity and low noise is used. Nevertheless, we think that the easiest and most precise way to determine the critical field is by measurements of the third harmonic response. Therefore, this method will be used below to determine the CDS phase diagram for silver.

As mentioned above there is much more noise in the resistive magnet compared to the superconducting magnet. Therefore, for experiments in the resistive magnet we needed to increase the signal by using rather high modulation frequencies ≈160 Hz and higher modulation amplitudes, 1.0 G and more. In the following we check whether the modulation frequency and amplitude can be varied without changing the value of the critical field deduced from the third harmonic response. A modulation frequency change modifies slightly the behavior of the imaginary part, which is due to the eddy currents. But the position of the deduced critical field is not affected. The same result is found when the modulation amplitude is increased.

We have seen that modulation amplitudes of the order of the width of the hysteresis loop are required to resolve the amplitude reduction in the normalized pickup voltage in figure 5.2a. For the third harmonic, however, the features persist up to high modulation amplitudes. Figure 5.4 shows traces with 0.2 and 1.0 G modulation amplitude while over the oscillations visible in figure 5.2b was averaged. For 1.0 G modulation amplitude there is a small third harmonic signal before the transition to the CDS takes place. This small contribution to the third harmonic is due to the nonlinearity of the dHvA effect itself (see section 2.2 and [11]). Nevertheless, the position of the sharp increase remains unchanged. Moreover, the noise level exceeds this small signal in a resistive magnet (see also figure 5.5).

Figure 5.5 shows that increasing the modulation amplitude up to 10 G and varying the modulation frequency by a factor four between 40 Hz and 160 Hz does not change the position of the critical field, either. The results presented here were obtained in the resistive magnet. The measurements were made at low temperatures in order to compare them with data obtained in the superconducting magnet. After all, the values found for the critical fields coincide with the results of the superconducting coil. Figure 5.6 shows an example of the transition point measurement in the resistive coil at the top of the phase diagram at 4.2 K.

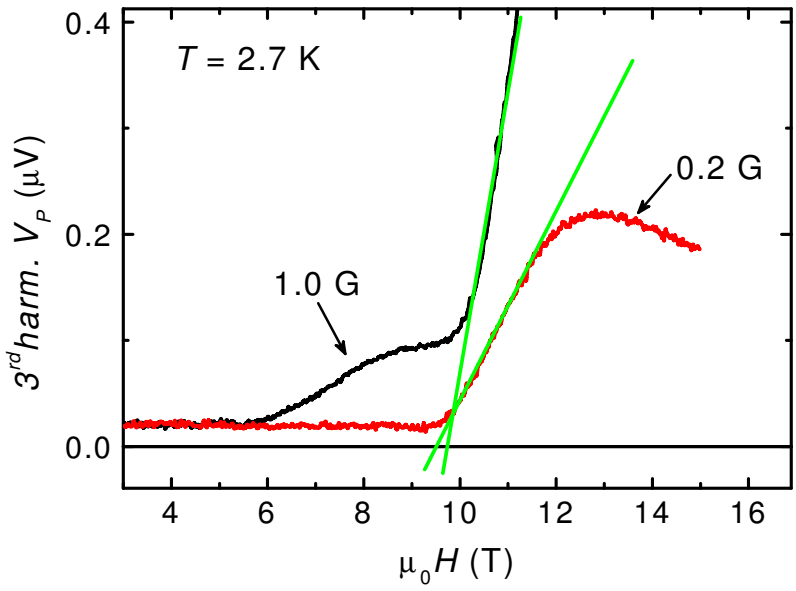

Figure 5.4: Amplitude dependence of the third harmonic response measured in a superconducting coil. The same critical field is found from the steep increase.

5.2.3 Phase diagram

All results obtained in the superconducting and the resistive magnets are presented in figure 5.7. The critical fields for each temperature are found as the field where the third harmonic response starts to arise like in figure 5.6. The solid line in figure 5.7 is the CDS boundary calculated for silver using the LK-formula with a Dingle temperature of $T_D = 0.2$ K as parameter for our sample. We see good agreement of the predictions based on the LK-formula with our data. Moreover, data points obtained in superconducting and resistive magnets overlap which supports again that the different measurement conditions did not affect the precise determination of the phase boundary.

At the flat top of the CDS phase diagram between 20 and 30 T it would be, in principle, better to make temperature sweeps with a variable temperature insert (VTI) at a fixed magnetic field while measuring the third harmonic response. Field sweeps are in this field range tangent to the phase boundary and therefore it might be difficult to determine the value of the critical field.

5.2.4 Conclusion

We have shown that hysteresis appears in silver in the Condon domain state. This substantiates the conclusion of chapter 4 that hysteresis is likely to occur in all pure metals

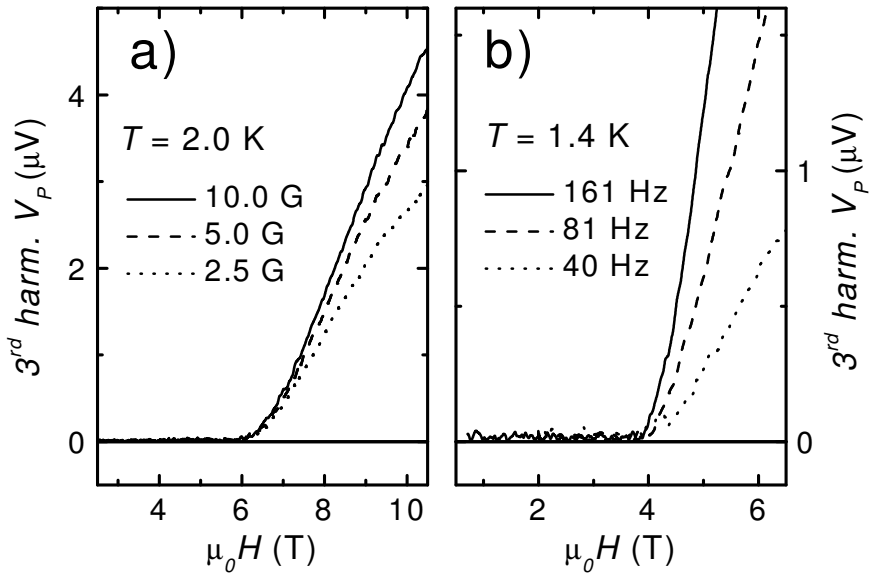

Figure 5.5: (a) Amplitude and (b) frequency dependence of the third harmonic response measured in a resistive coil. The critical field values obtained at a given temperature are independent on modulation frequency and amplitude.

that exhibit Condon domains. Due to the hysteresis similar features like in beryllium, especially the sharp increase of the third harmonic response at the transition from the uniform to the Condon domain state, are found in the pickup voltage. This offered the possibility to determine easily the CDS phase boundary with high accuracy. The critical fields obtained from both, the third harmonic and the out-of-phase part of the pickup voltage, turned out to be independent on changes of the modulation frequency and amplitude. The CDS phase boundary could be traced in a wide magnetic field range up to 28 T using resistive and superconducting magnets. Eddy currents affect slightly the behavior of the out-of-phase part in silver when the frequency is increased. Therefore, we preferred to use the third harmonic response to measure the phase boundary. The situation might be different in a less conducting metal.

We have found very good agreement with the LK-theory. Of course, it would be very interesting to continue the measurements to higher magnetic fields to see if the agreement holds for the whole phase diagram. This method for the determination of the CDS phase boundary could possibly be used in pulse fields as well, if the modulation frequency could be increased correspondingly.

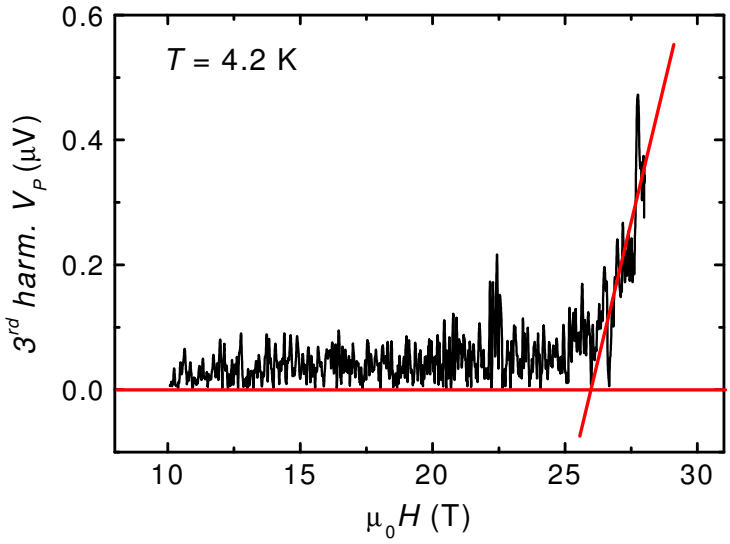

Figure 5.6: Example of a third harmonic response measurement at 4.2 K in a resistive magnet up to 28 T.

5.3 Beryllium

In this section we establish an experimental Condon domain phase diagram for beryllium in the same way as it was done in the previous section for silver. It was shown in section 1.7.2 that theoretical calculations for the CDS show big discrepancies with the conditions where Condon domains were actually observed. To overcome these shortcomings a new phase diagram for beryllium was calculated in [8] with a modified LK-formula. It is in good agreement with results obtained with μSR [6, 8]. Nevertheless, there is only very few data from μSR experiments that is able to test the recent calculations. In order to collect data for the whole Condon domain phase diagram of beryllium, we make the nonlinear response measurements which were suggested in chapter 4 and in [97].

5.3.1 Experiment

The standard pickup coil system which is shown in figure 2.2 was used for the measurements. The results shown here were measured on the same rod-like sample, that was used in chapter 4, of sizes $8 \times 2 \times 1$ mm^3 with the long side being parallel to $[0001]$. The magnetic field was applied parallel to the long side of the sample. We found from our measurements a Dingle temperature of $T_D = 2.0$ K. The experiments were carried out in a 10 T superconducting coil in a standard ^{4}helium cryostat which could be pumped down

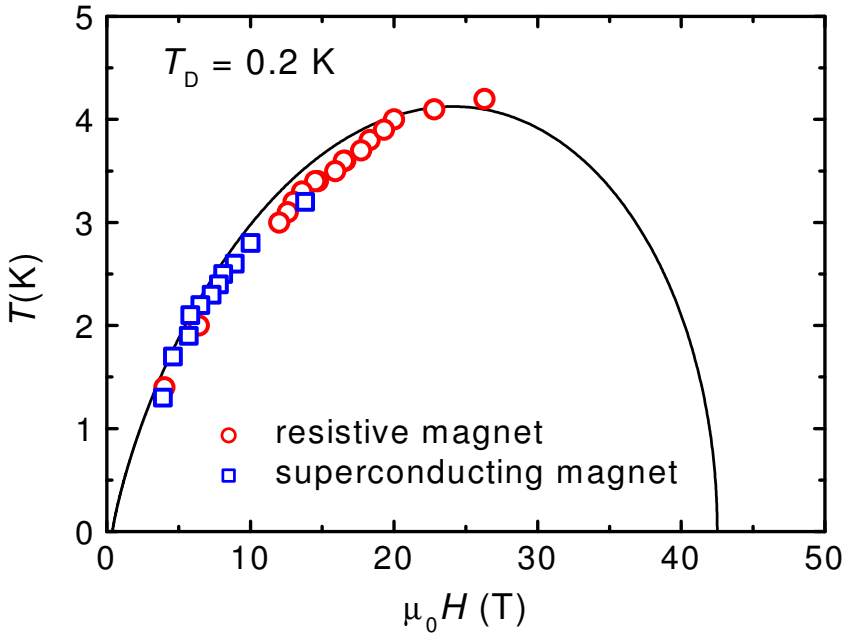

Figure 5.7: Phase diagram in the $H - T$ plane for silver. Experimental points from the superconducting and resistive magnet. The solid line is the CDS boundary calculated by the LK-formula for $T_D = 0.2$ K.

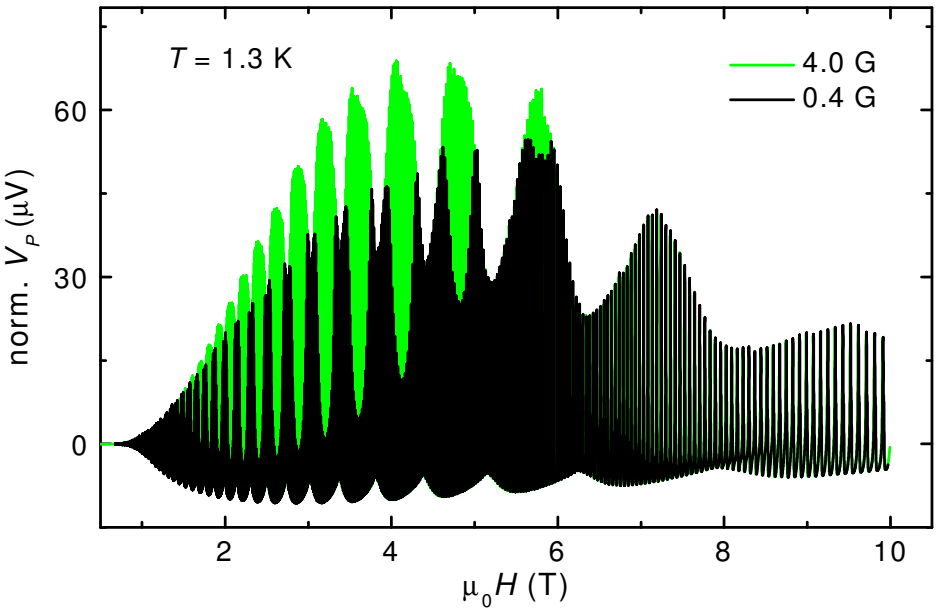

Figure 5.8: Pickup voltage normalized on the modulation level for high and low modulation level at 1.3 K. Due to hysteresis in the CDS the pickup voltage is nonlinear at the paramagnetic part of the dHvA oscillations.

to 1.3 K. Some further experiments were made in a 16 T coil with a variable temperature insert (VTI) which offered the possibility to measure temperature dependencies at a fixed applied magnetic field. In contrast to chapter 4 where low modulation frequencies of the order of 20 Hz and less were used, here we increased the frequency to about 160 Hz after having checked that the principle features do not change (see for example figure 5.5). The frequency increase allowed us to reduce the integration time of the lock-in amplifier and to use again smaller modulation amplitudes.

5.3.2 Results

As was pointed out in the previous section on the phase diagram for silver, several methods can be used to determine the Condon domain phase diagram. Figure 5.8 shows the pickup voltage normalized on the modulation level for low and high modulation amplitude in a large magnetic field range at 1.3 K. Due to the hysteresis in the CDS [97] the amplitude of the pickup voltage at the paramagnetic part of the dHvA oscillation decreases when the modulation level is of the order or smaller than the width of the hysteresis loop (see also figure 4.2a). One can, in principle, determine for which magnetic fields hystere-

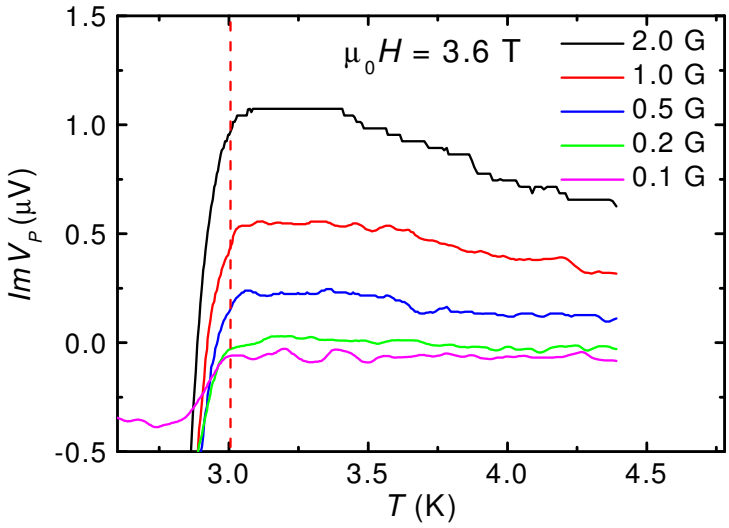

Figure 5.9: Temperature dependence of the imaginary part of the pickup voltage for several modulation amplitudes at the beat antinode at 3.6 T. The dashed line indicates the critical temperature $T_c = 3.0$ K where the Condon domain phase boundary is crossed.

sis and consequently Condon domains occur at a given temperature by subtracting both dHvA waveforms in figure 5.8 from each other. We see, for example, that there is no difference between the normalized pickup voltages for magnetic fields exceeding 7 T. This implies that Condon domains disappear for fields higher than 7 T at 1.3 K. The disadvantage of this method to determine the Condon domain phase diagram is that two field dependencies must be measured for each temperature. Furthermore, in order to detect the presence of even very small hysteresis the modulation level should be as small as possible.

We have seen in chapter 4 that the out-of-phase part and the third harmonic of the pickup voltage appear with threshold character whenever there is a small hysteresis in the dHvA magnetization. A measurement of one of these quantities offers therefore a simpler way to determine the phase boundary of the CDS. Figure 5.9 shows temperature dependencies of the out-of-phase part of the pickup voltage in a large modulation level range at the antinode of the dHvA oscillation envelope at 3.6 T. At the critical temperature $T_c = 3.0$ K the out-of-phase signal drops down rapidly. This indicates a sudden phase shift of the ac response with respect to the modulation signal, which is caused by the emerging hysteresis in the dHvA magnetization (see figure 5.1b). We find the same T_c, indicated by the dashed line in figure 5.9, for all modulation levels. The determination of the CDS phase boundary is thus independent on the modulation level. In the following we will use a modulation amplitude of 0.4 G. This value is sufficiently small to insure

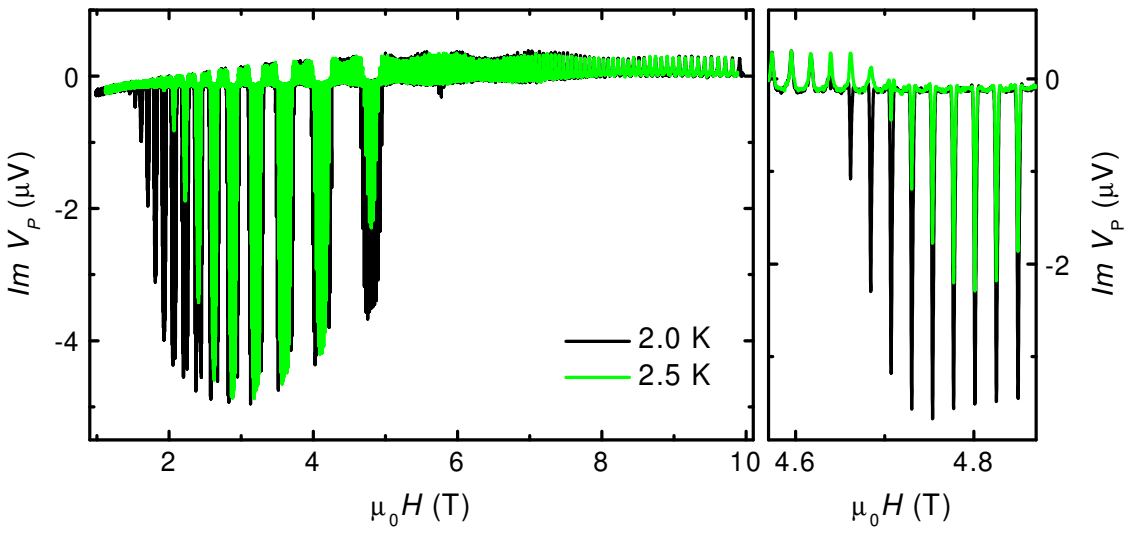

Figure 5.10: Field dependence of the imaginary part of the pickup voltage measured at 2.0 K and 2.5 K with 0.4 G modulation amplitude. The huge negative amplitude is caused by the hysteresis in the CDS. The right graph shows a zoom around 4.8 T.

that the dHvA period ΔH is always much bigger than the modulation amplitude h even at very low magnetic fields[1] and on the other hand the ac response is still easily detectable.

Figure 5.10 shows magnetic field dependencies of the imaginary part of the pickup voltage measured at 2.0 K and 2.5 K. The phase of the lock-in amplifier is adjusted in a way that the signal, that is due to the susceptibility of the sample, is mainly in-phase. dHvA oscillations with small amplitude, similar to the waveform in figure 5.8, are however visible around zero voltage. We note that the amplitude of the dHvA oscillations in the out-of-phase signal was much smaller in figure 4.4b. There a modulation frequency of only 21 Hz was used. The enhancement of the frequency to 160 Hz leads to increasing eddy currents, which affect mainly the out-of-phase signal. Huge negative peaks appear at magnetic fields where hysteresis occurs, like it was discovered in chapter 4 in figure 4.4b. This means that the sample is in the CDS for the magnetic fields around each peak (see zoom of figure 5.10). Figure 5.10 shows that the field range for which peaks appear is much more extended at 2.0 K than at 2.5 K, especially at lower magnetic fields around 2 T. At temperatures above 3.0 K all peaks disappear and only the small dHvA oscillations remain. The amplitude of the peaks depends on the modulation level, on the width of the hysteresis loop at the particular magnetic field and on the amplitude of the in-phase part of the pickup voltage, i.e. the susceptibility. Even though the peak amplitude seems to be correlated with the Condon domain phase diagram, we extract only for each temperature

[1] If the modulation amplitude is of the order of the dHvA period the imaginary part and the third harmonic increase even though there is no hysteresis (see section 2.2 and [11])

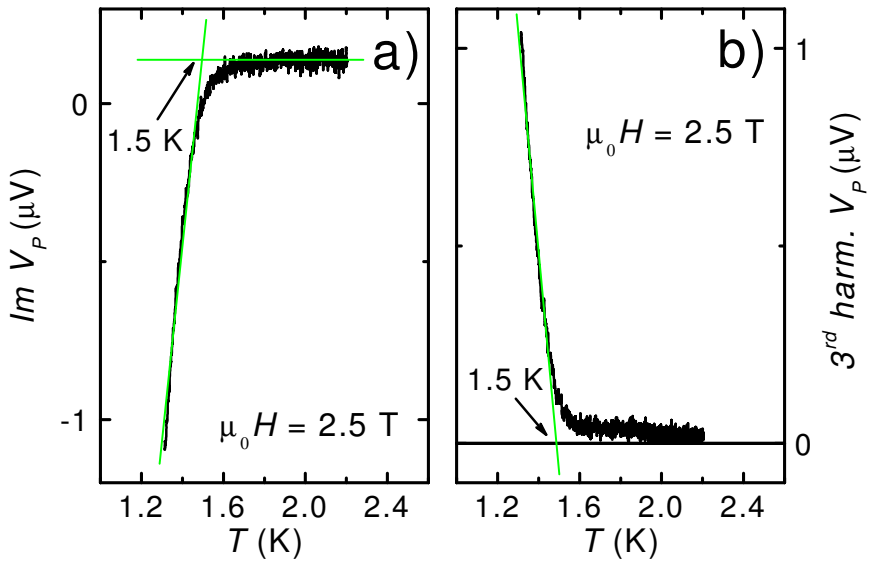

Figure 5.11: Temperature dependence of the (a) imaginary part and the (b) third harmonic of the pickup voltage measured at the beat node at 2.5 T with 0.4 G modulation amplitude.

the magnetic fields for which peaks appeared in order to construct the phase diagram in the next section.

It was reported in [5, 8, 29] that Condon domains occur also at the nodes of the dHvA oscillation envelope around 2.0 T and 2.7 T at 0.5 K and 0.8 K, respectively. As explained above, there are only very few temperature dependencies of the induction splitting measured with μSR. In other words, the reported temperatures do not necessarily represent the phase boundary of the CDS. Therefore, we tried to reach the phase boundary at beat nodes in the pumped ^{4}helium cryostat. A base temperature of 1.3 K can be reached in this cryostat (see chapter 2). Figure 5.11 shows the temperature dependence of the out-of-phase part (a) and the third harmonic (b) of the pickup voltage at the beat node at 2.5 T. A sharp transition at 1.5 K is visible in both traces which indicates that hysteresis arises at this temperature. This means that Condon domains are indeed formed at this beat node for temperatures lower than 1.5 K.

5.3.3 Phase diagram

We have seen that the CDS phase boundary can be determined with high precision by measuring the critical magnetic field where hysteresis starts to arise in the dHvA magnetization. Due to the hysteresis the out-of-phase signal of the pickup voltage drops rapidly.

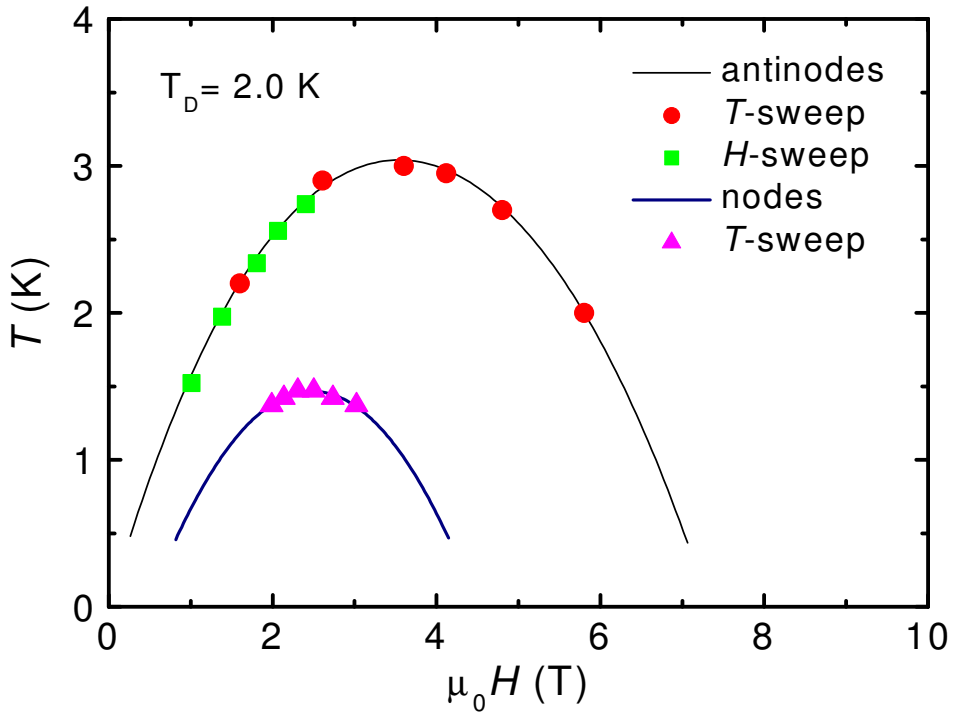

Figure 5.12: Phase diagram in the $H - T$ plane for beryllium. Scatter points indicate the position of the phase boundary determined by temperature sweeps like in figure 5.9 and 5.11 and field sweeps like in figure 5.10. The parabolas are fits to the phase boundary at the dHvA beat nodes and antinodes, respectively.

This was measured either at a fixed applied field like in figure 5.9 and 5.11 or at a fixed temperature as function of magnetic field like in figure 5.10. All this data is compiled to obtain a complete phase diagram. Figure 5.12 shows the Condon domain phase diagram for beryllium. The parabolas[2] are fits to the (H, T) values obtained at the beat antinodes and nodes, respectively.

Figure 5.13a shows narrow needles which correspond to the magnetic fields where sharp peaks appeared in figure 5.10. For magnetic fields between the needles the sample is in the homogeneous state. We see in figure 5.13a that Condon domains appear first for magnetic fields near a beat antinode. When cooling down the field range extends gradually around the antinode. Furthermore, we tested on a plate-like sample with the same Dingle temperature that the obtained phase diagram is independent on the shape of the sample. In other words the Condon domain phase diagram does not depend on the demagnetization factor. The difference between both samples was that the needles in figure 5.13a were much broader for the plate-like sample. The reason for this is that the field range within a dHvA period where domains arise is more extended in a plate-like sample (see chapter 1). The critical temperature at a given magnetic field, i.e. the top of each needle, remains, however, the same for rod-like and plate-like samples.

Moreover, the phase diagram in figure 5.12 agrees with all data from μSR [5, 8, 13, 29]. There is especially a temperature dependence of the induction splitting at the beat antinode near 2.6 T. It was found by μSR that the induction splitting disappears for temperatures higher than 3.0 K. We examined the same beat maximum and found a critical temperature of 2.9 K in our sample.

In figure 5.13b the experimental phase diagram from figure 5.12 is compared with the calculations made with the modified LK-formula in [6, 8]. There is only agreement for magnetic fields around 2.6 T. Starting from 4 T the calculation predicts still increasing critical temperatures whereas our measurements show clearly a rapid decrease. We see in addition that Condon domains continue to exist down to low fields at pretty high temperatures.

5.3.4 Conclusion

We have measured a complete Condon domain phase diagram for beryllium at temperatures down to 1.3 K and magnetic fields from 1 T up to 10 T. The method based on the detection of the nonlinear response to an ac field modulation provided also information about the substructure of the phase diagram which is due to the dHvA frequency beat in beryllium. The measurements agree with data from μSR where a sample with the same Dingle temperature was used.

[2]The phase boundary of the CDS, predicted by the LK-formula, is not parabolic in the (H, T)-plane (see chapter 1). The fits are guides to the eye in analogy to figure 1.15.

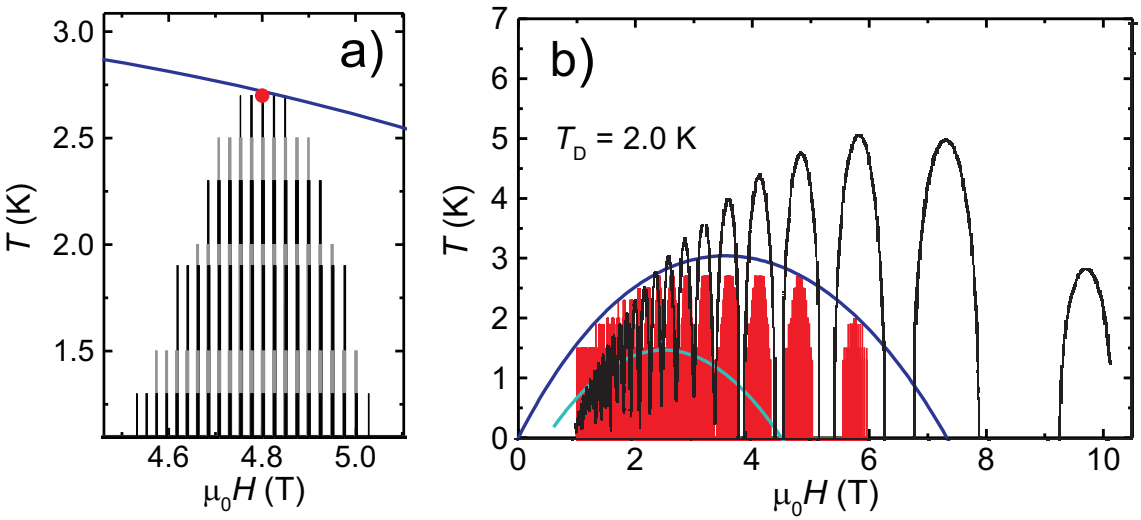

Figure 5.13: (a) Zoom of figure 5.12 around the beat maximum at 4.8 T showing the substructure of the phase diagram. (b) Comparison of the experimental phase diagram with theoretical calculations (solid black line) from [6, 8] based on the modified LK-formula.

Moreover, we have tested that the obtained phase diagram does not depend on the shape of the sample. The method can be easily applied to samples with different Dingle temperatures.

The comparison of the experimental phase diagram with theoretical calculations [8] shows differences especially for magnetic fields exceeding 4 T. Finally, we find from our measurements an upper critical field of about 8 T above which no domains exist for all temperatures in a sample with $T_D = 2.0$ K.

Summary

This thesis reports investigations on magnetic domains called "Condon domains". These domains are one of the rare examples of a magnetic domain structure with non-spin origin. The main topics addressed in this work are the visualization of the Condon domain structure with micro Hall probes and the question whether the dHvA magnetization exhibits hysteresis in the domain state. Furthermore, experimental phase diagrams of the Condon domain state are measured for silver and beryllium.

Direct evidence for Condon domains has been obtained as yet only in a few cases. After their discovery by Condon and Walstedt [4] in silver using NMR, they were more recently observed by Solt *et al.* in beryllium, white tin, lead and aluminium with μSR [5, 6]. However, there are some important open questions concerning the size, geometry and topology of Condon domains which could not be addressed with these spectroscopic methods. Therefore, the aim of this thesis is to measure directly the induction distribution at the sample surface with a local magnetic field probe.

Several generations of micro-Hall probes are developed to meet the challenging requirements of spatial and magnetic resolution at low temperatures and high offset magnetic fields. In particular a field contrast of $\Delta B/B \approx 10^{-4}$ on length scales of typically tens of micrometers should be resolved. Particular attention is drawn to the sample preparation as single crystals of very high quality are needed to observe Condon domains. Especially the silver samples are of outstanding quality and have a very low Dingle temperature.

Condon domains are for the first time revealed with a local magnetic probe. Using a Hall probe setup consisting of two arrays of each five Hall probes an induction splitting of up to 10 G is observed on silver at fields and temperatures which are in agreement with the theoretically estimated phase diagram. A laminar domain structure is found whose orientation is mainly transverse to the long sample axis. The domain motion is always reversible for increasing and decreasing magnet field. From the known sizes of the Hall probe array an estimation of the domain pattern size is deduced. The domain period is not smaller than 150 μm and the domain wall thickness must be about 20 μm for the 1 mm thick silver sample at 10 T and 1.3 K.

The same experiments are made on a beryllium sample on which Condon domains

were successfully observed using μSR and even bigger induction differences were expected than for the silver sample. However, an induction splitting of only 2 G is observed at the surface which implies that Condon domains do not emerge to the surface in beryllium.

The second major topic of this thesis is the investigation whether the dHvA magnetization shows hysteresis in the Condon domain state. The domain state consists of two phases of different induction values with a magnetization current in the domain walls. It was shown that the transition from the homogeneous state to the domain state is of first order [7]. At this phase transition all phenomena like irreversibility, supercooling and hysteresis are in principle expected. However, hysteresis in the dHvA effect has up to now only been discussed in several papers [9, 14].

In this work hysteresis is for the first time resolved in the dHvA magnetization under the conditions of the Condon domain state. A hysteresis loop with a width of a few Gauss is directly observed with Hall probes on a beryllium sample. As a complimentary method standard modulation field measurements reveal that the ac response to a modulation field is highly nonlinear as function of the modulation level. Furthermore, it is shown that the out-of-phase part and the third harmonic of the pickup voltage rise steeply when the magnetization becomes irreversible. The threshold character with which the nonlinearities arise offers a simple and robust possibility to measure Condon domain phase diagrams.

Finally, the nonlinearities arising in the ac response are used to determine Condon domain phase diagrams for silver and beryllium. In particular, it is shown that the same features that were previously found in the ac response on beryllium exist also in silver, another system that exhibits Condon domain formation. The Condon domain phase diagram for a silver sample is traced in a wide magnetic field range up to 28 T using resistive and superconducting magnets. Excellent agreement with the LK-theory is found in the explored field and temperature range.

For beryllium a very complete Condon domain phase diagram is presented for temperatures down to 1.3 K and magnetic fields from 1 T up to 10 T. The ac response technique provides also information about the substructure of the phase diagram which is due to the dHvA frequency beat in beryllium. The phase diagram agrees with data from μSR for a sample with the same Dingle temperature. A comparison of the experimental phase diagram with theoretical calculations [8] reveals differences especially for magnetic fields exceeding 4 T. An upper critical field of about 8 T is found above which no domains appear for all temperatures in a beryllium sample with $T_D = 2.0$ K.

Outlook

Despite of the progress made in this field in recent years there are still some open problems. Let us summarize first the perspectives of the experiments presented in this work.

The Condon domain visualization experiments with Hall probes presented in chapter 3 can be studied in more detail. First, the influence of the sample thickness and the demagnetization factor on the size of the domain structure can be studied. Furthermore, it is planned to make similar measurements on high quality single crystals made of copper. On the other hand more information on the domain structure could certainly be gained using a scanning Hall probe. Here, the first attempts to move the Hall probe with respect to the sample surface are under way.

The ac response measurements could be applied to construct Condon domain phase diagrams for other metals that exhibit Condon domain formation like e.g. lead and aluminium. Here, certainly lower temperatures than that available in a pumped ^{4}helium cryostat are needed as μSR experiments evidenced Condon domains only at temperatures below 300 mK in these metals. Moreover, it would be interesting to investigate the evolution of the phase diagram for samples with different Dingle temperatures. In particular, the phase diagram for silver, which has been established for magnetic fields up to 28 T in this work, could be continued to higher fields to check if the good agreement with the Lifshitz-Kosevich theory holds for the whole phase diagram.

Besides the perspectives concerning directly the experiments presented in this thesis we should mention the following open questions.

Fingerprints of the phase transition between the homogeneous and the Condon domain state should, in principle, occur in other thermodynamic quantities like specific heat. An anomaly of the specific heat at the phase transition has been predicted in [99] and up to now only unsuccessful attempts were made to find this anomaly [81]. However, specific heat measurements would be particularly useful to elucidate whether the phase transition from the homogenous to the Condon domain state is of first or second order.

Recent measurements of magnetostriction oscillations and compressibility in beryllium have shown an increase of the compressibility as a result of Condon domain formation [87, 88]. Considering the anisotropic magnetostriction of beryllium will certainly help to understand why Condon domains do not emerge to the sample surface in beryllium contrary to silver.

Besides normal metals, the transition to the Condon domain state in layered metals and especially in organic quasi-2D compounds is of particular interest, since the cylindrical Fermi surface with a unique cyclotron frequency should lead to a giant effect.

Finally, Condon domains are the only type of magnetic domains for which the dynamics of domain walls have not been considered, in contrast to the continuous progress in investigation of other magnetic ordered systems.

Conclusion en français

L'existence des domaines de Condon, prédite théoriquement en 1966 par Condon [3], a été démontrée jusqu'à présent dans un certain nombre de métaux, à l'aide de la résonance magnétique nucléaire dans un échantillon d'argent par Condon et Walstedt [4] et à l'aide de la rotation de spin de muon (μSR) dans le béryllium, l'étain, le plomb et l'aluminium par Solt *et al.* [5, 6]. Ces méthodes spectroscopiques ne permettent cependant pas de déterminer la taille, la géométrie et la topologie de ces domaines. Le sujet de cette thèse est de visualiser directement la distribution de l'aimantation à la surface d'un échantillon à l'aide d'une sonde magnétique locale. Notons que l'origine de ces domaines n'est pas l'interaction entre les spins des électrons mais "l'interaction magnétique" dans l'effet de Haas-van Alphen.

Pour la visualisation des domaines de Condon, plusieurs générations de microsondes de Hall sont développées afin de remplir les spécifications difficiles de la résolution spatiale et de la résolution magnétique à basse température et à champ magnétique intense. Notamment, une différence d'induction de $\Delta B/B \approx 10^{-4}$ doit être résolue sur des distances de quelques dizaines de micromètres. De plus, la qualité des monocristaux est essentielle pour observer les domaines de Condon; en particulier, nous avons eu l'opportunité de mesurer un échantillon d'argent ayant une température de Dingle très basse ($T_D = 0.2$ K), mesure de la qualité cristalline de l'échantillon. Pour la première fois, la structure des domaines de Condon a été détectée directement à la surface d'un échantillon en argent. L'induction (ou l'aimantation locale) est mesurée à l'aide d'un réseau de cinq microsondes de Hall. Les sondes mesurent périodiquement une différence locale d'aimantation dans la partie paramagnétique des oscillations dHvA, différence attribuée aux domaines de Condon. La direction de propagation des parois des domaines et leur orientation en sont déduites. Ces mêmes expériences ont été réalisées sur un échantillon de béryllium, sur lequel des domaines de Condon ont été mesurés par μSR. Pourtant, nous n'avons pas pu visualiser les domaines à la surface. Les expériences de visualisation des domaines de Condon à l'aide des sondes de Hall doivent être étendues, il est notamment intéressant de déterminer l'influence de l'épaisseur de l'échantillon et du facteur démagnétisant sur la taille de la structure des domaines. De plus, on obtiendrait beaucoup plus d'information sur les structures des domaines à l'aide d'un dispositif à balayage de sonde de Hall qu'à l'aide du réseau de cinq microsondes dont la résolution spatiale est

très limitée. Un tel microscope de Hall est en cours de développement.

La réversibilité de l'aimantation d'un échantillon en présence de domaines de Condon est étudiée. Les calculs théoriques ont montré que la transition entre l'état homogène et l'état avec domaines est de premier ordre [7]. En principe, l'hystérèse de l'aimantation accompagne une telle transition de phase. L'hystérèse est montrée à l'aide des sondes de Hall en variant lentement le champ magnétique appliqué puis confirmée par des mesures de susceptibilité AC. A très faible amplitude de modulation, la susceptibilité n'est plus linéaire en fonction de l'amplitude, en outre, la troisième harmonique de la susceptibilité montre des valeurs exceptionnellement grandes. Ce comportement très sensible est utilisé pour déterminer expérimentalement les diagrammes de phase (T, H) des domaines de Condon dans un échantillon d'argent puis dans un échantillon de béryllium. Le diagramme de phase de l'échantillon d'argent, mesuré jusqu'à 28 T doit être étendu à des champs magnétiques plus intenses. Cette méthode pourrait être appliquée à d'autre métaux dans lesquels l'existence des domaines de Condon a été vérifiée par μSR (le plomb, l'étain et l'aluminium). Par ailleurs, le diagramme de phase d'un métal, par ex. l'argent, pourrait être mesuré en fonction de la température de Dingle.

Récemment, Gordon *et al.* [99] ont prédit une anomalie de la chaleur spécifique à la transition de phase entre l'état homogène et l'état avec domaines de Condon. Cette anomalie n'a pas été observée expérimentalement jusqu'à présent. Avec la connaissance précise du diagramme de phase de l'échantillon, ces expériences devraient être plus simples à réaliser.

Bibliography

[1] I. M. Lifshitz and A. M. Kosevich, "Theory of magnetic susceptibility in metals at low temperatures," Soviet Physics JETP **2**, 636 (1956), [Zhurnal Eksperimental'noi i Teoreticheskoi Fiziki 29, 730 (1955)]. 7, 9, 16, 19

[2] D. Shoenberg, "The Fermi Surfaces of Copper, Silver and Gold I. The de Haas-van Alphen Effect," Royal Society of London Philosophical Transactions Series A **255**, 85–133 (1962). 7, 19

[3] J. H. Condon, "Nonlinear de Haas-van Alphen Effect and Magnetic Domains in Beryllium," Physical Review **145**, 526–35 (1966). 7, 9, 10, 24, 28, 45, 71, 88, 123

[4] J. H. Condon and R. E. Walstedt, "Direct evidence for magnetic domains in silver," Physical Review Letters **21**, 612–14 (1968). 7, 8, 9, 28, 29, 33, 54, 61, 71, 72, 75, 83, 84, 88, 100, 119, 123

[5] G. Solt, C. Baines, V. S. Egorov, D. Herlach, E. Krasnoperov, and U. Zimmermann, "Observation of diamagnetic domains in beryllium by muon spin rotation spectroscopy," Physical Review Letters **76**, 2575–8 (1996). 7, 9, 27, 28, 60, 66, 72, 83, 88, 100, 114, 116, 119, 123

[6] G. Solt and V. S. Egorov, "Recent results on Condon domains in metals," Physica B **318**, 231–50 (2002). 7, 8, 10, 31, 37, 72, 100, 109, 116, 117, 119, 123

[7] Y. M. Blanter, M. I. Kaganov, and D. V. Posvyanskii, "de Haas-van Alphen effect as a first-order electronic topological transition," Physics Uspekhi **38**, 203–9 (1995), [Uspekhi Fizicheskii Nauk 165, 213 (1995)]. 8, 10, 88, 120, 124

[8] G. Solt, "Phase diagram for Condon domains in beryllium," Solid State Communications **118**, 231–4 (2001). 8, 10, 37, 100, 109, 114, 116, 117, 120

[9] A. Gordon, I. D. Vagner, and P. Wyder, "Magnetic domains in non-ferromagnetic metals: the non-linear de Haas-van Alphen effect," Advances in Physics **52**, 385–454 (2003). 8, 10, 72, 88, 99, 120

[10] A. Hubert and R. Schäfer, *Magnetic Domains - The Analysis of Magnetic Microstructures* (Springer, Berlin, 1998). 9, 87

[11] D. Shoenberg, *Magnetic oscillations in metals* (Cambridge University Press, Cambridge, 1984). 9, 13, 17, 20, 31, 42, 44, 45, 46, 66, 68, 80, 83, 87, 90, 106, 113

[12] A. Gordon, M. A. Itskovsky, I. D. Vagner, and P. Wyder, "Order parameter for a diamagnetic phase transition," Physical Review Letters **81**, 2787–90 (1998). 9, 32, 36, 72

[13] G. Solt, V. S. Egorov, C. Baines, D. Herlach, and U. Zimmermann, "Condon domains in aluminum and lead," Physica B **326**, 536–9 (2003). 10, 31, 72, 116

[14] J. L. Smith and J. C. Lashley, "Domain state occurring in the de Haas-van Alphen effect in silver," Journal of Low Temperature Physics **135**, 161–4 (2004). 10, 88, 104, 120

[15] N. W. Ashcroft and N. D. Mermin, *Solid State Physics* (Saunders College Publishing, Fort Worth, 1976). 13

[16] C. Kittel, *Introduction to Solid State Physics* (Wiley, New York, 1996), 7th edn. 13, 46

[17] M. Springford ed. *Electrons at the Fermi surface* (Cambridge University Press, Cambridge, 1980). 13

[18] L. Onsager, "Interpretation of the de Haas-van Alphen effect," Philosophical Magazine **43**, 1006–8 (1952). 15

[19] R. B. Dingle, "Some magnetic properties of metals. II. The influence of collisions on the magnetic behavior of large systems," Royal Society of London Proceedings Series A **211**, 517–25 (1952). 18, 66

[20] A. B. Pippard, "Commentary on a Conjecture of Shoenberg's Concerning the de Haas-van Alphen Effect," Royal Society of London Proceedings Series A **272**, 192–206 (1963). 19

[21] L. D. Landau, E. M. Lifshitz, and L. P. Pitaevskii, *Electrodynamics of Continuous Media*, Vol. 8 (Butterworth-Heinemann, Oxford, 1984), 2nd edn. 26

[22] C. Kittel, "Physical Theory of Ferromagnetic Domains," Reviews of Modern Physics **21(4)**, 541–83 (1949). 26, 27

[23] J. H. Condon, "Magnetic domains in materials exhibiting strong dHvA effect," in *Proceedings of the 10th International Conference on Low Temperature Physics* **3**, 289 (1966). 27

[24] A. Schenck, *Muon Spin Rotation Spectroscopy* (Hilger, Bristol, 1986). 28

[25] V. S. Egorov, "Condon domains - these non-magnetic diamagnetic domains," HAIT Journal of Science and Engineering **1**, 647–72 (2004). 30

[26] Y. M. Belousov and V. P. Smilga, "Possibility of investigation of diamagnetic domains by the positive muon method," Soviet Physics Solid State **21**, 1416–17 (1979), [Fizika Tverdogo Tela 21, 2459 (1979)]. 28

[27] V. S. Egorov, E. P. Krasnoperov, F. V. Lykov, U. Zimmermann, G. Solt, C. Baines, and D. Herlach, "Observation of diamagnetic domains in beryllium," Physics of the Solid State **40**, 482–4; Original: Fizika–Tverdogo–Tela. March 1998; 40(3): 524–6 (1998). 30

[28] G. Solt, C. Baines, V. S. Egorov, D. Herlach, E. P. Krasnoperov, and U. Zimmermann, "Direct evidence for dia- and paramagnetic domains in beryllium," Hyperfine Interactions **104**, 257–63 (1997). 30, 66, 72, 83

[29] G. Solt, C. Baines, V. S. Egorov, D. Herlach, and U. Zimmermann, "Diamagnetic domains in beryllium observed by muon-spin-rotation spectroscopy," Physical Review B Condensed Matter **59**, 6834–45 (1999). 30, 35, 36, 60, 66, 71, 72, 75, 83, 88, 100, 114, 116

[30] G. Solt, C. Baines, V. S. Egorov, D. Herlach, and U. Zimmermann, "Observation of dia- and paramagnetic domains in beryllium and white tin by muon spin rotation spectroscopy," Journal of Applied Physics **87**, 7144–6 (2000). 31, 72

[31] G. Solt, V. S. Egorov, C. Baines, D. Herlach, and U. Zimmermann, "Evidence for Condon domains in white tin with two de Haas-van Alphen periods," Physical Review B Condensed Matter **62**, R11 933–6 (2000). 31, 72

[32] A. S. Joseph and A. C. Thorsen, "Low-Field de Haas-van Alphen Effect in Ag," Physical Review **138**, 1159–64 (1965). 31

[33] T. S. Choy, J. Naset, J. Chen, S. Hershfield, and C. Stanton, "A database of fermi surface in virtual reality modeling language (vrml)," Bulletin of The American Physical Society **45**, 36–42 (2000).
http://www.phys.ufl.edu/fermisurface 31

[34] A. Gordon, M. A. Itskovsky, and P. Wyder, "Quantizing field-induced magnetic phase in a three-dimensional electron gas," Physical Review B Condensed Matter **59**, 10 864–8 (1999). 33, 75, 76

[35] W. M. Bibby, P. T. Coleridge, N. S. Cooper, C. M. M. Nex, and D. Shoenberg, "Curvature factors for the noble metals," Journal of Low Temperature Physics **34**, 681–94 (1979). 33

[36] W. A. Reed and J. H. Condon, "Effect of magnetic breakdown and nonlinear magnetization on the high- field magnetoresistance of Be," Physical Review B Solid State **1**, 3504–10 (1970). 34

[37] T. L. Louks and P. H. Cutler, "Band Structure and Fermi Surface of Beryllium," Physical Review **133**, 819–29 (1964). 34

[38] J. H. Tripp, P. M. Everett, W. L. Gordon, and R. W. Stark, "Fermi surface of beryllium and its pressure dependence," Physical Review **180**, 669–77 (1969). 34

[39] L. R. Testardi and J. H. Condon, "Landau quantum oscillations of the velocity of sound in Be: the strain dependence of the Fermi surface," Physical Review B Solid State **1**, 3928–42 (1970). 34, 35

[40] N. E. Alekseevskii and V. I. Nizhankovskii, "Oscillations of the chemical potential and the equation of state for beryllium," Soviet Physics JETP **61**, 1051–5 (1985), [Zhurnal Eksperimental'noi i Teoreticheskoi Fiziki 88, 1771 (1985)]. 34

[41] V. S. Egorov, "Anomalous amplitude of the de Haas-van Alphen effect in a quasi two-dimensional electron gas in beryllium," Soviet Physics Solid State **30**, 730–2 (1988), [Fizika Tverdogo Tela 30, 1253 (1988)]. 36

[42] H. Preston-Thomas, "The International Temperature Scale of 1990 (ITS-90)," Metrologia **27**, 3–10 (1990).
http://www.its-90.com 40

[43] "Magnets of the GHMFL and their performances," .
http://ghmfl.grenoble.cnrs.fr/ 42

[44] D. Shoenberg and P. J. Stiles, "The de Haas-Van Alphen Effect in Alkali Metals," Royal Society of London Proceedings Series A **281**, 62–91 (1964). 42

[45] A. Goldstein, S. J. Williamson, and S. Foner, "Low Frequency Field Modulation Differential Magnetometer; Applications to the De Haas-Van Alphen Effect," Review of Scientific Instruments **36**, 1356–65 (1965). 42

[46] R. W. Stark and L. R. Windmiller, "Theory and technology for measuring the de Haas-van Alphen type spectra in metal," Cryogenics **8**, 272–81 (1968). 42

[47] B. Knecht, G. G. Lonzarich, J. M. Perz, and D. Shoenberg, "Eddy currents in magnetic measurements," Journal of Low Temperature Physics **29**, 499–531 (1977). 44, 45, 88, 94

[48] R. Griessen, "A capacitance torquemeter for de Haas-van Alphen measurements," Cryogenics **13**, 375–7 (1973). 46, 67

[49] S. J. Bending, "Local magnetic probes of superconductors," Advances in Physics **48**, 449–535 (1999). 48, 49, 62, 72

[50] F. M. Peeters and X. Q. Li, "Hall magnetometer in the ballistic regime," Applied Physics Letters **72**, 572–4 (1998). 49

[51] S. J. Bending and A. Oral, "Hall effect in a highly inhomogeneous magnetic field distribution," Journal of Applied Physics **81**, 3721–5 (1997). 49

[52] A. Thiaville, L. Belliard, D. Majer, E. Zeldov, and J. Miltat, "Measurement of the stray field emanating from magnetic force microscope tips by Hall effect microsensors," Journal of Applied Physics **82**, 3182–91 (1997). 49

[53] H. Guillou, A. D. Kent, G. W. Stupian, and M. S. Leung, "Geometries for high spatial resolution Hall probes," Journal of Applied Physics **93**, 2746–51 (2003). 49

[54] S. Liu, H. Guillou, A. D. Kent, G. W. Stupian, and M. S. Leung, "Effect of probe geometry on the Hall response in an inhomogeneous magnetic field: A numerical study," Journal of Applied Physics **83**, 6161–5 (1998). 49

[55] Y. G. Cornelissens and F. M. Peeters, "Response function of a Hall magnetosensor in the diffusive regime," Journal of Applied Physics **92**, 2006–12 (2002). 49, 50

[56] J. E. Simpkins, "Microminiature Hall Probes for Use in Liquid Helium," Review of Scientific Instruments **39**, 570–5 (1968). 50

[57] R. N. Goren and M. Tinkham, "Patterns of magnetic flux penetration in superconducting films," Journal of Low Temperature Physics **5**, 465–494 (1971). 50, 62

[58] R. Dingle, H. L. Stormer, A. C. Gossard, and W. Wiegmann, "Electron mobilities in modulation-doped semiconductor heterojunction superlattices," Applied Physics Letters **33**, 665–7 (1978). 50

[59] S. J. Bending, K. von Klitzing, and K. Ploog, "Two-dimensional electron gas as a flux detector for a type-II superconducting film," Physical Review B Condensed Matter **42**, 9859–64 (1990). 50

[60] S. T. Stoddart, S. J. Bending, A. K. Geim, and M. Henini, "Quantum-resolved investigations of flux dynamics: collective and single vortex effects," Physical Review Letters **71**, 3854–7 (1993). 50

[61] E. Zeldov, A. I. Larkin, V. B. Geshkenbein, M. Konczykowski, D. Majer, B. Khaykovich, V. M. Vinokur, and H. Shtrikman, "Geometrical barriers in high-temperature superconductors," Physical Review Letters **73**, 1428–31 (1994). 50

[62] E. Zeldov, D. Majer, M. Konczykowski, V. B. Geshkenbein, V. M. Vinokur, and H. Shtrikman, "Thermodynamic observation of first-order vortex-lattice melting transition in $Bi_2Sr_2CaCu_2O_8$," Nature **375**, 373–6 (1995). 50

[63] E. Pugel, E. Shung, T. F. Rosenbaum, and S. P. Watkins, "Local magnetometry at high fields and low temperatures using InAs Hall sensors," Applied Physics Letters **71**, 2205–7 (1997). 51

[64] S. S. Murzin, I. Claus, A. G. M. Jansen, N. T. Moshegov, A. I. Toropov, and K. Eberl, "Quantum Hall effect induced by electron-electron interaction in disordered GaAs layers with a three-dimensional spectrum," Physical Review B Condensed Matter **59**, 7330–3 (1999). 52, 53

[65] M. Weiss, *Quantum Hall effect in a strongly disordered system*, Ph.D. thesis, Universität Konstanz (2004). 52

[66] L. Lehmann, *Magnetization measurements for study of Condon domains in noble metals*, Master's thesis, Universität Konstanz (2000). 52, 54, 62

[67] D. Shoenberg, *Superconductivity* (Cambridge University Press, Cambridge, 1952). 58

[68] J. D. Livingstone and W. DeSorbo, *Superconductivity* (Dekker, New York, 1969), chap. The Intermediate State in Type I Superconductors, pp. 1235–81. 58, 59, 72, 78, 79

[69] M. Tinkham, *Introduction to Superconductivity* (McGraw, New York, 1996). 58

[70] E. M. Lifshitz and Y. V. Sharvin, Doklady Akademii Nauk SSSR **79**, 783 (1951). 58

[71] A. L. Schawlow, "Structure of the Intermediate State in Superconductors," Physical Review **101**, 573–9 (1956). 59

[72] V. S. Egorov, G. Solt, C. Baines, D. Herlach, and U. Zimmermann, "Superconducting intermediate state of white tin studied by muon-spin-rotation spectroscopy," Physical Review B Condensed Matter and Materials Physics **64**, 024 524 (2001). 59

[73] J. A. Osborn, "Demagnetizing Factors of the General Ellipsoid," Physical Review **67**, 351–7 (1945). 59

[74] I. S. Grigoriev and E. Z. Meilikhov eds. *Handbook of Physical Quantities* (CRC Press, Boca Raton, 1997). 59

[75] D. R. Lide ed. *Handbook of Chemistry and Physics* (CRC Press, Boca Raton, 1998). 59

[76] Y. Kuk and P. J. Silverman, "Scanning tunneling microscope instrumentation," Review of Scientific Instruments **60**, 165–80 (1989). 61

[77] G. Binnig, H. Rohrer, C. Gerber, and E. Weibel, "Tunneling through a controllable vacuum gap," Applied Physics Letters **40**, 178–80 (1982). 61

[78] J. Heil, A. Böhm, M. Primke, and P. Wyder, "Versatile three-dimensional cryogenic micropositioning device," Review of Scientific Instruments **67**, 307–11 (1996). 62, 63, 64

[79] J. Siegel, J. Witt, N. Venturi, and S. Field, "Compact large-range cryogenic scanner," Review of Scientific Instruments **66**, 2520–3 (1995). 62

[80] D. A. Brawner and N. P. Ong, "Scanning Hall microprobe measurements of magnetization profiles in $YBa_2Cu_3O_{7-y}$ single crystals," Journal of Applied Physics **73**, 3890–902 (1993). 62

[81] J. Hinderer, *Magnetic domains with non-spin origin; Condon domains*, Ph.D. thesis, Universität Konstanz (2002). 67, 121

[82] V. A. Gasparov, "Anisotropy of the probability for electron-phonon scattering in silver," Soviet Physics JETP **41**, 1129–34 (1975), [Zhurnal Eksperimental'noi i Teoreticheskoi Fiziki 68, 2259 (1975)]. 67, 69, 74

[83] V. A. Gasparov and R. Huguenin, "Electron-phonon, electron-electron and electron-surface scattering in metals from ballistic effects," Advances in Physics **42**, 393–521 (1993). 67, 74, 101

[84] V. B. Zernov and Y. V. Sharvin, "Measurement of the resistivity of high-purity tin at helium temperatures," Soviet Physics JETP **9**, 737 (1959), [Zhurnal Eksperimental'noi i Teoreticheskoi Fiziki 36, 1038 (1959)]. 68, 74, 101

[85] R. B. G. Kramer, V. S. Egorov, A. Gordon, N. Logoboy, W. Joss, and V. A. Gasparov, ""Magnetic" phase transition in silver," Physica B **362**, 50–5 (2005). 75, 76, 100

[86] Y. V. Sharvin, "Measurement of the surface tension at the boundary between a superconducting and a normal phase," Soviet Physics JETP **6**, 1031 (1958), [Zhurnal Eksperimental'noi i Teoreticheskoi Fiziki 33, 1341 (1958)]. 79

[87] V. S. Egorov, P. V. Lykov, and O. A. Repina, "Anomalous compressibility and magnetostriction of beryllium under the conditions of diamagnetic domain formation," JETP Letters **72**, 18–20 (2000), [Pis'ma v Zhurnal Eksperimental'noi i Teoreticheskoi Fiziki 72, 28 (2000)]. 84, 121

[88] V. S. Egorov and P. V. Lykov, "Diamagnetic domains and magnetostriction in beryllium," Soviet Physics JETP **94**, 162–71 (2002), [Zhurnal Eksperimental'noi i Teoreticheskoi Fiziki 121, 191 (2002)]. 84, 88, 97, 121

[89] E. du Trémolet de Lacheisserie, D. Gignoux, and M. Schlenker eds. *Magnetism* (Kluwer Academic Publishers, Norwell, 2002). 87, 92

[90] L. Landau, "Diamagnetism in metals," Zeitschrift für Physik **64**, 629–37 (1930). 87

[91] V. I. Bozhko and E. P. Vol'skii, "Helicon damping in a metal with diamagnetic domains," JETP Letters **26**, 223–6 (1977), [Pis'ma v Zhurnal Eksperimental'noi i Teoreticheskoi Fiziki 26, 337 (1977)]. 88, 97

[92] R. D. Plummer and W. L. Gordon, "New de Haas-van Alphen Frequencies in Beryllium Caused by Magnetic Interaction," Physical Review Letters **13**, 432–4 (1964). 88, 94, 95

[93] C. Rüdt, P. J. Jensen, A. Scherz, J. Lindner, P. Poulopoulos, and K. Baberschke, "Higher harmonics of the ac susceptibility: Analysis of hysteresis effects in ultrathin ferromagnets," Physical Review B Condensed Matter **69**, 014 419 (2004). 92

[94] R. D. Plummer and W. L. Gordon, "Apparent waveform distortions in field modulation studies of the de Haas-van Alphen effect in beryllium," Physics Letters **20**, 612–4 (1966). 94

[95] A. Gordon, N. Logoboy, and W. Joss, "Size-dependent effects on the magnetization dynamics of Condon domains," Physical Review B Condensed Matter **69**, 174 417 (2004). 97

[96] R. B. G. Kramer, V. S. Egorov, V. A. Gasparov, A. G. M. Jansen, and W. Joss, "Direct Observation of Condon Domains in Silver by Hall Probes," Physical Review Letters **95**, 267 209 (2005). 100, 101

[97] R. B. G. Kramer, V. S. Egorov, A. G. M. Jansen, and W. Joss, "Hysteresis in the de Haas-van Alphen effect," Physical Review Letters **95**, 187 204 (2005). 100, 101, 102, 109, 111

[98] T. Klein, A. Conde-Gallardo, J. Marcus, C. Escribe-Filippini, P. Samuely, P. Szabo, and A. G. M. Jansen, "Vortex-glass transition in the (K,Ba)BiO/sub 3/ cubic superconductor," Physical Review B Condensed Matter **58**, 12 411–15 (1998). 100

[99] A. Gordon, M. A. Itskovsky, and P. Wyder, "Phase transitions in metals at quantizing magnetic fields," Physical Review B Condensed Matter **55**, 812–15 (1997). 121, 124

Appendix A

Publications

Parts of the present dissertation are published in the following publications:

R. B. G. Kramer, V. S. Egorov, A. G. M. Jansen, and W. Joss,
”Hysteresis in the de Haas–van Alphen Effect,”
Physical Review Letters **95**, 187204 (2005).

R. B. G. Kramer, V. S. Egorov, V. A. Gasparov, A. G. M. Jansen, and W. Joss,
”Direct Observation of Condon Domains in Silver by Hall Probes,”
Physical Review Letters **95**, 267209 (2005).

R. B. G. Kramer, V. S. Egorov, A. Gordon, N. Logoboy,
W. Joss, and V. A. Gasparov,
””Magnetic" phase transition in silver,”
Physica B **362**, 50-5 (2005).

R. B. G. Kramer, V. S. Egorov, V. A. Gasparov, A. G. M. Jansen, and W. Joss,
”Condon Domain Phase Diagram for Silver,”
submitted for publication in Physical Review B.